Doctoral Dissertation

博士論文

Effects of inter-ligand interactions on the redox and optical properties of thiolate-protected gold superatoms

(チオラート保護金超原子の酸化還元挙動と光学特性に対する配位子間相互作用の効果)

A Dissertation Submitted for the Degree of Doctor of Philosophy

December 2020

令和2年12月博士 (理学) 申請

Department of Chemistry, Graduate School of Science,

The University of Tokyo

東京大学大学院理学系研究科化学専攻

Tsubasa Omoda

重田　翼

Abstract

Gold clusters composed of several to hundreds of gold atoms can be viewed as superatoms because they take atom-like electron configuration by accommodating valence electrons in quantized orbitals labeled as 1S, 1P, 1D, 2S,…. In order to utilize the Au superatoms as novel materials and building units of functional devices, their surface must be passivated with organic ligands. Recent examples have illustrated that the ligands do not just protect the Au superatoms, but also directly affect their structures, reactivity, and physicochemical properties. In this thesis, I studied how the structures of the tail group of ligands affect the structures and properties of Au superatoms. To this end, I chose different types of bulky thiolate (RS) ligands and introduced them into a ubiquitous thiolate-protected Au cluster $[Au_{25}(SR)_{18}]^z$ which has an icosahedral (Ih) Au_{13} core fully protected by six units of $Au_2(SR)_3$ with a closed electron configuration of $(1S)^2(1P)^6$ for $z = -1$. The effect of ligand side chains on the optical and redox properties are discussed.

In Chapter 1, I describe the general introduction of simple and coinage metal clusters in a naked form and the concept of superatom. I also introduce ligand-protected metal superatoms with a focus on Au. Current understanding of the ligand effects on the structures and properties of Au superatoms is then explained.

In Chapter 2, I synthesize $[Au_{25}(SR)_{18}]^-$ with using *N*-2-(mercaptopropionyl)glycine (PGSH) as a ligand. The results of optical absorption spectroscopy and extended X-ray absorption fine structure (EXAFS) indicate that

$[Au_{25}(SPG)_{18}]^-$ is an isomer of $[Au_{25}(SR)_{18}]^-$ having an anisotropic Au core. Its optical gap of the highest occupied molecular orbital (HOMO) and the lowest unoccupied molecular orbital (LUMO) is larger than that of the conventional $[Au_{25}(SR)_{18}]^-$. Non-covalent interactions between PGS ligands probably contribute to the formation of an anisotropic core in $[Au_{25}(SPG)_{18}]^-$.

In Chapter 3, I synthesize $[Au_{25}(SR)_{18}]^0$ using cyclohexanethiol (cHexSH) as a ligand. While the conventional $[Au_{25}(SR)_{18}]^0$ with an electron configuration of $(1S)^2(1P)^5$ is easily reduced to form a closed shell of $(1S)^2(1P)^6$, $[Au_{25}(ScHex)_{18}]^0$ had resistance to the reduction. The result implies that the bulky ligand layer of cHexS prefers the structure of neutral state with an open electron configuration.

In Chapter 4, I synthesize the Fréchet-type dendritic thiol (DenSH) with benzyloxy groups and introduce them into $[Au_{25}(SEtPh)_{18}]^-$ (PhEtSH = 2-phenylethanethiol). Partially exchanged $[Au_{25}(SEtPh)_{18-x}(SDen)_x]^-$ shows stronger photoluminescence (PL) than unexchanged one. The result is ascribed to the suppression of non-radiative decay processes by the rigidification of Au core via CH–π and/or π–π interactions between DenS ligands. In addition, I introduce DenSH into $[Au_{23}(ScHex)_{16}]^-$ with an anisotropic Au_{13} core to study how PL enhancement changes dependent on Au core. The effects of the number and generation of DenSH is also discussed.

In Chapter 5, I give a summary of the thesis and describe future prospects as a concluding remark.

Contents

Chapter 1.

General introduction

1.1. Metal nanoparticles and clusters

Metal nanoparticles (NPs) with the diameter of few to hundreds nm have gained much attention in a wide range of scientific disciplines because they show different physicochemical properties from the corresponding bulk. They have a large surface-to-volume ratio and a high fraction of coordinatively unsaturated sites such as edges and corners.[1] Therefore, transition metal NPs show an outstanding catalytic activity toward small molecules and have been applied in various reactions such as drug synthesis and gas reforming.[2-5] Coinage metal NPs show strong extinction in ultraviolet-visible (UV-vis) region due to the localized surface plasmon resonance (LSPR).[6] The LSPR of Ag and Au NPs is widely utilized for photocatalysis, bioimaging, and photothermal therapy.[6-9] These properties of metal NPs can be described as functions of the diameter and shape using the physical constants of bulk metal. For example, the diameter D of a cuboctahedral NP with a face-centered cubic (FCC) packing and the shell number m is described as

$$D = 2\sqrt[3]{\frac{5\sqrt{2}}{4\pi}}md \approx 1.65md \tag{1.1}$$

where d represents the diameter of the constituent atoms.[10] Then, we can calculate the number of surface atoms N_s of a metal NP with m as follows:[11]

$$N_s = 10m^2 - 20m + 12 \tag{1.2}$$

The LSPR extinction coefficient C_{ext} of a spherical metal NP is dependent on its radius R:[6]

$$C_{ext} = \frac{24\pi^2 R^3 \varepsilon_m^{3/2} N}{\lambda \ln(10)} \frac{\varepsilon_i}{(\varepsilon_r + 2\varepsilon_m)^2 + \varepsilon_i^2} \tag{1.3}$$

where ε_m, N, and λ are the dielectric constant of the surrounding medium, the electron density, and the wavelength of the incident light, respectively. $\varepsilon = \varepsilon_r + i\varepsilon_i$ represents the

complex dielectric constant of the bulk metal. The LSPR peak wavelength is given when $\varepsilon_r = -2\varepsilon_m$.[6] In addition, the ionization potential (IP) and electron affinity (EA) of a metal NP can be calculated as functions of R according to the liquid drop model:[12]

$$IP = W_{\mathrm{B}} + \alpha \frac{e^2}{R} \tag{1.4}$$

$$EA = W_{\mathrm{B}} + \beta \frac{e^2}{R} \tag{1.5}$$

where W_{B} and e represent the bulk work function and elementary charge, respectively, and α and β are constants. By these equations, the structures and properties of metal NPs can be scaled from corresponding bulk metals.

Metal NPs show a structural transition when the diameter is reduced to 1–2 nm. Specific geometrical structures such as an icosahedron or a decahedron emerge to minimize their high surface energy (Figure 1.1).[13] Their electronic structure also changes from continuous band structure to discrete energy states.[14] Thereby, metal NPs in this size

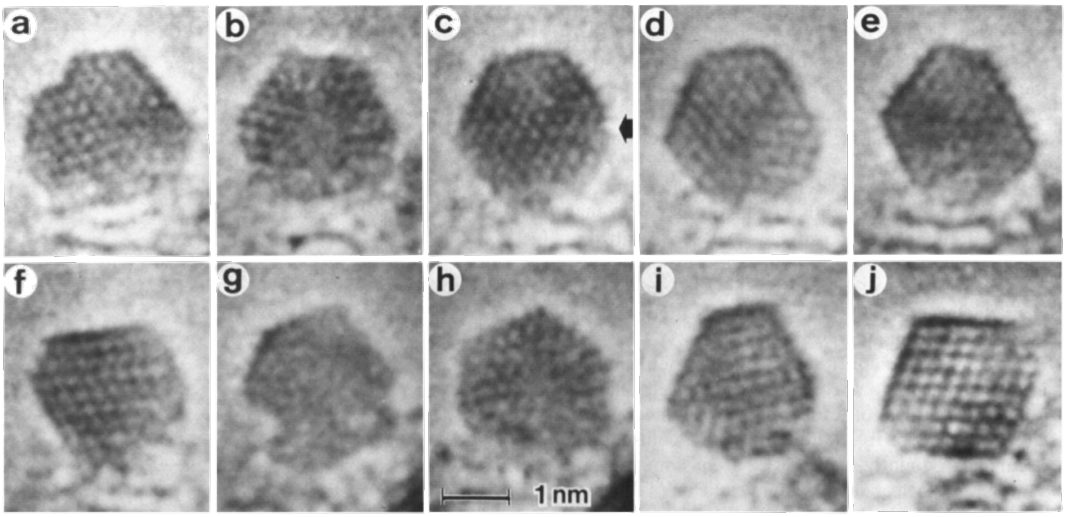

Figure 1.1. (a-j) Electron micrographs of a single Au NP with the diameter of 2 nm. The shape of the particle continuously changes under electron beam irradiation. Shape: single twin (a,d,i); multiple twin (g); cuboctahedron (c,e,f,j); icosahedron (b,h). Adapted with permission from ref. 13. Copyright 1986 American Physical Society.

region are distinctively called as “metal clusters”. The structures and properties of metal clusters drastically change depending on the number of constituent atoms, i.e., size. For example, Figure 1.2 shows the electron binding energies of Cu_n^-, Ag_n^-, and Au_n^- determined by photoelectron (PE) spectroscopy.[15] They fluctuate and do not follow the scaling law of eq 1.5 especially in the small size region. Metal clusters can be viewed as a different state from both NP and bulk.

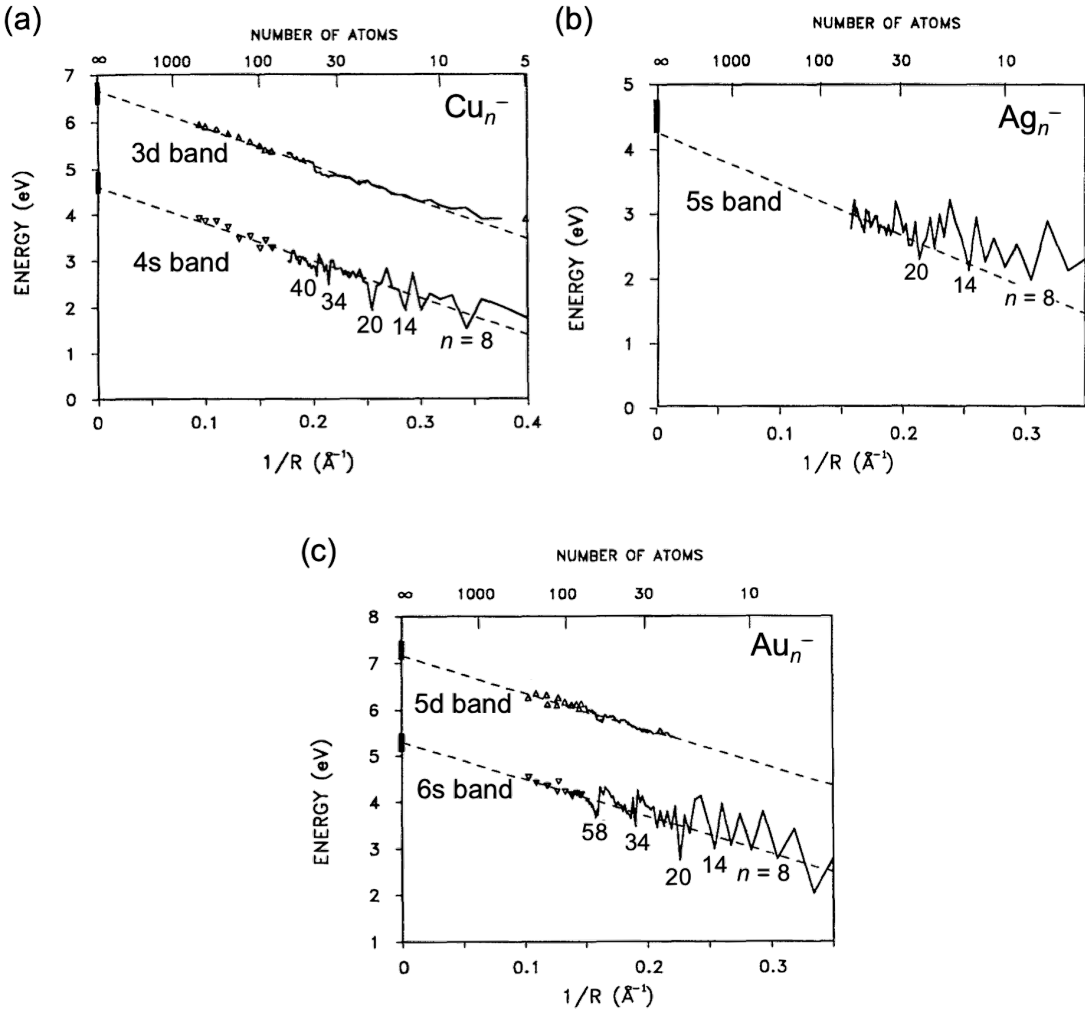

Figure 1.2. Plots of the onsets of s and d bands in PE spectra of (a) Cu_n^-, (b) Ag_n^-, and (c) Au_n^- as functions of cluster size. The dashed lines are the predicted EAs according to eq 1.5. Adapted with permission from ref. 15. Copyright 1992 American Institute of Physics.

1.2. Superatom concept

1.2.1. Isolated superatoms

Fundamental issues about the structure, stability, and reactivity of isolated metal clusters have been extensively studied in the gas phase especially for simple alkali metals.[16] Figures 1.3a shows the mass spectrum of Na_n^0 clusters.[17] The abundance of each peak is plotted in Figure 1.3b.[16] Apparently, the peaks at n = 8, 20, 40, and 58 (magic number) are more prominent than adjacent ones, suggesting that Na_8, Na_{20}, Na_{40}, and Na_{58} are much more stable than the neighbors. The same trend is observed in the mass spectrum

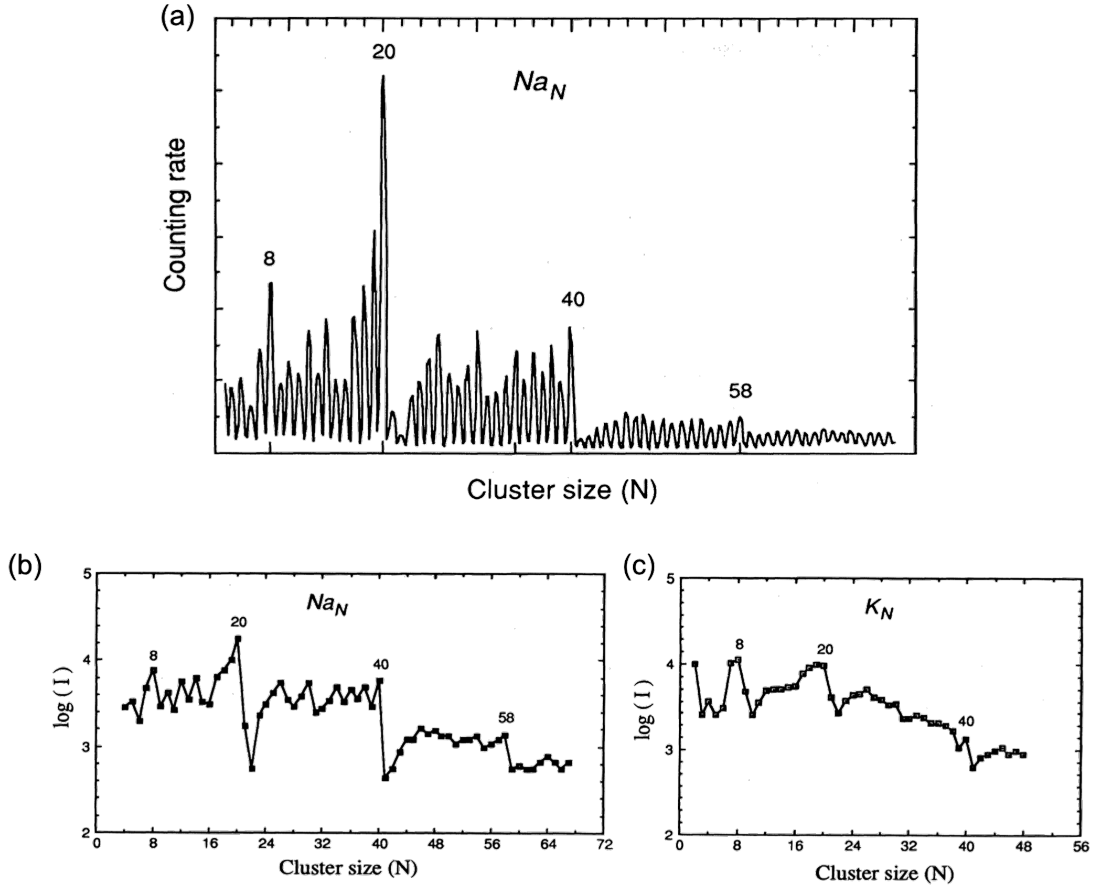

Figure 1.3. (a) Mass spectrum of Na_n^0 as a function of cluster size. Na_n^+ clusters generated by photoionization of Na_n^0 are detected.[17] (b,c) Plots of peak abundance in the mass spectra of Na_n^0 and K_n^0, respectively. The size of prominent peaks is shown in each panel. Reproduced with permission from ref. 16. Copyright 1993 American Physical Society.

of K_n^0 clusters (Figure 1.3c).[18] The high stability at magic number can be understood in the framework of spherical jellium model in which valence electrons of the constituent atoms (3s or 4s electrons of Na or K atom, respectively) are delocalized over a uniform potential with a positive charge.[16] Such picture confines the delocalized electrons into discrete orbitals shown in Figure 1.4a. The number of electrons for shell closing in an intermediate potential (Figure 1.4a, center) is 2, 8, 20, 40, 58… which agrees well with the magic number of Na_n^0 and K_n^0 in Figure 1.3, suggesting that electronic shell of Na_n^0 and K_n^0 is closed at n = 8, 20, 40, and 58 because one electron (1e) per Na or K atom from valence s orbitals is provided. Electronic shell closing is also confirmed by spectroscopic studies. The photoionization spectra of Na_n^0 and K_n^0 show that their IPs discontinuously drop at the next size of n = 8, 20, 40, 58… because the energy level upshifts just after the shell closing at these sizes (8e, 20e, 40e, 58e…).[16,19,20] The discrete orbitals in the jellium model have a similar shape to that of conventional atomic orbitals and are labeled as 1S,

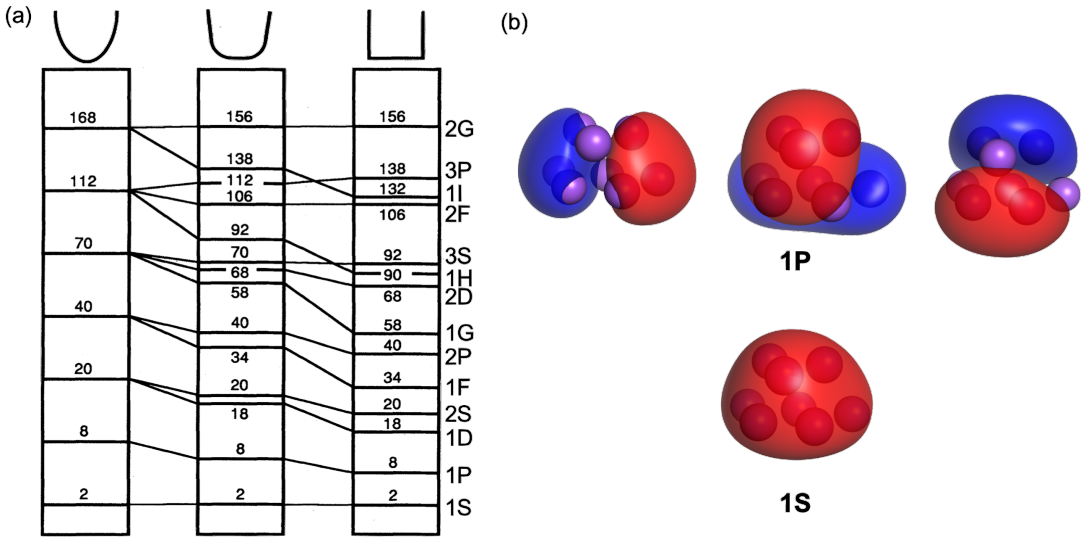

Figure 1.4. (a) Schematic images of jellium potentials with a harmonic, an intermediate, and a square-well shape. The number of total electrons to fill superatomic orbitals is also shown. (b) Typical images of superatomic 1S and 1P orbitals. (a) Adapted with permission from ref. 16. Copyright 1993 American Physical Society.

1P, 1D,… (Figure 1.4). From this similarity, simple metal clusters can be viewed as "superatoms".

The superatomic concept is also applicable for clusters of other metals having s or p valence electrons. For example, Al atom with the electron configuration of $[Ne](3s)^2(3p)^1$ donates valence 3*e* for electronic shell of Al_n. As a result, the closed shell is formed in Al_{13}^- (40*e*) and in Al_{23}^- (70*e*) having the electron configurations of $(1S)^2(1P)^6(1D)^{10}(1S)^2(1F)^{14}(2P)^6$ and $(1S)^2(1P)^6(1D)^{10}(1S)^2(1F)^{14}(2P)^6(1G)^{18}(2D)^{10}(3S)^2$, respectively. The magic stability of Al_{13}^- and Al_{23}^- is confirmed by reaction and PE spectroscopy in the gas phase. Under O_2 gas flow in a cluster source, only Al_{13}^- and Al_{23}^- can survive while other Al_n^- clusters undergo combustion with O_2 (Figure 1.5a).[21] The EAs of Al_{13}^0 (39*e*) and Al_{23}^0 (69*e*) are specifically high compared with those of adjacent

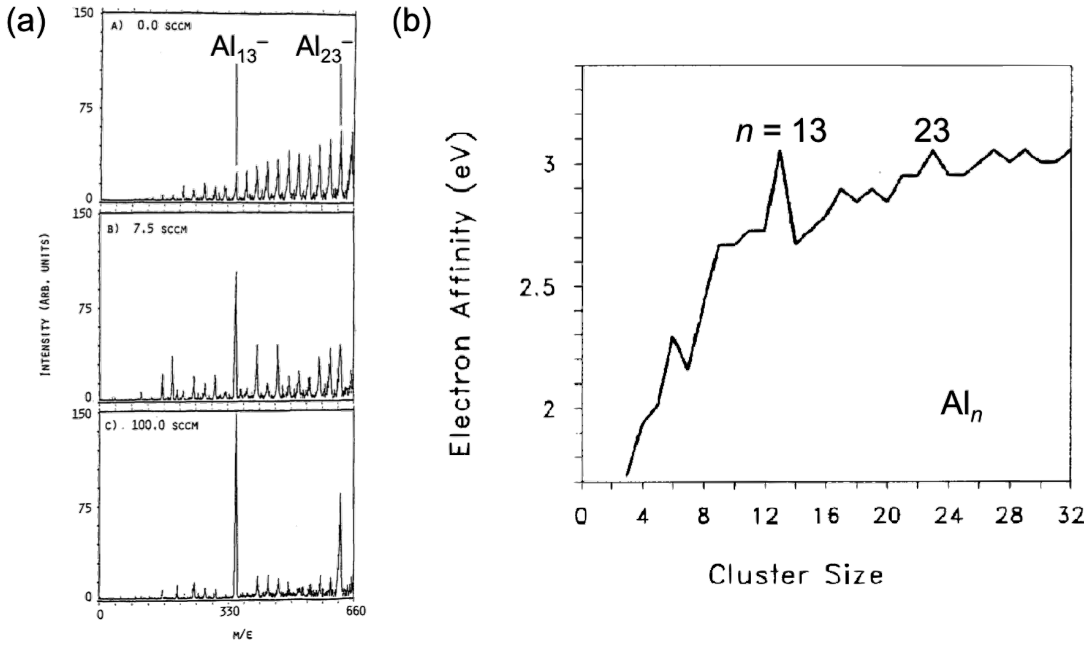

Figure 1.5. (a) Mass spectra of Al_n^- with and without O_2 gas in a cluster source. Flow rate of O_2 gas is increased from top to bottom panels. (b) EAs of Al_n^0 plotted for cluster size. (a) Adapted with permission from ref. 21. Copyright 1989 American Institute of Physics. (b) Adapted with permission from ref. 22. Copyright 1988 Elsevier.

Al_n because the corresponding anions form a closed electronic shell at 40*e* and 70*e*, respectively (Figure 1.5b).[22] Coinage metal clusters of Group 11 (Cu, Ag, Au) also form electronic shell in a similar way of alkali metal clusters because the number of their valence s electrons (1*e*) is same each other. In the mass spectra of $Cu_n^{+/-}$, $Ag_n^{+/-}$, and $Au_n^{+/-}$, the magic number is observed when the number of electrons is 8, 20, 34, 58...[23,24] EAs of Cu_n^0, Ag_n^0, and Au_n^0 take the specifically small values at n = 8, 20, 34, 40, 58…(Figure 1.6).[15] These results indicate that the electronic shells of coinage metal clusters are closed with 8*e*, 20*e*, 34*e*, 40*e*, 58*e*… as in the cases of Na and K clusters.[17,18]

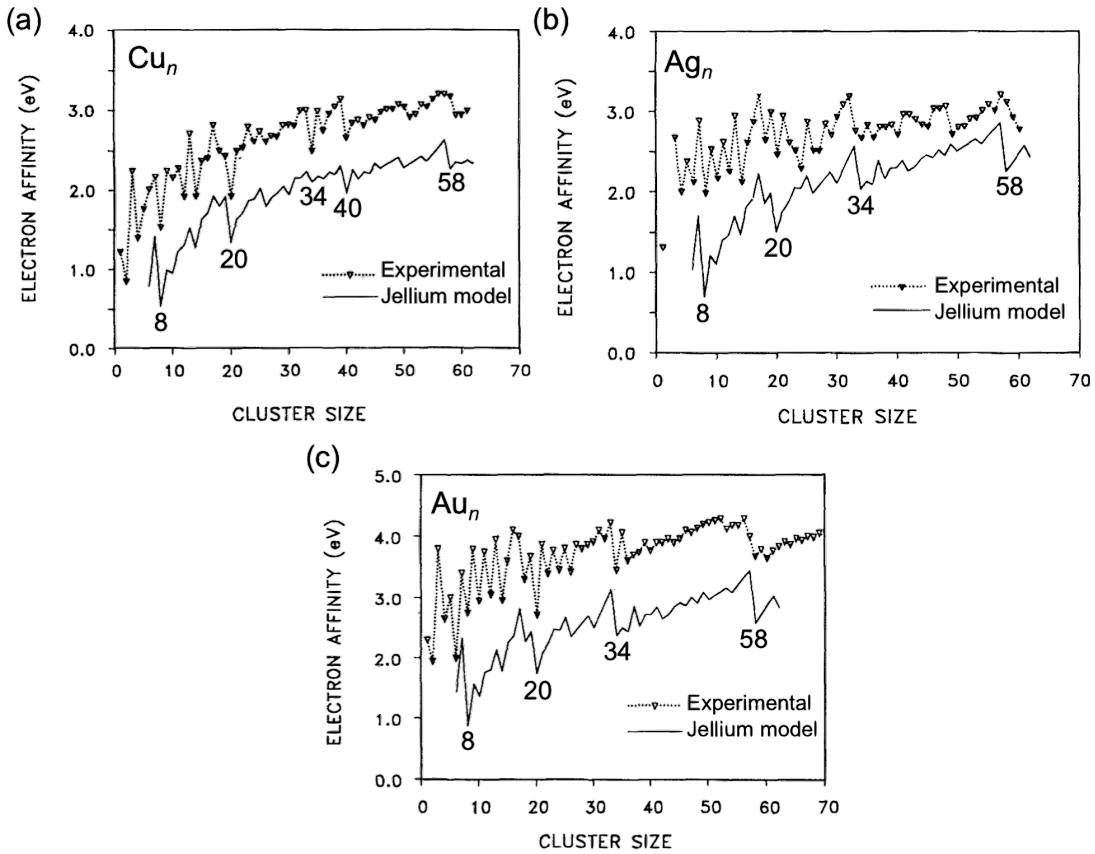

Figure 1.6. EAs of (a) Cu_n^0, (b) Ag_n^0, and (c) Au_n^0 plotted against the cluster size. The triangles and solid lines represent the experimental values and the calculated values by jellium model, respectively. Adapted with permission from ref. 15. Copyright 1992 American Institute of Physics.

The above studies on isolated superatoms suggest that their stability is majorly governed by their electronic shell structure.

In addition to the size specificity, superatom has an internal structure in contrast to the conventional atom. When a spherical superatom deforms, degenerated superatomic orbitals split in energy due to the Jahn-Teller effect (Figure 1.7).[25,26] For example, the compression from one direction gives an oblate superatom and destabilizes some of 1P, 1D, 1F… orbitals along the short axis. As a result, the number of electrons for shell closing becomes 2*e*, 6*e*, 14*e*, 22*e*… (Figure 1.7, left). On the other hand, when a spherical superatom is elongated along one direction to form a prolate superatom, superatomic

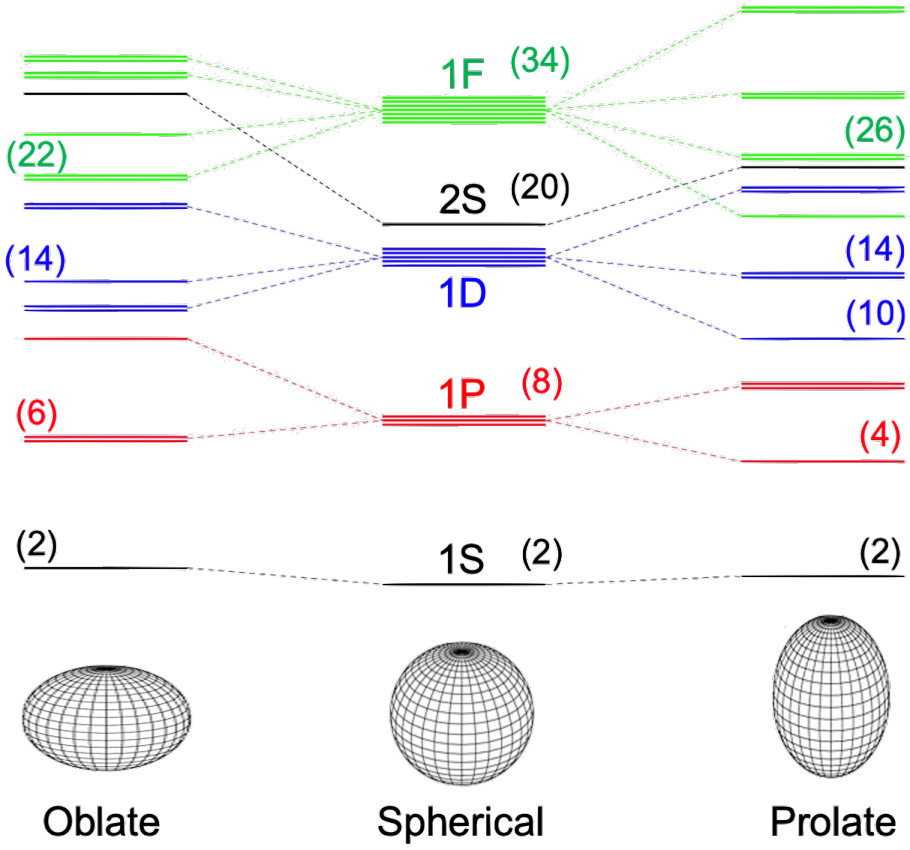

Figure 1.7. Schematic illustration of the Jahn-Teller splitting of superatomic orbitals in an oblate and prolate superatom. The number of parentheses represents the number of electrons for closing electronic shell.[25,26]

orbitals along the long axis are stabilized and electronic shell is closed with 2*e*, 4*e*, 10*e*, 14*e*, 26*e*… (Figure 1.7, right). These phenomena indicate that the electronic structure of superatoms can be controlled by their shape. In addition, due to the ultraminiaturization, thermal behaviors of superatoms are different from those of bulk metals. Au superatoms have much lower melting point than that of bulk state[27] and take some structural isomers which are energetically close each other (Figure 1.1).[13] During the isomerization, the melting of Au superatoms initiates at their surface and propagates to inner part according to the theoretical simulation.[28] This result indicates that there is a hierarchy of the bond stiffness; the surface Au–Au bonds are softer than the internal Au–Au bonds. Such thermal characters of superatoms would affect the temperature dependance of their physicochemical properties. By tuning their soft surface, we can introduce the chirality and promote their reactivity. For these unique features, metal superatoms have a high potential as a building unit of novel functional materials.

1.2.2. Stabilized superatoms

Because metal superatoms in a naked form easily aggregate into bulk metals, stabilization is necessary to utilize them as a new class of materials. For this purpose, superatoms of coinage metal (Cu, Ag, Au) has been intensively studied because they are more stable and less toxic compared with other metals.[29,30] There are three methods to stabilize superatoms: stabilization by polymers,[31,32] immobilization on solid supports,[33] and protection by ligands (Figure 1.8).[34,35] In polymer stabilization, the long backbone and multiple coordination of polymers prevent the diffusion and aggregation of superatoms. Polymer-stabilized superatoms has a partially exposed surface due to the steric demand of polymers and can be applied for catalysis, but the precise control of their

Figure 1.8. Schematic illustrations of three stabilization methods of superatoms.

size is challenging.[31,32,36] Immobilization on solid supports is practically beneficial for catalytic use because it can be easily collected by filtration and be reused after the catalytic reactions.[33,36] It is also expected that the electronic and geometric structures of superatoms are modulated by interactions with various supports.[37,38] Ligand-protection by organic ligands such as phosphines (R_3P), thiolates (RS), alkynyls (RC≡C), *N*-heterocyclic carbenes (NHC), and so on is the most versatile stabilization method. Due to the fully passivation of the surface, ligand-protected superatoms are quite stable and single-sized species can be obtained by applying various purification techniques such as chemical etching, fractional precipitation, liquid chromatography, and gel electrophoresis.[39] We can characterize thus isolated ligand-protected superatoms in various ways. For example, information about their size, composition, and charge state is obtained by mass spectrometry and their electronic structure is studied by optical spectroscopy and electrochemical measurements. Single crystal X-ray diffractometry quantitatively determines their geometric structure. Therefore, we can correlate the size/structure with the properties of ligand-protected superatoms. Because of these advantages, extensive studies on ligand-protected coinage metal superatoms have been conducted to date.[34,35] Especially, the field of ligand-protected Au superatoms has been developed in the last two decades while that of Ag and Cu superatoms has been emerging

recently.

In the electron counting rule of ligand-protected superatoms, we should consider the contribution of ligands in addition to the constituent metal atoms. Häkkinen and colleague have proposed that the formal number of valence electrons (n^*) in ligand (L)-protected metal (M) superatoms having z charge $[M_xL_y]^z$ is calculated as follows:[40]

$$n^* = Ax + By - z \tag{1.6}$$

where A and B are the number of valence electrons supplied from the constituent atoms and the ligands, respectively. A is one for Cu, Ag, and Au and B takes 0 in neutral ligands such as R_3P and NHC, whereas it takes –1 in anionic ligands such as RS and RC≡C.[40]

Numerous characterization results up to now show that magic-sized superatoms have a common core structure independent on the ligands and the composition. For example, an icosahedral (Ih) Au_{13} is one of the ubiquitous superatomic core and observed in many clusters such as $[Au_{13}(R_2P\text{^}PR_2)_5Cl_2]^{3+}$ ($R_2P\text{^}PR_2$ = diphosphine),[41,42] $[Au_{19}(Hdppa)_3(C{\equiv}CPh)_9]^{2+}$ (Hdppa = *N*,*N*-bis(diphenylphosphino)amine, PhC≡CH = phenylacetylene),[43] and $[Au_{25}(SR)_{18}]^-$ (refs. 44–48) in which $n^* = 8$ according to eq 1.6 (Figure 1.9a). Theoretical calculation showed that the Ih Au_{13} core with $n^* = 8$ has a closed electron configuration with $(1S)^2(1P)^6$ (Figure 1.9b).[40,42-44,49,50] A spherical Au_{79} core with $n^* = 58$ is also observed in $[Au_{102}(SR)_{44}]^0$ and $[Au_{103}S_2(SNap)_{41}]^0$ (NapSH = 2-naphthalenethiol)[51-53] and exhibit the shell closing with an electron configuration of $(1S)^2(1P)^6(1D)^{10}(2S)^2(1F)^{14}(2P)^6(1G)^{18}$ (Figure 1.10).[40,49] These results indicate that the stability of ligand-protected superatoms is also explained by the valence electronic structure as in the case of naked superatoms.

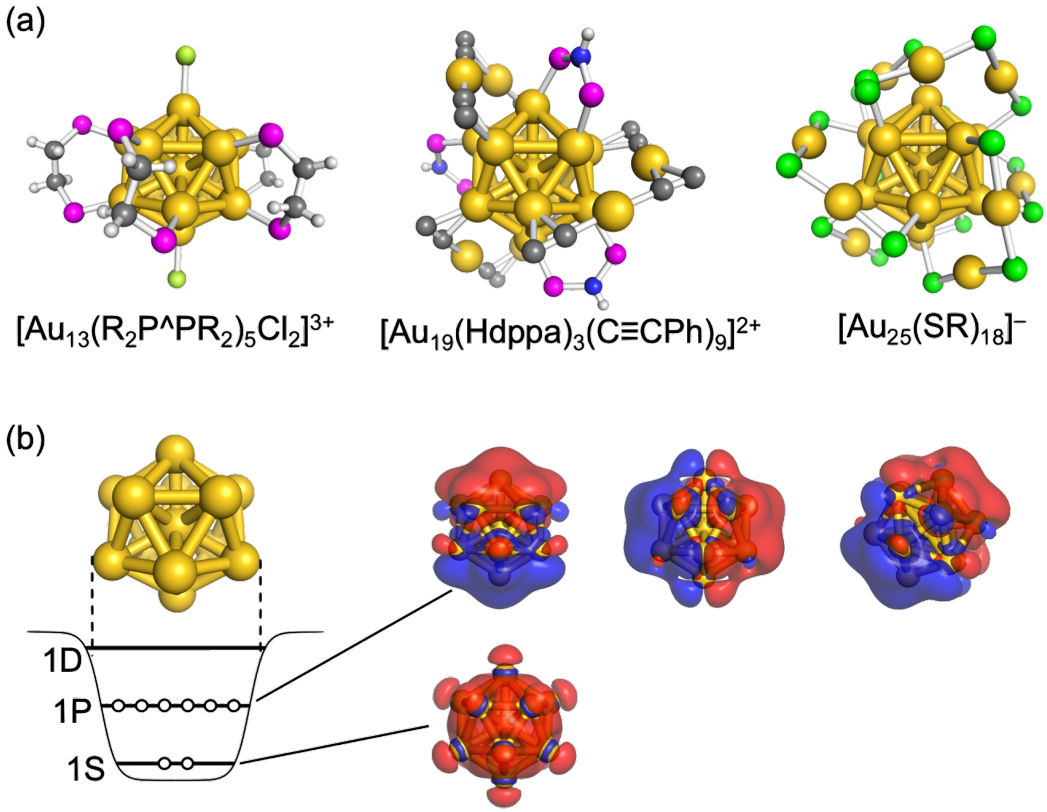

Figure 1.9. (a) Single crystal X-ray structures of $[Au_{13}(R_2P\text{^}PR_2)_5Cl_2]^{3+}$, $[Au_{19}(Hdppa)_3(C\equiv CPh)_9]^{2+}$, and $[Au_{25}(SR)_{18}]^-$.[41-48] Au_{13} core is highlighted by yellow Au–Au bonds. Side chains of ligands are omitted for clarity. (b) Schematic jellium potential of Au_{13}^{5+} core. Superatomic 1S and 1P orbitals in Au_{13}^{5+} are also shown. Color code: yellow (Au); magenta (P); limon (Cl); gray (C); blue (N); white (H); green (S).

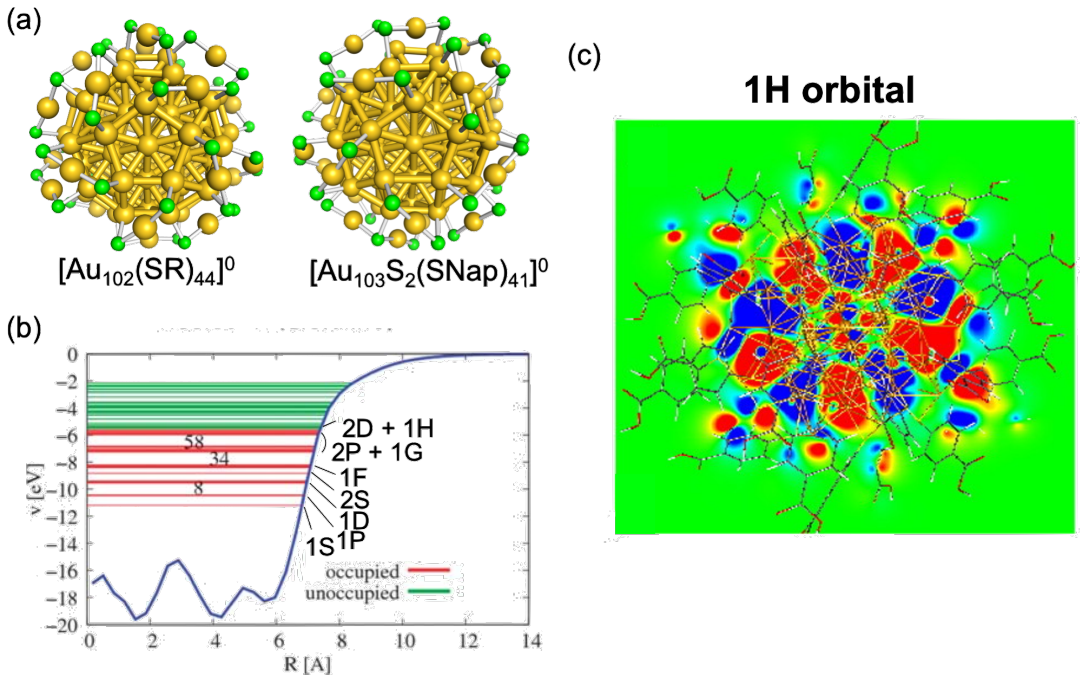

Figure 1.10. (a) Single crystal X-ray structures of $[Au_{102}(SR)_{44}]^0$ and $[Au_{103}S_2(SNap)_{41}]^0$.[51-53] Spherical Au_{79} core is highlighted by yellow Au–Au bonds. Side chains of ligands are omitted for clarity. Color code: yellow (Au); green (S). (b) Radially averaged Kohn-Sham potential of spherical Au_{79}^{21+} core. The occupied and unoccupied superatomic orbitals are depicted as red and green lines, respectively. (c) The lowest unoccupied superatomic 1H orbital of theoretically optimized $[Au_{102}(SPh\text{-}4\text{-}COOH)_{44}]^0$ (HOOC-4-PhSH = 4-mercaptobenzoic acid). (b) Adapted with permission from ref. 49. Copyright 2008 Royal Society of Chemistry. (c) Adapted with permission from ref. 40. Copyright 2008 National Academy of Sciences.

1.3. Ligand effects on Au superatoms

In ligand-protected Au superatoms, ligand does not just protect Au cores, but is one of the important structural factors that directly affects their structures, stability, and physicochemical properties. Eq 1.6 is ascribed to that ligands adjust n^* value of the Au core and close the electronic shell of superatoms as observed in an Ih Au_{13} with $n^* = 8$ and a spherical Au_{79} with $n^* = 58$.[40,49] The optical properties of superatoms are significantly affected by the protecting ligands. For example, $[Au_{13}(R_2P\text{^}PR_2)_5Cl_2]^{3+}$,

$[Au_{19}(Hdppa)_3(C{\equiv}CPh)_9]^{2+}$, and $[Au_{25}(SR)_{18}]^{-}$ having the same superatomic Ih Au_{13} core show different optical absorption spectra (Figure 1.11).[41-43,45-48,54] Protection with alkynyl ligands induces the delocalization of superatomic orbitals over them and modulates the optical response of the superatoms.[55-57] Thermal stability of Au superatoms is enhanced by introducing NHC ligands having a high affinity toward Au.[58-61] In phosphine-protected $[Au_{11}(PPh_3)_8Cl_2]^{+}$ (Ph_3P = triphenylphosphine), just one replacement of Ph_3P with NHC significantly promotes its thermal stability (Figure 1.12).[59] These examples show that the structures, properties, and stability of Au superatoms are tuned by various ligands.

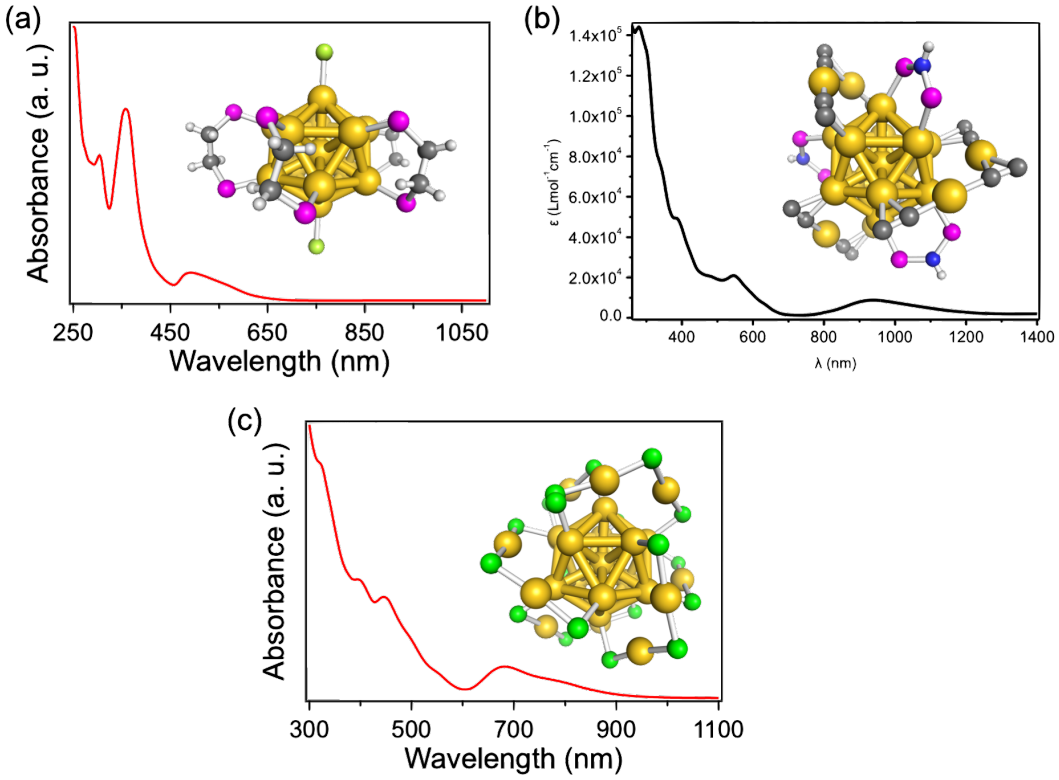

Figure 1.11. Optical absorption spectra of (a) $[Au_{13}(R_2P\text{^}PR_2)_5Cl_2]^{3+}$, (b) $[Au_{19}(Hdppa)_3(C{\equiv}CPh)_9]^{2+}$, and (c) $[Au_{25}(SR)_{18}]^{-}$.[41-43,45-48,54] X-ray structure of each cluster is also shown in the inset. Au_{13} core is highlighted by yellow Au–Au bonds. Side chains of ligands are omitted for clarity. Color code: yellow (Au); magenta (P); limon (Cl); gray (C); blue (N); white (H); green (S). (b) Adapted with permission from ref. 43. Copyright 2015 American Chemical Society.

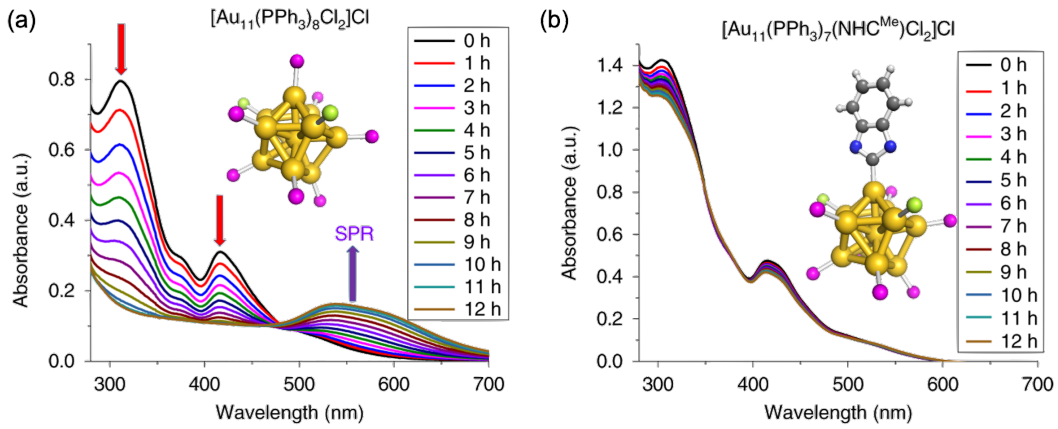

Figure 1.12. Time course optical absorption spectra of (a) $[Au_{11}(PPh_3)_8Cl_2]^+$ and (b) $[Au_{11}(PPh_3)_7(NHC^{Me})Cl_2]^+$ (NHC^{Me} = 1,3-dimethylbenzimidazolin-2-ylidene) in pentanol at 70 ºC. Inset shows X-ray structure of each cluster. Au_{11} core is highlighted by yellow Au–Au bonds. Side chains of ligands are omitted for clarity. Color code: yellow (Au); magenta (P); limon (Cl); gray (C); blue (N); white (H). Adapted with permission from ref. 59. Copyright 2019 Nature Publishing Group.

The ligand conformation and inter-ligand interactions also modify the structures and properties of Au superatoms. Multidentate ligands can make a chiral network and the chirality is transferred to superatomic core through Au–ligand bonds.[62-65] For example, the Au_8 superatom protected by the chiral diphosphine of *R*/*S*-BINAP (BINAP = 2,2'-bis(diphenylphosphino)-1,1'-binaphthyl) has a chiral structure (Figure 1.13a, left).[66] The formation of chiral superatomic cores using achiral ligands has been demonstrated especially in thiolate-protected Au superatoms.[62-65] $Au_{38}(SEtPh)_{24}$ (PhEtSH = 2-phenylethanethiol) has an enantiomeric pair because bidentate Au-SEtPh oligomers make a chiral configuration on the bi-icosahedral Au_{23} core (Figure 1.13a, right).[67] These superatoms show circular dichroism (CD) in the optical transition within a superatomic Au core. The photoluminescence (PL) intensity of Au superatoms is enhanced as a result of core rigidification by ligands.[68] Partial ligand exchange of $[Au_{23}(ScHex)_{16}]^-$ (cHexSH = cyclohexanethiol) with bis(diphenylphosphino)methane (dppm) increases its PL

quantum yield (QY) from 0.4 % to 3 % (Figure 13b, left). This result indicates that the replacement of cHexS ligand with short dppm rigidifies the Au core and suppresses the non-radiative relaxation processes (Figure 1.13b, left).[69,70] Accumulation of CH–π and/or π–π interactions also rigidifies an Au core. For example, the PLQY of the NHC-protected $[Au_{13}(NHC^{Bn})_9Cl_3]^{2+}$ (NHC^{Bn} = 1,3-dibenzylbenzimidazolin-2-ylidene) is relatively high (7 %) and is promoted to 16 % in $[Au_{13}(NHC^{Np})_9Cl_3]^{2+}$ (NHC^{Np} = 1,3-di(napthalen-2-ylmethyl)benzimidazolin-2-ylidene) with an extended π system in the side chains (Figure 1.13b, right).[60] Indeed, there are CH–π and/or π–π interactions between the NHC ligands in the crystal structure of $[Au_{13}(NHC^{Bn})_9Cl_3]^{2+}$.[60] The core size and structure of superatoms are dependent on the ligand bulkiness.[71] By ligand exchange with 2,4-dimethylbenzenethiol (Me_2PhSH), $[Au_{43}(ScHex)_{25}]^0$ is converted to $[Au_{44}(SPhMe_2)_{26}]^0$ and vice versa associated with the structural transformation of Au_{29} core (Figure 1.13c).[72,73] The reversible size/structure transformation by ligand exchange is also observed in $[Au_{44}(SPhMe_2)_{26}]^0$ having the Au_{29} core and $[Au_{44}(SPh\textit{t}Bu)_{28}]^0$ (*t*BuPhSH = 4-*tert*-butylbenzenethiol) having the Au_{26} core (Figure 1.13c).[73,74] It is indicated that the size and structure of superatomic core change by the difference of steric repulsion between ligands; cHexS (secondary), Me_2PhS (ortho- and para-substituted aryl), and *t*BuPhS (para-substituted aryl) have a different steric demand in the vicinity of the core. These reported results suggest that the structures and physicochemical properties of Au superatoms can be tuned by controlling the conformation of ligands and inter-ligand interactions (dispersive interaction, CH–π and/or π–π interactions, hydrogen bonding, steric repulsion).

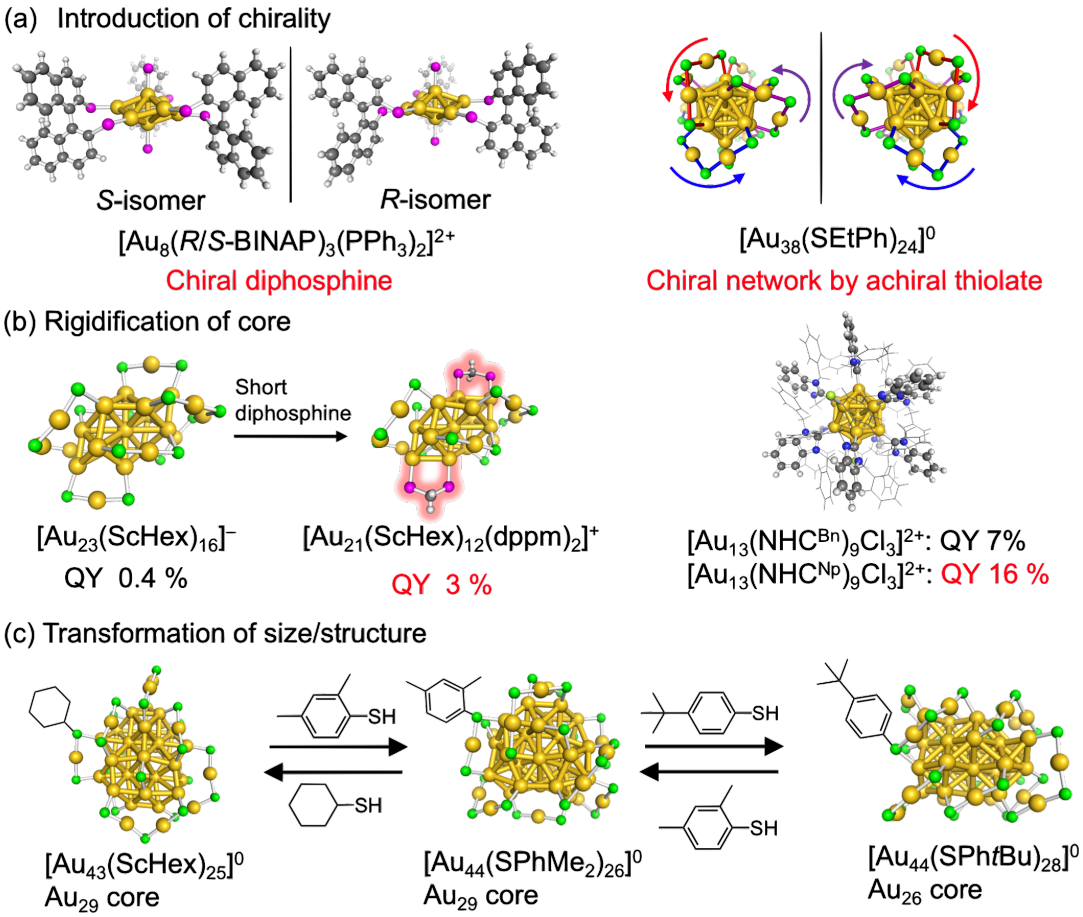

Figure 1.13. Effects of the ligand conformation and the inter-ligand interactions. (a) The structure of enantiomeric pair of $[Au_8(R/S\text{-BINAP})_3(PPh_3)_2]^{2+}$ and $[Au_{38}(SEtPh)_{24}]^0$.[66,67] Ph and PhEt groups are omitted for clarity. (b) Atomic structure of $[Au_{23}(ScHex)_{16}]^-$, $[Au_{21}(ScHex)_{12}(dppm)_2]^+$, and $[Au_{13}(NHC)_9Cl_3]^{2+}$.[60,69,70] Side chains in ligands are omitted or shown as wireframe for clarity. PLQY of each cluster is also shown. (c) Scheme of size/structure transformation by ligand exchange among $[Au_{43}(ScHex)_{25}]^0$, $[Au_{44}(SPhMe_2)_{26}]^0$, and $[Au_{44}(SPhtBu)_{28}]^0$.[72-74] X-ray structure of each cluster is also shown. Only one ligand is schematically shown for clarity. Superatomic Au core is highlighted by yellow Au–Au bonds. Color code: yellow (Au); magenta (P); gray (C) white (H): green (S); blue (N); limon (Cl).

1.4. Aim and outline of the thesis

As explained above, the ligand conformation and inter-ligand interactions affect the structures and properties of Au superatoms. Therefore, until now, many ligand-protected Au superatoms have been synthesized using various ligands.[29,30,34,35] However, the size and composition of superatoms changes dependent on the ligands. The independent discussion of the effects by ligand tail groups is difficult. It is essential to synthesize Au superatoms protected by different ligands while keeping their size and composition. In addition, to tune the properties of ligand-protected superatoms, the tail group of ligands should be intendedly designed to utilize their conformation and the interactions between them.

In this thesis, I studied how the structures of ligand tail groups affect the structures and properties of Au superatoms. To this end, I chose a ubiquitous RS-protected Au superatom $Au_{25}(SR)_{18}$ as a platform. $Au_{25}(SR)_{18}$ is one of the representative Au superatoms and has an isotropic Ih Au_{13} core fully protected by six oligomers of $Au_2(SR)_3$ (Figures 1.9a and 1.11c). It exhibits a closed superatomic electron configuration with $(1S)^2(1P)^6$ when the charge is –1 (Figure 1.9b).[44,45,50] As ligands, I herein used two types of bulky thiols; *N*-2-(mercaptopropionyl)glycine (PGSH) and cHexSH with a secondary α-carbon next to S atoms (Figure 1.14a) and the Fréchet-type dendritic thiols (DenSH) with benzyloxy groups up to second generation (Figure 1.14b).[75,76] In Chapter 2, I synthesized and characterized $[Au_{25}(SPG)_{18}]^-$. Its optical absorption spectrum is significantly different from that of conventional $[Au_{25}(SEtPh)_{18}]^-$ even though the same composition of Au and RS.[44,45] Instead, its profile was similar to that of $[Au_{23}(ScHex)_{16}]^-$ with an anisotropic Au_{13} core (Figure 1.14b).[77] The optical gap of the highest occupied molecular orbital (HOMO) and the lowest unoccupied molecular orbital (LUMO) in

$[Au_{25}(SPG)_{18}]^-$ was 1.8 eV, larger than that in conventional $[Au_{25}(SEtPh)_{18}]^-$ (1.3 eV) and comparable with that of $[Au_{23}(ScHex)_{16}]^-$ (1.9 eV). Extended X-ray absorption fine structure (EXAFS) also showed that the core of $[Au_{25}(SPG)_{18}]^-$ was different from an Ih Au_{13}, but took an anisotropic shape like that in $[Au_{23}(ScHex)_{16}]^-$.[77] According to the experimental results, I constructed the model structures of $[Au_{25}(SPG)_{18}]^-$ based on the crystal structure of $[Au_{23}(ScHex)_{16}]^-$.[77] Density functional theory (DFT) calculations on the model structures indicated that the HOMO-LUMO gap is widened by the reordering of superatomic orbitals in the anisotropic core of $[Au_{25}(SPG)_{18}]^-$ to form an electron configuration of $(1S)^2(1P)^4(1D)^2$ (Figure 1.14a). In Chapter 3, $[Au_{25}(ScHex)_{18}]^0$ with 7*e* was synthesized and its reduction behavior was studied. It is reported that conventional $[Au_{25}(SEtPh)_{18}]^0$ (7*e*) having a Jahn-Teller distorted Ih Au_{13} core is reduced to $[Au_{25}(SEtPh)_{18}]^-$ (8*e*) having an isotropic Ih Au_{13} core by 1 equiv of $NaBH_4$.[78-80] $[Au_{25}(ScHex)_{18}]^0$ had a similar core structure to $[Au_{25}(SEtPh)_{18}]^0$, but was not reduced by 1 equiv of $NaBH_4$. This result indicated that $[Au_{25}(ScHex)_{18}]^0$ had resistance to the formation of a closed shell with 8*e* (Figure 1.14a). In the X-ray structure of $[Au_{25}(ScHex)_{18}]^0$, there were close contacts between the cHex groups and the oligomer motifs of $Au_2(ScHex)_3$ in the ligand layer. It was suggested that the steric hinderance of the cHexS ligands inhibit the structural transformation of a distorted Au_{13} core to an isotropic one and thus the reduction of $[Au_{25}(ScHex)_{18}]^0$ was retarded. In Chapter 4, DenSH with benzyloxy groups were synthesized to make CH–π and/or π–π interactions in ligand layer.[75,76] I introduced DenSH into the different structure of superatoms by the ligand-exchange reaction and studied how their PL response was changed by DenS ligands. The target superatoms are $[Au_{25}(SEtPh)_{18}]^-$ with an isotropic Ih Au_{13} core[44,45] and $[Au_{23}(ScHex)_{16}]^-$ with an anisotropic Au_{13} core (Figure 1.14b).[77] Both partially

exchanged $[Au_{25}(SEtPh)_{18-x}(SDen)_x]^-$ and $[Au_{23}(ScHex)_{16-x}(SDen)_x]^-$ showed stronger PL than unexchanged $[Au_{25}(SEtPh)_{18}]^-$ and $[Au_{23}(ScHex)_{16}]^-$. This result was ascribed to that CH–π and/or π–π interactions between DenS ligands rigidified the Au cores and suppressed the non-radiative relaxation. The degree of PL enhancement in $[Au_{23}(ScHex)_{16-x}(SDen)_x]^-$ was larger than the case of $[Au_{25}(SEtPh)_{18-x}(SDen)_x]^-$. For DenS ligands, an anisotropic Au_{13} core of $[Au_{23}(ScHex)_{16}]^-$ seemed to be more comfortable to coordinate and form CH–π and/or π–π interactions rather than an isotropic Au_{13} core of $[Au_{25}(SEtPh)_{18}]^-$. In Chapter 5, as a concluding remark, I summarized the works in Chapters 2–4 and discuss the future prospect.

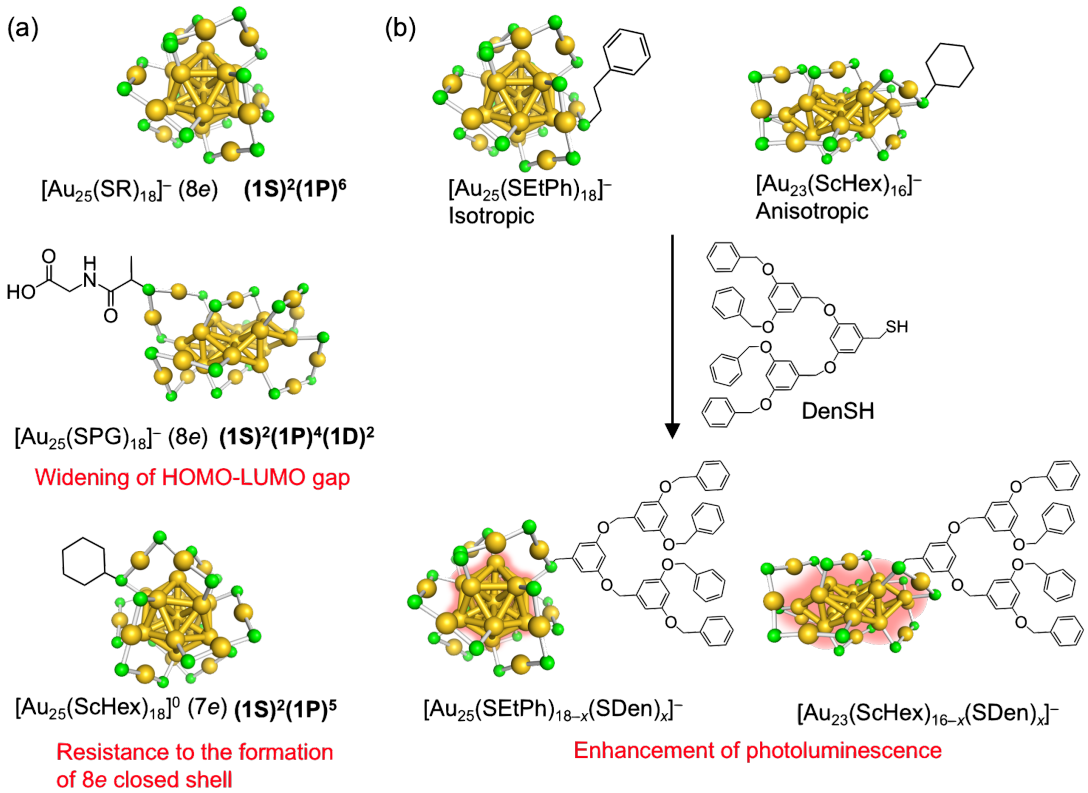

Figure 1.14. Schematic illustrations of the outline of the thesis. (a) A brief comparison of the structures and properties of a conventional $[Au_{25}(SR)_{18}]^-$ with $[Au_{25}(SPG)_{18}]^-$ and $[Au_{25}(ScHex)_{18}]^0$. (b) Introduction of DenSH into $[Au_{25}(SEtPh)_{18}]^-$ and $[Au_{23}(ScHex)_{16}]^-$. The Au core of each cluster is highlighted by yellow Au–Au bonds. Color code: yellow (Au); green (S).

References

1. Van Hardeveld, R.; Hartog, F. *Surf. Sci.* **1969**, *15*, 189.
2. Davis, S. E.; Ide, M. S.; Davis, R. J. *Green Chem.* **2013**, *15*, 17.
3. Arisawa, M. *Chem. Pharm. Bull.* **2019**, *67*, 733.
4. Chen, L.; Qi, Z.; Zhang, S.; Su, J.; Somorjai, G. A. *Catalysts* **2020**, *10*, 858.
5. Zhao, X.; Joseph, B.; Kuhn, J.; Ozcan, S. *iScience* **2020**, *23*, 101082.
6. Petryayeva, E.; Krull, U. J. *Anal. Chim. Acta* **2011**, *706*, 8.
7. Anker, J. N.; Hall, W. P.; Lyandres, O.; Shah, N. C.; Zhao, J.; Van Duyne, R. P. *Nat. Mater.* **2008**, *7*, 442.
8. Vines, J. B.; Yoon, J. H.; Ryu, N. E.; Lim, D. J.; Park, H. *Front. Chem.* **2019**, *7*, 167.
9. Tatsuma, T.; Nishi, H. *Nanoscale Horiz.* **2020**, *5*, 597.
10. Marinkovic, N. S.; Sasaki, K.; Adzic, R. R. *J. Electrochem. Soc.* **2018**, *165*, J3222.
11. Benfield, R. E. *J. Chem. Soc., Faraday Trans.* **1992**, *88*, 1107.
12. Brack, M. *Rev. Mod. Phys.* **1993**, *65*, 677.
13. Iijima, S.; Ichihashi, T. *Phys. Rev. Lett.* **1986**, *56*, 616.
14. Busani, R.; Folkers, M.; Cheshnovsky, O. *Phys. Rev. Lett.* **1998**, *81*, 3836.
15. Taylor, K. J.; Pettiette-Hall, C. L.; Cheshnovsky, O.; Smalley, R. E. *J. Chem. Phys.* **1992**, *96*, 3319.
16. de Heer, W. A. *Rev. Mod. Phys.* **1993**, *65*, 611.
17. Knight, W. D.; Clemenger, K.; de Heer, W. A.; Saunders, W. A.; Chou, M. Y.; Cohen, M. L. *Phys. Rev. Lett.* **1984**, *52*, 2141.
18. Knight, W. D.; de Heer, W. A.; Clemenger, K.; Saunders, W. A. *Solid State Commun.* **1985**, *53*, 445.
19. Saunders, W. A.; Clemenger, K.; de Heer, W. A.; Knight, W. D. *Phys. Rev. B* **1985**, *32*, 1366.
20. Kappes, M. M.; Schär, M.; Röthlisberger, U.; Yeretzian, C.; Schumacher, E. *Chem. Phys. Lett.* **1988**, *143*, 251.
21. Leuchtner, R. E.; Harms, A. C.; Castleman, A. W. *J. Chem. Phys.* **1989**, *91*, 2753.
22. Taylor, K. J.; Pettiette, C. L.; Craycraft, M. J.; Chesnovsky, O.; Smalley, R. E. *Chem. Phys. Lett.* **1988**, *152*, 347.
23. Katakuse, I.; Ichihara, T.; Fujita, Y.; Matsuo, T.; Sakurai, T.; Matsuda, H. *Int. J. Mass Spectrom. Ion Processes* **1985**, *67*, 229.
24. Katakuse, I.; Ichihara, T.; Fujita, Y.; Matsuo, T.; Sakurai, T.; Matsuda, H. *Int. J. Mass Spectrom. Ion Processes* **1986**, *74*, 33.
25. Clemenger, K. *Phys. Rev. B* **1985**, *32*, 1359.
26. Lin, Z.; Slee, T.; Mingos, D. M. P. *Chem. Phys.* **1990**, *142*, 321.

27. Buffat, P.; Borel, J. P. *Phys. Rev. A* **1976**, *13*, 2287.
28. Cleveland, C.; Luedtke, W.; Landman, U. *Phys. Rev. Lett.* **1998**, *81*, 2036.
29. Jin, R.; Zeng, C.; Zhou, M.; Chen, Y. *Chem. Rev.* **2016**, *116*, 10346.
30. Chakraborty, I.; Pradeep, T. *Chem. Rev.* **2017**, *117*, 8208.
31. Hasegawa, S.; Tsukuda, T. *Bull. Chem. Soc. Jpn.* **2020**, DOI: 10.1246/bcsj.20200377.
32. Yamamoto, K.; Imaoka, T.; Tanabe, M.; Kambe, T. *Chem. Rev.* **2020**, *120*, 1397.
33. Yamazoe, S.; Yoskamtorn, T.; Takano, S.; Yadnum, S.; Limtrakul, J.; Tsukuda, T. *Chem. Rec.* **2016**, *16*, 2338.
34. Omoda, T.; Takano, S.; Tsukuda, T. *Small* **2020**, e2001439.
35. Hirai, H.; Ito, S.; Takano, S.; Koyasu, K.; Tsukuda, T. *Chem. Sci.* **2020**, *11*, 12233.
36. Yamazoe, S.; Koyasu, K.; Tsukuda, T. *Acc. Chem. Res.* **2014**, *47*, 816.
37. Liu, X. Y.; Wang, A.; Zhang, T.; Mou, C.-Y. *Nano Today* **2013**, *8*, 403.
38. Liu, L.; Corma, A. *Chem. Rev.* **2018**, *118*, 4981.
39. Negishi, Y.; Hashimoto, S.; Ebina, A.; Hamada, K.; Hossain, S.; Kawawaki, T. *Nanoscale* **2020**, *12*, 8017.
40. Walter, M.; Akola, J.; Lopez-Acevedo, O.; Jadzinsky, P. D.; Calero, G.; Ackerson, C. J.; Whetten, R. L.; Grönbeck, H.; Häkkinen, H. *Proc. Natl. Acad. Sci. U. S. A.* **2008**, *105*, 9157.
41. Shichibu, Y.; Konishi, K. *Small* **2010**, *6*, 1216.
42. Yang, Y.; Zhang, Q.; Guan, Z. J.; Nan, Z. A.; Wang, J. Q.; Jia, T.; Zhan, W. W. *Inorg. Chem.* **2019**, *58*, 3670.
43. Wan, X. K.; Tang, Q.; Yuan, S. F.; Jiang, D. E.; Wang, Q. M. *J. Am. Chem. Soc.* **2015**, *137*, 652.
44. Heaven, M. W.; Dass, A.; White, P. S.; Holt, K. M.; Murray, R. W. *J. Am. Chem. Soc.* **2008**, *130*, 3754.
45. Zhu, M.; Aikens, C. M.; Hollander, F. J.; Schatz, G. C.; Jin, R. *J. Am. Chem. Soc.* **2008**, *130*, 5883.
46. Li, G.; Abroshan, H.; Liu, C.; Zhuo, S.; Li, Z.; Xie, Y.; Kim, H. J.; Rosi, N. L.; Jin, R. *ACS Nano* **2016**, *10*, 7998.
47. Gunawardene, P. N.; Corrigan, J. F.; Workentin, M. S. *J. Am. Chem. Soc.* **2019**, *141*, 11781.
48. Huang, Z.; Ishida, Y.; Yonezawa, T. *Angew. Chem. Int. Ed.* **2019**, *58*, 13411.
49. Häkkinen, H. *Chem. Soc. Rev.* **2008**, *37*, 1847.
50. Akola, J.; Walter, M.; Whetten, R. L.; Häkkinen, H.; Grönbeck, H. *J. Am. Chem. Soc.* **2008**, *130*, 3756.

51. Jadzinsky, P. D.; Calero, G.; Ackerson, C. J.; Bushnell, D. A.; Kornberg, R. D. *Science* **2007**, *318*, 430.
52. Heinecke, C. L.; Ni, T. W.; Malola, S.; Makinen, V.; Wong, O. A.; Häkkinen, H.; Ackerson, C. J. *J. Am. Chem. Soc.* **2012**, *134*, 13316.
53. Higaki, T.; Liu, C.; Zhou, M.; Luo, T. Y.; Rosi, N. L.; Jin, R. *J. Am. Chem. Soc.* **2017**, *139*, 9994.
54. Kang, X.; Chong, H.; Zhu, M. *Nanoscale* **2018**, *10*, 10758.
55. Kobayashi, N.; Kamei, Y.; Shichibu, Y.; Konishi, K. *J. Am. Chem. Soc.* **2013**, *135*, 16078.
56. Sugiuchi, M.; Shichibu, Y.; Nakanishi, T.; Hasegawa, Y.; Konishi, K. *Chem. Commun.* **2015**, *51*, 13519.
57. Konishi, K.; Iwasaki, M.; Sugiuchi, M.; Shichibu, Y. *J. Phys. Chem. Lett.* **2016**, *7*, 4267.
58. Crudden, C. M.; Horton, J. H.; Narouz, M. R.; Li, Z.; Smith, C. A.; Munro, K.; Baddeley, C. J.; Larrea, C. R.; Drevniok, B.; Thanabalasingam, B.; McLean, A. B.; Zenkina, O. V.; Ebralidze, II; She, Z.; Kraatz, H.-B.; Mosey, N. J.; Saunders, L. N.; Yagi, A. *Nat. Commun.* **2016**, *7*, 12654.
59. Narouz, M. R.; Osten, K. M.; Unsworth, P. J.; Man, R. W. Y.; Salorinne, K.; Takano, S.; Tomihara, R.; Kaappa, S.; Malola, S.; Dinh, C. T.; Padmos, J. D.; Ayoo, K.; Garrett, P. J.; Nambo, M.; Horton, J. H.; Sargent, E. H.; Häkkinen, H.; Tsukuda, T.; Crudden, C. M. *Nat. Chem.* **2019**, *11*, 419.
60. Narouz, M. R.; Takano, S.; Lummis, P. A.; Levchenko, T. I.; Nazemi, A.; Kaappa, S.; Malola, S.; Yousefalizadeh, G.; Calhoun, L. A.; Stamplecoskie, K. G.; Häkkinen, H.; Tsukuda, T.; Crudden, C. M. *J. Am. Chem. Soc.* **2019**, *141*, 14997.
61. Smith, C. A.; Narouz, M. R.; Lummis, P. A.; Singh, I.; Nazemi, A.; Li, C. H.; Crudden, C. M. *Chem. Rev.* **2019**, *119*, 4986.
62. Knoppe, S.; Bürgi, T. *Acc. Chem. Res.* **2014**, *47*, 1318.
63. Pelayo, J. J.; Valencia, I.; Garcia, A. P.; Chang, L.; Lopez, M.; Toffoli, D.; Stener, M.; Fortunelli, A.; Garzón, I. L. *Adv. Phys. X* **2018**, *3*.
64. Li, Y.; Higaki, T.; Du, X.; Jin, R. *Adv. Mater.* **2020**, *32*, e1905488.
65. Zhu, Y.; Guo, J.; Qiu, X.; Zhao, S.; Tang, Z. *Acc. Mater. Res.* **2021**, 2, 21.
66. Takano, S.; Tsukuda, T. *J. Phys. Chem. Lett.* **2016**, *7*, 4509.
67. Dolamic, I.; Knoppe, S.; Dass, A.; Bürgi, T. *Nat. Commun.* **2012**, *3*, 798.
68. Kang, X.; Zhu, M. *Chem. Soc. Rev.* **2019**, *48*, 2422.
69. Li, Q.; Luo, T. Y.; Taylor, M. G.; Wang, S.; Zhu, X.; Song, Y.; Mpourmpakis, G.; Rosi, N. L.; Jin, R. *Sci. Adv.* **2017,** *3*, e1603193.

70. Li, Q.; Zhou, M.; So, W. Y.; Huang, J.; Li, M.; Kauffman, D. R.; Cotlet, M.; Higaki, T.; Peteanu, L. A.; Shao, Z.; Jin, R. *J. Am. Chem. Soc.* **2019**, *141*, 5314.
71. Higaki, T.; Zeng, C.; Chen, Y.; Hussain, E.; Jin, R. *CrystEngComm* **2016,** *18*, 6979.
72. Liao, L.; Zhuang, S.; Yao, C.; Yan, N.; Chen, J.; Wang, C.; Xia, N.; Liu, X.; Li, M. B.; Li, L.; Bao, X.; Wu, Z. *J. Am. Chem. Soc.* **2016**, *138*, 10425.
73. Dong, H.; Liao, L.; Wu, Z. *J. Phys. Chem. Lett.* **2017**, *8*, 5338.
74. Zeng, C.; Chen, Y.; Iida, K.; Nobusada, K.; Kirschbaum, K.; Lambright, K. J.; Jin, R. *J. Am. Chem. Soc.* **2016**, *138*, 3950.
75. Hawker, C. J.; Fréchet, J. M. J. *J. Am. Chem. Soc.* **1990**, *112*, 7638.
76. Zhang, L.; Huo, F.; Wang, Z.; Wu, L.; Zhang, X.; Höppener, S.; Chi, L.; Fuchs, H.; Zhao, J.; Niu, L.; Dong, S. *Langmuir* **2000**, *16*, 3813.
77. Das, A.; Li, T.; Nobusada, K.; Zeng, C.; Rosi, N. L.; Jin, R. *J. Am. Chem. Soc.* **2013**, *135*, 18264.
78. Zhu, M.; Eckenhoff, W. T.; Pintauer, T.; Jin, R. *J. Phys. Chem. C* **2008**, *112*, 14221.
79. Zhu, M.; Aikens, C. M.; Hendrich, M. P.; Gupta, R.; Qian, H.; Schatz, G. C.; Jin, R. *J. Am. Chem. Soc.* **2009**, *131*, 2490.
80. Tofanelli, M. A.; Salorinne, K.; Ni, T. W.; Malola, S.; Newell, B.; Phillips, B.; Häkkinen, H.; Ackerson, C. J. *Chem. Sci.* **2016**, *7*, 1882.

Chapter 2.

HOMO-LUMO gap widening in $[Au_{25}(SR)_{18}]^-$ protected by *N*-(2-mercaptopropionyl)glycine

Omoda, T.; Takano, S.; Yamazoe, S.; Koyasu, K.; Negishi, Y.;

Tsukuda, T. *J. Phys. Chem. C* **2018**, *122*, 13199-13204.

2.1. Introduction

The optical property of ligand-protected Au superatoms is dependent on their size. With increasing their size, their optical absorption band is gradually red-shifted.[1] This trend is ascribed to the framework of spherical jellium model.[2] Size increase leads to an increase in the potential volume while retaining the depth of the potential well (Figure 2.1). As a result, superatomic orbitals are more energetically stabilized and the energy gaps between the highest occupied molecular orbitals (HOMOs) and the lowest unoccupied molecular orbitals (LUMOs) are narrowed in the large size of superatoms. When the size of superatoms reaches at a certain critical point, the energy gaps of superatomic orbitals become negligibly small and the metallic behavior emerges. In optical absorption spectra, the peaks by electronic transitions disappear and the localized

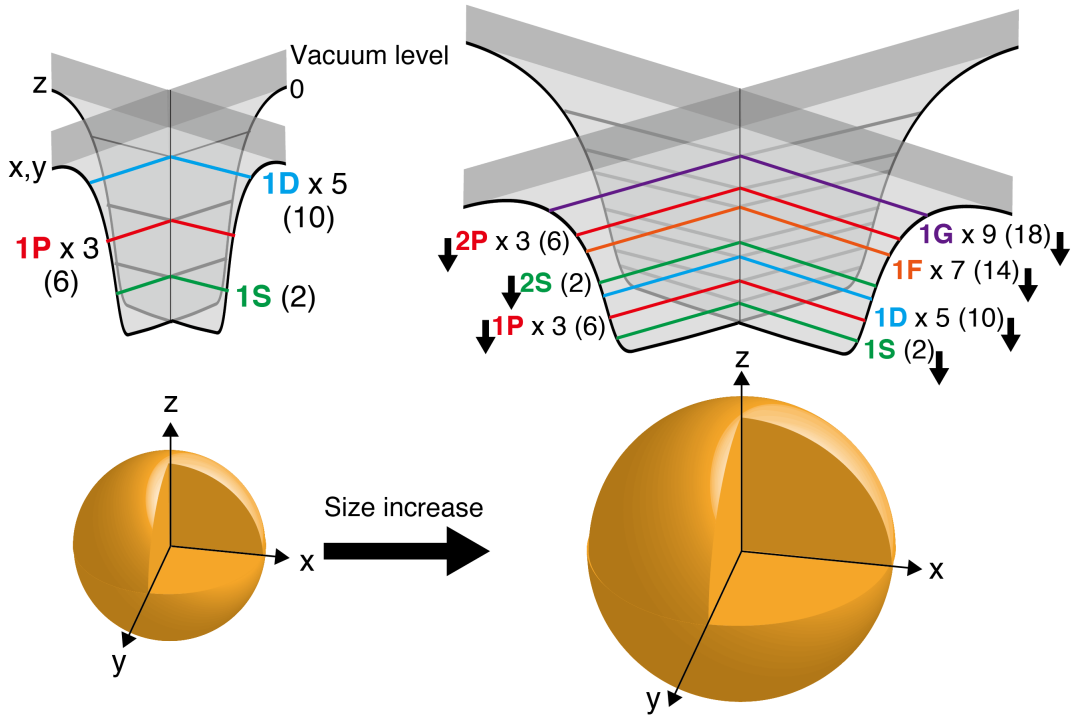

Figure 2.1. Schematic illustration of size effect on a spherical jellium potential. The maximum number of electrons confined in each superatomic orbital is shown in parentheses. Reproduced with permission from ref. 2. Copyright 2020 Wiley-VCH.

surface plasmon resonance (LSPR) band by the oscillation of free electrons is observed in the visible region.[3] In thiolate (RS)-protected Au superatoms, the critical core size of nonmetal-to-metal transition is around Au_{150}–Au_{200} and somewhat depends on measurement methods and ligands.[4,5]

In the small size region, the optical absorption of Au superatoms significantly depends on their atomic structure rather than their size.[1] Some Au superatoms show different optical response even though their size and composition are identical. The typical example is $[Au_9(PPh_3)_8]^{3+}$ (PPh_3 = triphenylphosphine).[6-11] The optical absorption spectrum of $[Au_9(PPh_3)_8]^{3+}$ is significantly changed when solidified with compact counter anions such as NO_3^-. This is because the structural isomerization of $[Au_9(PPh_3)_8]^{3+}$ from a crown to a butterfly motif takes place (Figure 2.2a). Such spectral change is not observed when $[Au_9(PPh_3)_8]^{3+}$ is solidified with large counter anions such as $PMo_{12}O_{40}^{3-}$. Structural isomerization is also reported in other ligand-protected Au superatoms (Figure 2.2). For example, in $[Au_{38}(SEtPh)_{24}]^0$, one isomer has a bi-icosahedral (Ih) Au_{23} core while the other has an Au_{23} core with a capped Ih motif.[12,13] In two isomers of $[Au_{28}(ScHex)_{20}]^0$ (cHexSH = cyclohexanethiol), the same Au_{14} core is protected by $Au_n(ScHex)_{n+1}$ oligomers with different length.[14,15] These pairs of structural isomers show different optical absorption each other (Figures 2.2b and c). Structural isomers showing different optical responses have been also found in $[Au_{23}(C{\equiv}C\textit{t}Bu)_{15}]^0$ (*t*BuC≡CH = *tert*-butylacetylene),[16] $[Au_{36}(SPhMe_2)_{24}]^0$ (Me_2PhSH = 3,5-dimethylbenzenethiol),[17] and $[Au_{42}(SPh\textit{t}Bu)_{26}]^0$ (*t*BuPhSH = 4-*tert*-butylbenezenethiol).[18,19] Especially in thiolate-protected Au superatoms, structural isomers with different thiolate ligands have been reported: $[Au_{21}(S\textit{t}Bu)_{15}]^0$ (*t*BuSH = *tert*-butyl mercaptan) and $[Au_{21}(SAdm)_{15}]^0$ (AdmSH = 1-adamantanethiol),[20,21] $[Au_{28}(ScHex)_{20}]^0$ and $[Au_{28}(SR)_{20}]^0$ (R = *t*BuPh, cyclopentyl

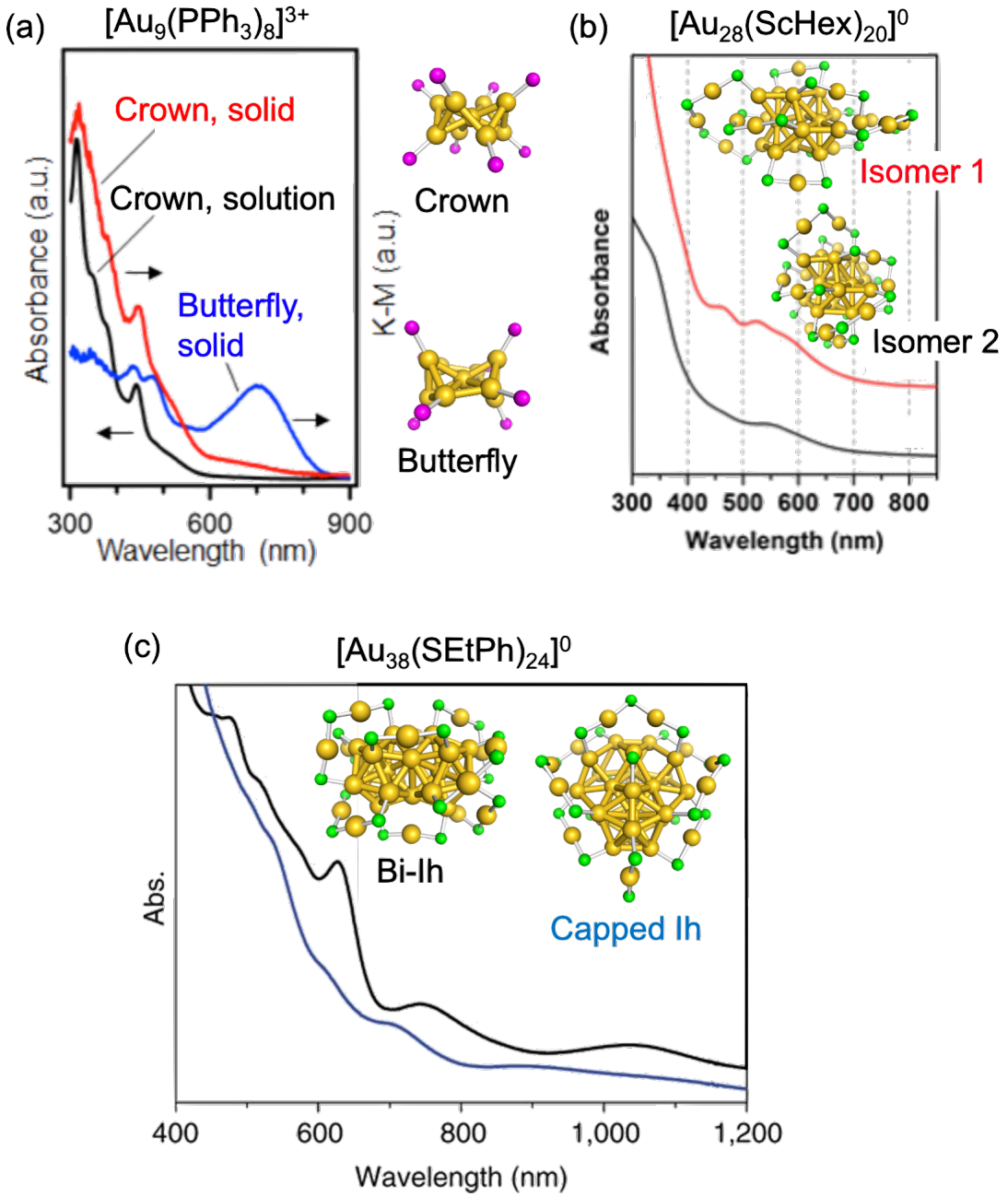

Figure 2.2. (a) Optical absorption and diffuse-reflectance spectra of the structural isomers of $[Au_9(PPh_3)_8]^{3+}$. Optical absorption spectra of the structural isomers of (b) $[Au_{28}(ScHex)_{20}]^0$ and (c) $[Au_{38}(SEtPh)_{24}]^0$. The atomic structure of each isomer is also shown with omitting R groups of ligands for clarity. Color codes: yellow (Au); magenta (P); green (S). (a) Adapted with permission from ref. 11. Copyright 2017 American Chemical Society. (b) Adapted with permission from ref. 15. Copyright 2020 American Chemical Society. (c) Adapted with permission from ref. 13. Copyright 2015 Nature Publishing Group.

(cPen)),[14,15,22] $[Au_{30}(StBu)_{18}]^0$ and $[Au_{30}(SAdm)_{18}]^0$,[23,24] $[Au_{36}(SPhMe_2)_{24}]^0$ and $[Au_{36}(SR)_{24}]^0$ (R = *t*BuPh, Ph, cPen),[17,25-27] $[Au_{42}(SPhtBu)_{26}]^0$ and $[Au_{42}(ScHex)_{26}]^0$,[18,19,28] $[Au_{52}(SPhtBu)_{32}]^0$ and $[Au_{52}(SEtPh)_{32}]^0$.[29,30] These results suggest that the optical absorption of small-sized superatoms is modulated by their structural change induced by the counter ions and ligands.

$[Au_{25}(SR)_{18}]^-$ is a prototypical system in thiolate-protected Au superatoms having an Ih Au_{13} core fully protected by $Au_2(SR)_3$ oligomers with the closed superatomic electron configuration of $(1S)^2(1P)^6$ (Figure 2.3a).[31-33] Although $[Au_{25}(SR)_{18}]^-$ has been synthesized with using various RS ligands up to now,[34] its optical absorption spectrum is almost independent on their R groups. This result indicates that the modulation of optical absorption through the structural isomerization by ligands is not observed in

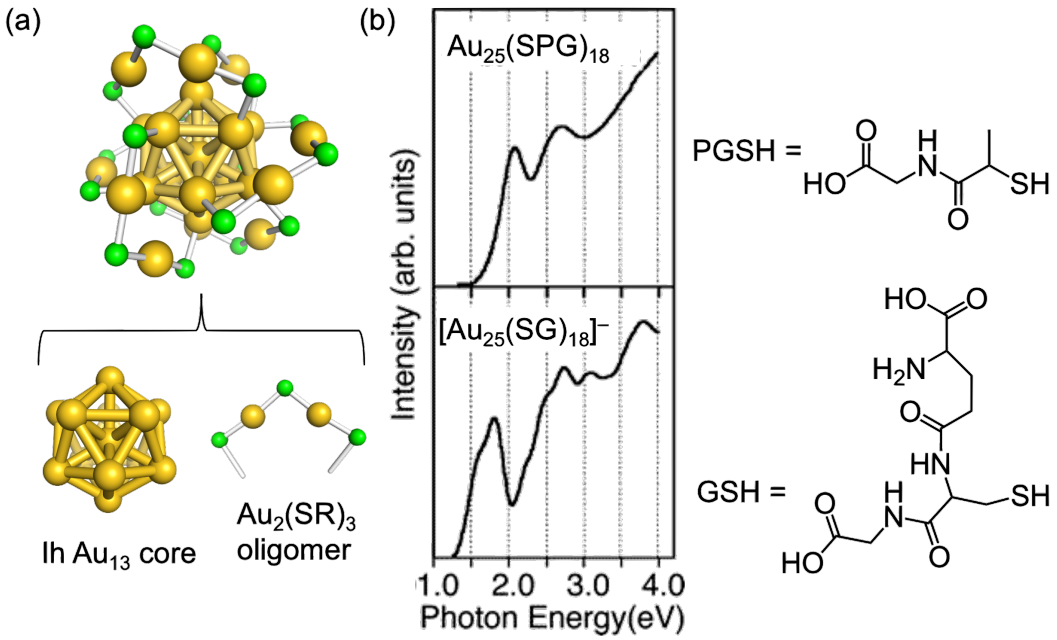

Figure 2.3. (a) Anatomy of $[Au_{25}(SR)_{18}]^-$.[31,32] R group is omitted for clarity. Au_{13} core is highlighted by yellow Au–Au bonds. Color code: yellow (Au); green (S). (b) Optical absorption spectra of $Au_{25}(SPG)_{18}$ and conventional $[Au_{25}(SG)_{18}]^-$ (GSH = glutathione). The structures of PGSH and GSH are also shown. Adapted with permission from ref. 35. Copyright 2006 American Chemical Society.

$[Au_{25}(SR)_{18}]^{-}$.[34] An exception is only found in $Au_{25}(SPG)_{18}$ (PGSH = *N*-2-(mercaptopropionyl)glycine) reported by Negishi *et al*.[35] The optical absorption spectrum of $Au_{25}(SPG)_{18}$ is significantly different from that of conventional $[Au_{25}(SR)_{18}]^{-}$ (Figure 2.3b). This result suggests that the structural isomerization induced by PGS ligand occurs in $[Au_{25}(SR)_{18}]^{-}$. However, no structural characterization of $Au_{25}(SPG)_{18}$ has been conducted ever. In this chapter, I studied the geometric and electronic structures of $Au_{25}(SPG)_{18}$ with the combination of experimental and theoretical techniques. Based on the results, the origin of different optical absorption of $Au_{25}(SPG)_{18}$ from that of conventional $[Au_{25}(SR)_{18}]^{-}$ was discussed.

2.2. Experiment

2.2.1. Chemicals

All chemicals were commercially available and used without further purification. Tetrachloroauric acid tetrahydrate ($HAuCl_4 \cdot 4H_2O$), sodium borohydride ($NaBH_4$), cesium iodide (CsI), acetic acid (AcOH), triethylamine (Et_3N), boron nitride, acrylamide, *N*,*N*'-methylenebis(acrylamide), 2-mercaptopropionic acid (PASH), dichloromethane (DCM), *n*-hexane, methanol (MeOH), ethanol (EtOH), isopropanol (iPrOH), and toluene were purchased from FUJIFILM Wako Pure Chemical Corporation. 2-phenylethanethiol (PhEtSH), cyclohexanethiol (cHexSH), and *N*-(2-mercaptopropionyl)glycine (PGSH) were purchased from Tokyo Chemical Industry. Tetra-*n*-octylammonium bromide (TOABr) was purchased from Sigma-Aldrich. Tetrahydrofuran (THF) was obtained from Kanto Chemical. 1.5 M tris(hydroxymethyl)aminomethane hydrochloride (Tris−HCl) buffer (pH 8.8) and Tris–glycine (Tris = 0.25 M, glycine = 1.92 M) buffer were obtained from Bio-Rad Laboratories. Glycerol was obtained from ICN Biomedicals. Water was

Milli-Q grade (ρ > 18 MΩ·cm).

2.2.2. General

Ultraviolet-visible (UV-vis) absorption spectra were measured by JASCO V-630, V-670, and V-770 spectrophotometers. The raw spectral data as functions of the wavelength could be converted to the energy-dependent data according to the reported procedure.[36] Electrospray ionization (ESI)-mass spectra of $Au_n(SPG)_m$ and $Au_n(SPA)_m$ were measured with using a JEOL JMS-T100LP AccuTOF mass spectrometer. The sample of $Au_{25}(SPG)_{18}$ for ESI-mass spectrometry was prepared by reprecipitation using 2 % acetic acid and EtOH/DCM = 1:1 (v/v) to remove the counter cation of $Tris^+$ prior to the measurement. A 50 % water/MeOH (v/v) dispersion of $Au_n(SPG)_m$ and $Au_n(SPA)_m$ were mixed with 0.1 vol % of Et_3N at a concentration of 0.5 and 1 mg/mL, respectively. The mixed dispersion was electrosprayed in a negative-ion mode. The temperatures of a desolvation chamber and an orifice were 100–150 °C. The mass spectra were calibrated by mass spectra of $[(CsI)_nI]^-$ as an external standard.

2.2.3. Synthesis

2.2.3.1. Crude Au:SPG clusters

The crude mixture of Au:SPG clusters were prepared by the reported method with modification.[35] PGSH (1.5 mmol) was added to the EtOH solution of $HAuCl_4·4H_2O$ (5 mM, 50 mL). The mixed solution was stirred for 2.5 h at room temperature. The colorless solution was then cooled to ∼0 °C in an ice bath for 30 min. To this solution, an ice-cooled aqueous solution of $NaBH_4$ (0.2 M, 12.5 mL) was dropwise added for ∼10 min. The sticky black precipitate that formed was dissolved in a Tris–HCl buffer solution (1.5

M, 2 mL), collected, and precipitated using excess EtOH. After being washed with EtOH three times, the black precipitate was dried in vacuo and used for further experiments.

2.2.3.2. Annealing of Au:SPG clusters

Crude Au:SPG clusters as prepared (1.4 mg) were dissolved in water (25 mL). 5 mL of this solution was stirred for 24 h at r.t., 40 ºC, and 50 ºC. After that, each solution was concentrated by centrifugal ultrafiltration (Vivaspin 20; Vivascience; MWCO = 5 kDa) and then dried by a lyophilizer (FDU-2000; EYERA).

2.2.3.3. $Au_{25}(SPG)_{18}$

The crude Au:SPG clusters were separated by polyacrylamide gel electrophoresis (PAGE)[35,37] using a single (NA-1120, Nihon Eido) or a double (BE-S12, Bio Craft) slab gel units with a size of 3t × 160 × 160 mm. The total concentration of acrylamide in the preparative gel and the stacking gel was 30 and 3 wt%, respectively (acrylamide:*N*,*N*'-methylenebis(acrylamide) = 93:7). The crude Au:SPG clusters were dissolved in a 2.5% (v/v) aqueous solution of glycerol and the sample dispersion (40 mg/mL, 300 μL) was loaded for a single gel. Tris–glycine (Tris = 25 mM, glycine = 192 mM) buffer was used as the eluting buffer. The Au:SPG clusters were eluted for 10.5 h at a constant voltage mode (150 V) in an incubator kept at 5 °C to suppress the decomposition of the clusters. After the elution, Au:SPG clusters were separated into six fractions. Green fraction of $Au_{25}(SPG)_{18}$ was cut out, crushed using a spatula, and placed in Tris–HCl buffer (1.5 M, 2 mL) at 2 °C for 2 h to extract $Au_{25}(SPG)_{18}$ from the gel. Then, the extract was filtered (0.2 μm pore size) followed by centrifugal ultrafiltration (MWCO = 30 kDa) to remove remaining gel lumps. The filtrate was concentrated by centrifugal ultrafiltration (MWCO

= 5 kDa) and lyophilized. The dried sample was dissolved in 2 % (v/v) acetic acid (200 μL) and reprecipitated in EtOH by centrifugation (10000 rpm). The obtained precipitate were washed with EtOH repeatedly and dried in vacuo. A typical yield of $Au_{25}(SPG)_{18}$ was ~1 mg (~1% based on Au).

2.2.3.4. Au:SPA clusters

PASH (2.5 mmol) was added to the iPrOH solution of $HAuCl_4 \cdot 4H_2O$ (5 mM, 50 mL). The mixed solution was stirred for 4 h at room temperature. The colorless solution was then cooled to ~0 °C in an ice bath for 30 min. To this solution, an ice-cooled aqueous solution of $NaBH_4$ (0.2 M, 12.5 mL) was dropwise added for ~10 min. After the stirring for 1 h, the sticky black precipitate that formed was dissolved in a Tris–HCl buffer solution (1.5 M, 2 mL), collected, and precipitated using excess EtOH. After being washed with EtOH three times, the black precipitate was dried in vacuo and used for further experiments.

Crude Au:SPA clusters were fractionated by PAGE in the same way described in 2.2.3.3. They were separated into six fractions.

2.2.3.5. $[Au_{25}(SEtPh)_{18}]^-$ and $[Au_{23}(ScHex)_{16}]^-$

Reference clusters of $[Au_{25}(SEtPh)_{18}]^-$ and $[Au_{23}(ScHex)_{16}]^-$ were synthesized by the reported procedures.[38,39]

2.2.4. X-ray absorption fine structure

X-ray absorption fine structures (XAFS) of $Au_{25}(SPG)_{18}$, $[Au_{25}(SEtPh)_{18}]^-$, and $[Au_{23}(ScHex)_{16}]^-$ at the Au L_3-edge were measured in BL01B1 beamline at the SPring-8

facility of the Japan Synchrotron Radiation Research Institute (JASRI). The incident X-ray beam was monochromatized by an Si(111) double-crystal monochromator. The energy of X-ray was calibrated using Au foil. Solid samples were ground in an agate mortar with boron nitride powder and pressed into square pellets (5 × 10 mm). Due to the hygroscopicity of $Au_{25}(SPG)_{18}$, it was firstly dissolved in 50 % water/1.5 M Tris−HCl buffer (v/v) and dried up by a lyophilizer with boron nitride before grinding. The sample pellets were wrapped with aluminum foil and mounted on a copper holder attached to a cryostat.[40] Data analysis was performed using the program REX2000 ver 2.5.9 program (Rigaku Co.). At first, extended X-ray absorption fine structure (EXAFS) oscillations were extracted from the raw spectra by subtracting the atomic absorption background using a cubic spline interpolation and were normalized to the edge height. The k^3-weighted χ spectra in the range of 3.0 $Å^{-1} \leq k \leq 21.0$ $Å^{-1}$ were Fourier-transformed into r space. The curve-fitting analysis on Fourier transformed (FT)-EXAFS was performed for one Au–S and two Au–Au bonds in the range of 1.5 Å $\leq r \leq$ 3.0 Å. In the curve-fitting analysis, the phase shifts and back-scattering amplitude functions for Au–S and Au–Au bonds were extracted from the corresponding simulation results of the FEFF8 program[41] by setting the value of Debye-Waller (DW) factor to 0.0036. This value did not significantly affect the phase shifts and the back-scattering amplitude functions.

2.3. Calculation

Density functional theory (DFT) calculations were performed on singlet $[Au_{25}(SCH_3)_{18}]^-$ with using Gaussian 09 package.[42] Basis sets were LanL2DZ for Au atom with its effective core potential and 6-31G(d) for C, H, and S atoms. Structural optimization was carried out followed by frequency calculation to check whether the

optimized structure was a local minimum structure. Total energy of optimized structures is corrected with vibrational zero-point energy. Time dependent (TD)-DFT calculation was also conducted on the optimized structures. The number of states was 100.

EXAFS simulation was performed on the DFT-optimized structures of $[Au_{25}(SCH_3)_{18}]^-$ with using FEFF8 code[41] built in REX2000. Optimized $[Au_{25}(SCH_3)_{18}]^-$ was scaled by 98.5 % prior to the simulation. In the simulation, the value of DW factor of each Au atom was set according to the experimental result of curve fitting analysis on $Au_{25}(SPG)_{18}$.

2.4. Results and discussion

2.4.1. Isolation of $Au_{25}(SPG)_{18}$

$Au_{25}(SPG)_{18}$ was synthesized by the modified procedure of the previous report.[35] First of all, $HAuCl_4$ and PGSH were mixed and stirred in EtOH to make Au(I)-SPG complex. Thus formed complex was slowly reduced by dropping ice-cooled $NaBH_4$*aq* in an ice bath. The crude product of sticky precipitate was collected and washed with EtOH. The obtained crude Au:SPG clusters were fractionated by PAGE. Figure 2.4 shows a typical result of PAGE separation of Au:SPG clusters. They were clearly separated into six fractions (**Fr1–6**). Negative-mode ESI mass spectra of **Fr1–6** are shown in Figure 2.5. In all the fractions, a major series of peaks are assigned to the multiply charged anions of $Au_n(SPG)_m$ generated by the deprotonation of -COOH groups in SPG ligands. The progression in higher mass region can be assigned to the adducts of Na^+ and/or $Tris^+$ used in the buffer solution to $-COO^-$ groups instead of H^+. From the series of mass peaks, the composition of $Au_n(SPG)_m$ majorly contained in each fraction was obtained and is summarized in Table 2.1. $Au_{25}(SPG)_{18}$ was isolated as **Fr4** with green color.

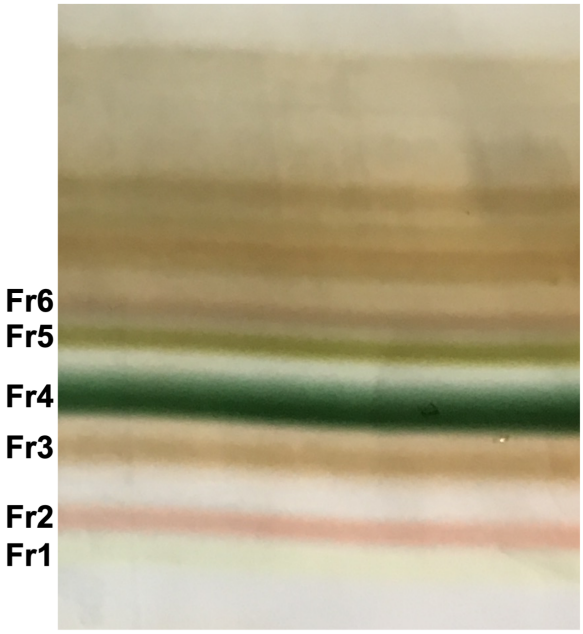

Figure 2.4. Typical PAGE pattern of the crude Au:SPG clusters.

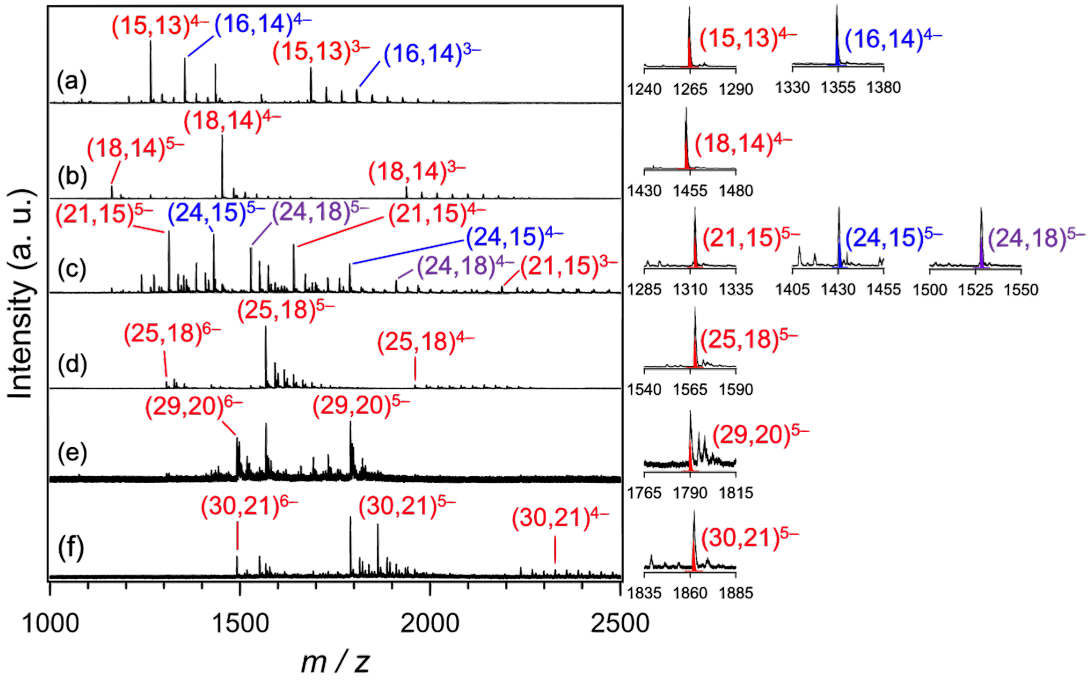

Figure 2.5. Negative-mode ESI mass spectra of (a) **Fr1**, (b) **Fr2**, (c) **Fr3**, (d) **Fr4**, (e) **Fr5**, and (f) **Fr6**. The major mass peaks can be assigned to the multiply charged anions of $Au_n(SPG)_m$ denoted as $(n,m)^{z-}$. z represents the total charge of $Au_n(SPG)_m$. In the right side, the simulated mass peaks of $(n,m)^{z-}$ are compared with experimental ones.

Table 2.1. Composition of $Au_n(SPG)_m$ contained in **Fr1**–**6**.

Fraction	Composition
Fr1	$Au_{15}(SPG)_{13}$, $Au_{16}(SPG)_{14}$
Fr2	$Au_{18}(SPG)_{14}$
Fr3	$Au_{21}(SPG)_{15}$, $Au_{24}(SPG)_{15}$, $Au_{24}(SPG)_{18}$
Fr4	$Au_{25}(SPG)_{18}$
Fr5	$Au_{29}(SPG)_{20}$
Fr6	$Au_{30}(SPG)_{21}$

For further characterization, I tried to improve the yield of $Au_{25}(SPG)_{18}$. Conventionally, due to the outstanding stability, $Au_{25}(SR)_{18}$ is selectively obtained when the solution of the crude Au:SR mixture is stirred at high temperature for long time.[43,44] With expecting to obtain $Au_{25}(SPG)_{18}$ selectively, crude Au:SPG clusters were annealed by stirring in an aqueous solution for 24 h. Figure 2.6 shows the result of PAGE separation of crude Au:SPG as prepared and annealed at r.t., 40 ºC, and 50 ºC. The green band of $Au_{25}(SPG)_{18}$ completely disappears after the annealing, indicating that $Au_{25}(SPG)_{18}$ was not thermally stable. Indeed, during the synthesis, the reaction solution was cooled in an ice bath and the Au:SPG clusters formed were precipitated out from the system soon after the reduction. Thermally unstable $Au_{25}(SPG)_{18}$ might be trapped in such formation process.

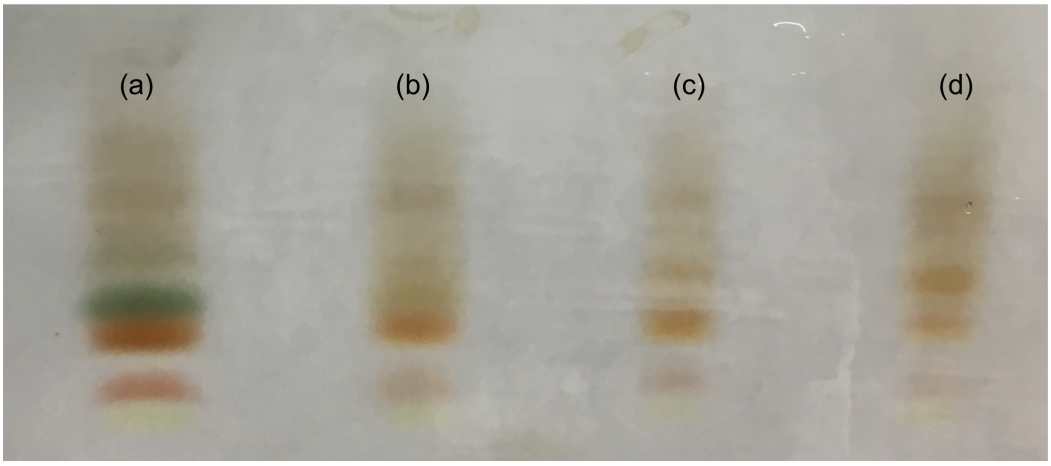

Figure 2.6. PAGE patterns of the crude Au:SPG clusters (a) as prepared and after being stirred in water for 24 h at (b) r.t., (c) 40 ºC, and (d) 50 ºC.

2.4.2. Characterization of $Au_{25}(SPG)_{18}$

2.4.2.1. Charge state of $Au_{25}(SPG)_{18}$

The charge state of $Au_{25}(SPG)_{18}$ was firstly checked. Conventional $Au_{25}(SR)_{18}$ cluster can take three charge states: anion, neutral, and cation.[39] Among three states, anion is the most stable state with a closed shell of $(1S)^2(1P)^6$.[45] Figure 2.7 shows ESI-mass spectrum of $Au_{25}(SPG)_{18}$ after the reprecipitation with using 2 % acetic acid solution. By this treatment, the adducts of $Tris^+$ and/or Na^+ were decreased and the peak intensity was enhanced. The inset of Figure 2.7 compares the most intense peak at m/z = 1568 and the isotope pattern simulations for $Au_{25}(SPG)_{18}$. When $Au_{25}(SPG)_{18}$ is neutral, the number of deprotonation is same as the total charge. However, the number of deprotonation is decreased by one in the case of anion and increased by one in the case of cation. As a result, m/z value of $Au_{25}(SPG)_{18}$ is shifted dependent on its inherent charge. In the inset of Figure 2.7, the simulated isotope pattern for the anion of $Au_{25}(SPG)_{18}$ most reproduces the experimental result than those for neutral and cation. Therefore, it is concluded that

$Au_{25}(SPG)_{18}$ was isolated as anion with formally 8 electrons as in the case of conventional $Au_{25}(SR)_{18}$ cluster.

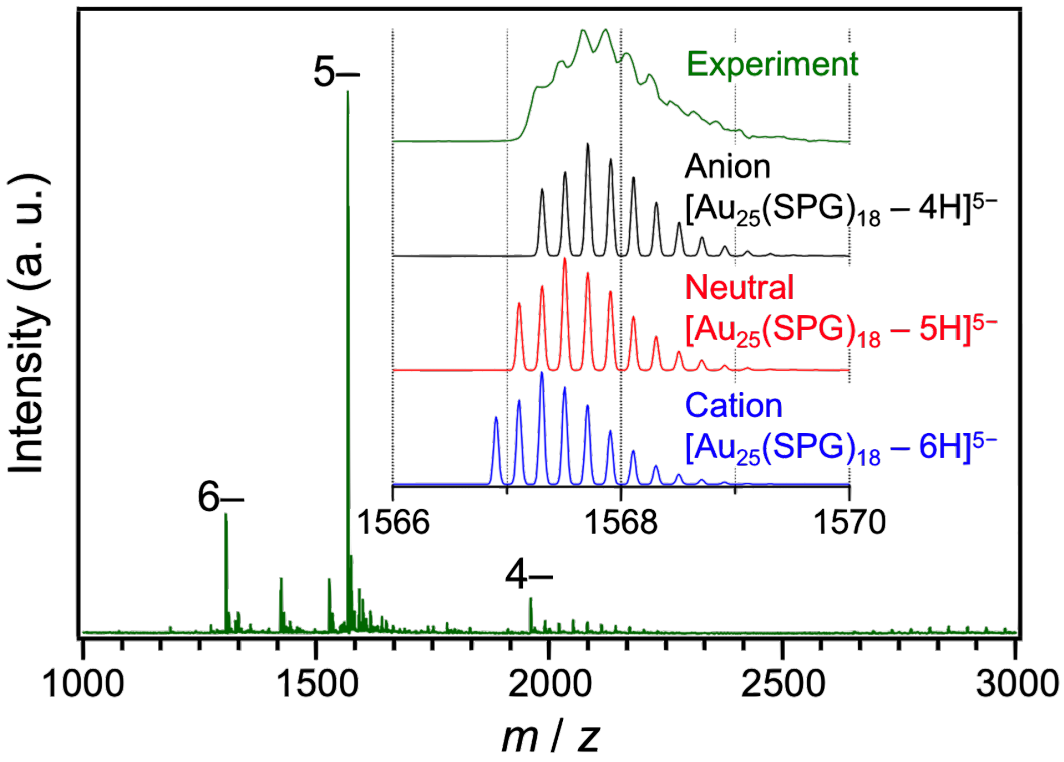

Figure 2.7. Negative-mode ESI mass spectrum of $Au_{25}(SPG)_{18}$ after the reprecipitation with using 2 % acetic acid solution. The number on the peaks represents the total charge of $Au_{25}(SPG)_{18}$. The inset shows an expanded mass peak at m/z = 1568 and simulated mass peaks for each charge state of $Au_{25}(SPG)_{18}$.

2.4.2.2. Structure of $Au_{25}(SPG)_{18}$

Figure 2.8a shows the UV-vis absorption spectrum of $[Au_{25}(SPG)_{18}]^-$. It has a distinct peak at 2.1 eV and looks different from the previously reported one (Figure 2.3b).[35] This is probably due to the contaminants in PGSH; the purity of PGSH in the previous study is 87 %,[35] smaller than that of present study (97 %). The profile of the UV-vis absorption spectrum of $[Au_{25}(SPG)_{18}]^-$ is significantly different from that of conventional $[Au_{25}(SEtPh)_{18}]^-$ with an Ih Au_{13} core even though the same composition each other

(Figures 2.8a and b). Instead, the spectral profile of $[Au_{23}(ScHex)_{16}]^-$ with a non-Ih and anisotropic Au_{13} core is quite similar to that of $[Au_{25}(SPG)_{18}]^-$ (Figures 2.8a and c).[38] This result indicates that the core structure of $[Au_{25}(SPG)_{18}]^-$ is not an Ih structure, but takes an anisotropic structure like that of $[Au_{23}(ScHex)_{16}]^-$. The optical HOMO-LUMO gaps (HL^{opt}) of $[Au_{25}(SPG)_{18}]^-$, $[Au_{25}(SEtPh)_{18}]^-$, and $[Au_{23}(ScHex)_{16}]^-$ are obtained by the extrapolation of first absorption peaks (Figure 2.8). The value for $[Au_{25}(SPG)_{18}]^-$ is 1.8 eV, similar to that of $[Au_{23}(ScHex)_{16}]^-$ (1.9 eV) but different from that of $[Au_{25}(SEtPh)_{18}]^-$ (1.3 eV).

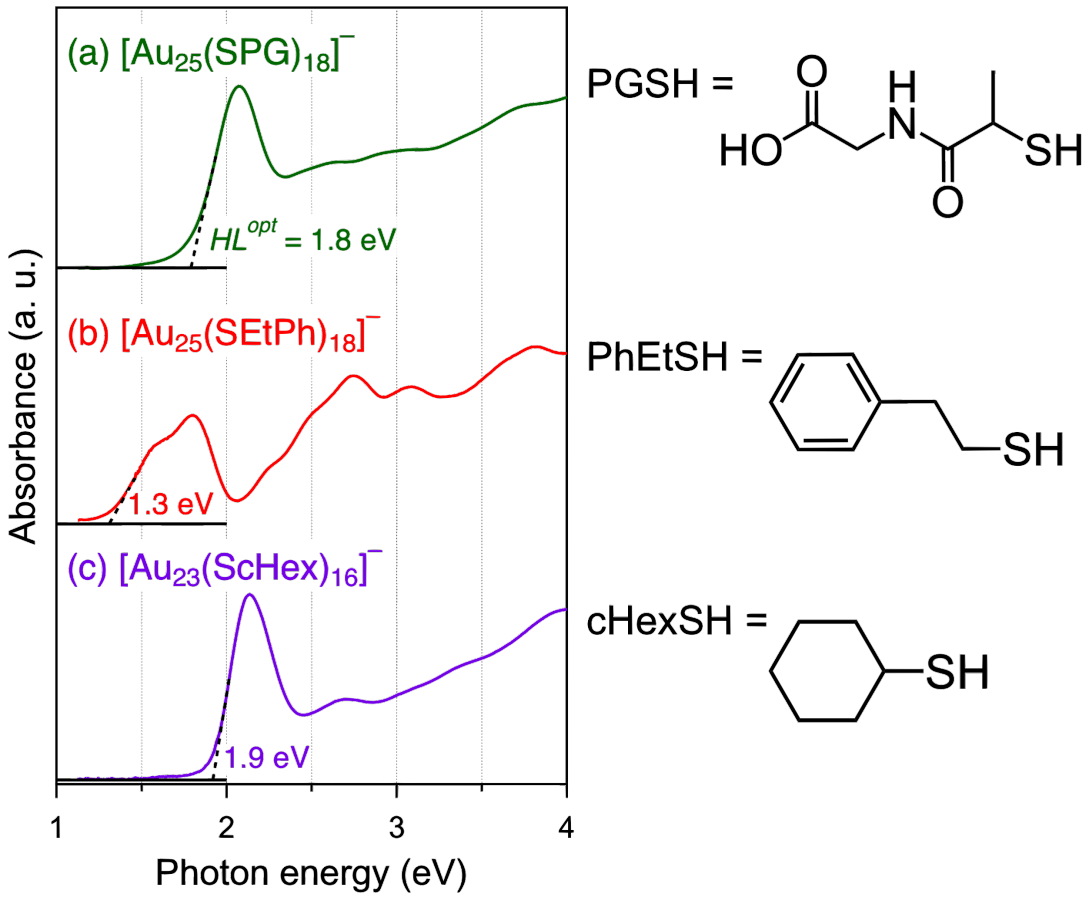

Figure 2.8. UV-vis absorption spectra of (a) $[Au_{25}(SPG)_{18}]^-$, (b) $[Au_{25}(SEtPh)_{18}]^-$, and (c) $[Au_{23}(ScHex)_{16}]^-$. The spectra are offset for clarity. The optical HOMO-LUMO gap (HL^{opt}) of each cluster is indicated in the spectra. The structures of PGSH, PhEtSH, and cHexSH are also shown.

To gain an insight into the geometrical structure, I measured Au-L_3 edge EXAFS of $[Au_{25}(SPG)_{18}]^-$, $[Au_{25}(SEtPh)_{18}]^-$, and $[Au_{23}(ScHex)_{16}]^-$ because I could not obtain the single crystal of $[Au_{25}(SPG)_{18}]^-$. It is known that EXAFS oscillations in the region of $k \geq 10$ Å^{-1} sensitively reflect the geometrical structure of Au core.[40] Figures 2.9a–c show EXAFS oscillations of $[Au_{25}(SPG)_{18}]^-$, $[Au_{25}(SEtPh)_{18}]^-$, and $[Au_{23}(ScHex)_{16}]^-$ measured at 10 K. Low-temperature measurement is essential to suppress the thermal fluctuation of tiny Au clusters and to get their structural information.[40] As in the case of UV-vis absorption spectra, oscillation pattern of $[Au_{25}(SPG)_{18}]^-$ is different from that of $[Au_{25}(SEtPh)_{18}]^-$, but similar to that of $[Au_{23}(ScHex)_{16}]^-$ (Figures 2.9a–c). From these results, I concluded that $[Au_{25}(SPG)_{18}]^-$ has a non-Ih Au_{13} core and thus is a so-called structural isomer of $[Au_{25}(SR)_{18}]^-$. Many $[Au_{25}(SR)_{18}]^-$ clusters protected by various

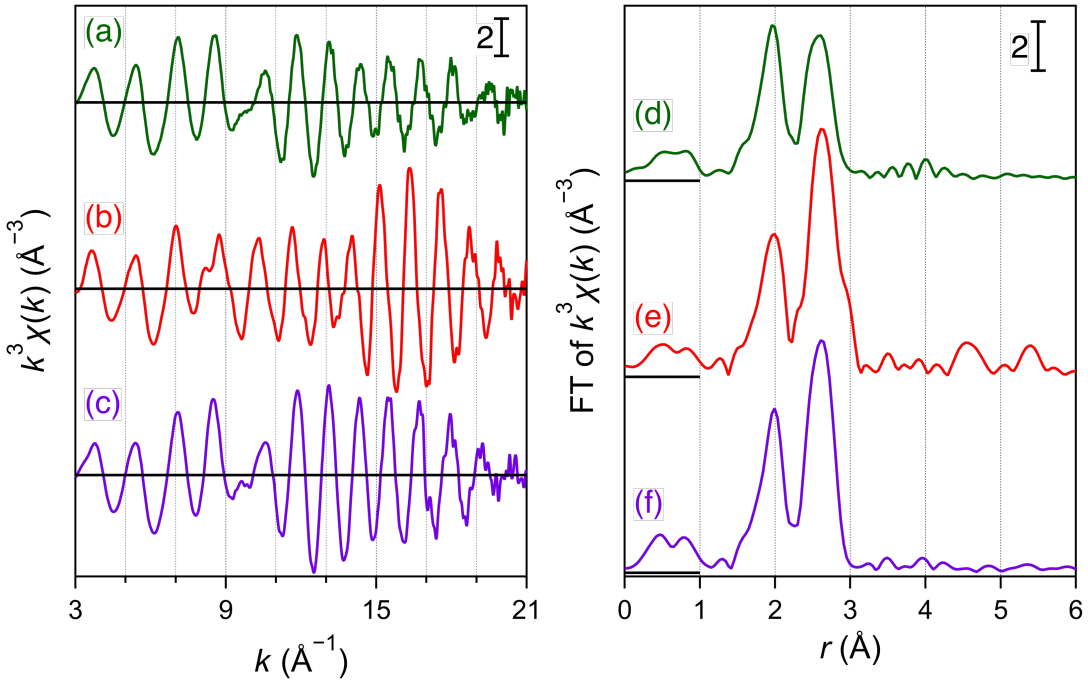

Figure 2.9. (Left) Au-L_3 edge EXAFS oscillations of (a) $[Au_{25}(SPG)_{18}]^-$, (b) $[Au_{25}(SEtPh)_{18}]^-$, and (c) $[Au_{23}(ScHex)_{16}]^-$ measured at 10 K. (Right) Au-L_3 edge FT-EXAFS spectra of (d) $[Au_{25}(SPG)_{18}]^-$, (e) $[Au_{25}(SEtPh)_{18}]^-$, and (f) $[Au_{23}(ScHex)_{16}]^-$. The spectra are offset for clarity.

thiolate ligands have been hitherto reported,[34] but this is the first example of $[Au_{25}(SR)_{18}]^-$ without an Ih core structure.

Figures 2.9d–f show FT-EXAFS spectra of $[Au_{25}(SPG)_{18}]^-$, $[Au_{25}(SEtPh)_{18}]^-$, and $[Au_{23}(ScHex)_{16}]^-$. The results of curve fitting analysis on FT-EXAFS spectra are summarized in Table 2.2. Structural data of $[Au_{25}(SEtPh)_{18}]^-$ and $[Au_{23}(ScHex)_{16}]^-$ obtained from the previous single crystal X-ray diffraction (XRD) analysis are summarized in Table 2.3. The Au–Au bonds in $[Au_{25}(SEtPh)_{18}]^-$ and $[Au_{23}(ScHex)_{16}]^-$ are classified into three groups according to their length:[40] Au–Au(S), Au–Au(M), and Au–Au(L) (Table 2.3). The average length of Au–Au(S) bonds is shorter than that of bulk Au (2.88 Å) while those of Au–Au(M) and Au–Au(L) bonds are longer. In the curve fitting analysis of $[Au_{25}(SPG)_{18}]^-$, $[Au_{25}(SEtPh)_{18}]^-$, and $[Au_{23}(ScHex)_{16}]^-$, Au–S, Au–Au(S), and Au–Au(M) bonds were taken into account because it is known that the contribution of Au–Au(L) bonds is quite small due to their large DW factor.[40] The

Table 2.2. Structural parameters of $[Au_{25}(SPG)_{18}]^-$, $[Au_{25}(SEtPh)_{18}]^-$, and $[Au_{23}(ScHex)_{16}]^-$ obtained by curve-fitting analysis of Au-L_3 edge FT-EXAFS.

Cluster	Bonds	C.N.	r (Å)	σ^2 (Å^2)	R (%)
$[Au_{25}(SPG)_{18}]^-$	Au–S	1.5(2)	2.313(3)	0.0038(12)	9.9
	Au–Au(S)	1.1(3)	2.689(4)	0.0036(15)	
	Au–Au(M)	1.1(7)	2.930(11)	0.0060(58)	
$[Au_{25}(SEtPh)_{18}]^-$ (ref. 40)	Au–S	1.6(2)	2.319(4)	0.0037(18)	10.6
	Au–Au(S)	1.5(4)	2.770(3)	0.0027(11)	
	Au–Au(M)	1.5(6)	2.936(6)	0.0040(24)	
$[Au_{23}(ScHex)_{16}]^-$	Au–S	1.6(2)	2.325(4)	0.0038(15)	8.8
	Au–Au(S)	1.3(5)	2.699(6)	0.0034(21)	
	Au–Au(M)	1.2(7)	2.926(10)	0.0041(40)	

C.N.: Coordination number, r (Å): bond length,
σ^2 (Å^2): Debye-Waller factor, R (%) = $(\sum(k^3\chi_{data} - k^3\chi_{fit})^2 / \sum(k^3\chi_{data})^2)^{1/2}$.

Table 2.3. Structural parameters of $[Au_{25}(SEtPh)_{18}]^-$ and $[Au_{23}(ScHex)_{16}]^-$ obtained by the single crystal XRD data.[32,38]

Cluster	Bonds	C.N.	*r* (Å)
$[Au_{25}(SEtPh)_{18}]^-$ (ref. 32)	Au–S	1.4	2.33
	Au–Au(S)	1.4	2.78
	Au–Au(M)	1.9	2.95
	Au–Au(L)	2.9	3.16
$[Au_{23}(ScHex)_{16}]^-$ (ref. 38)	Au–S	1.4	2.32
	Au–Au(S)	1.6	2.71
	Au–Au(M)	1.4	2.94
	Au–Au(L)	2.6	3.27

C.N.: Coordination number, *r* (Å): bond length.

coordination number and the bond length of $[Au_{25}(SEtPh)_{18}]^-$ and $[Au_{23}(ScHex)_{16}]^-$ obtained by curve fitting analysis are consistent with the reported single crystal XRD data (Tables 2.2 and 2.3).[32,38,40] As seen in figure 2.9, the result of curve firring analysis on $[Au_{25}(SPG)_{18}]^-$ was more similar to that on $[Au_{23}(ScHex)_{16}]^-$ than that on $[Au_{25}(SEtPh)_{18}]^-$ (Table 2.2). Especially, the lengths of Au–Au(S) bonds in $[Au_{25}(SPG)_{18}]^-$ and $[Au_{23}(ScHex)_{16}]^-$ (~2.7 Å) are shorter than that of $[Au_{25}(SEtPh)_{18}]^-$ (2.77 Å). This difference probably contributed to the difference of EXAFS oscillations in Figure 2.9.

PGSH has an asymmetric carbon next to S atoms (Figures 2.3 and 2.8). Although PGSH purchased this time was racemic, the distribution of *R*- and *S*-PGS ligands in $[Au_{25}(SPG)_{18}]^-$ might be different from the statistical distribution due to the chiral self-sorting on its surface.[46] Their distribution would be obtained by high performance liquid chromatography (HPLC) using a chiral column.[47] From such information, it is expected to gain an insight into the surface structure of $[Au_{25}(SPG)_{18}]^-$.

2.4.3. Model structure of $Au_{25}(SPG)_{18}$

2.4.3.1. Structural optimization of model structures

Next, I consider the possible model structures of $[Au_{25}(SPG)_{18}]^-$ based on the crystal structure of $[Au_{23}(ScHex)_{16}]^-$.[38] Figure 2.10 shows the crystal structure of $[Au_{23}(ScHex)_{16}]^-$. $[Au_{23}(ScHex)_{16}]^-$ has an anisotropic Au_{13} core symmetrically protected by the pairs of $Au_1(ScHex)_2$ and $Au_3(ScHex)_4$ oligomers and is formulated as $Au_{13}[Au_1(ScHex)_2]_4[Au_3(ScHex)_4]_2$ (Figure 2.10b). This anisotropic Au_{13} core can be viewed as an elongated-square-bipyramidal shape Au_{11} capped by two Au atoms. Two

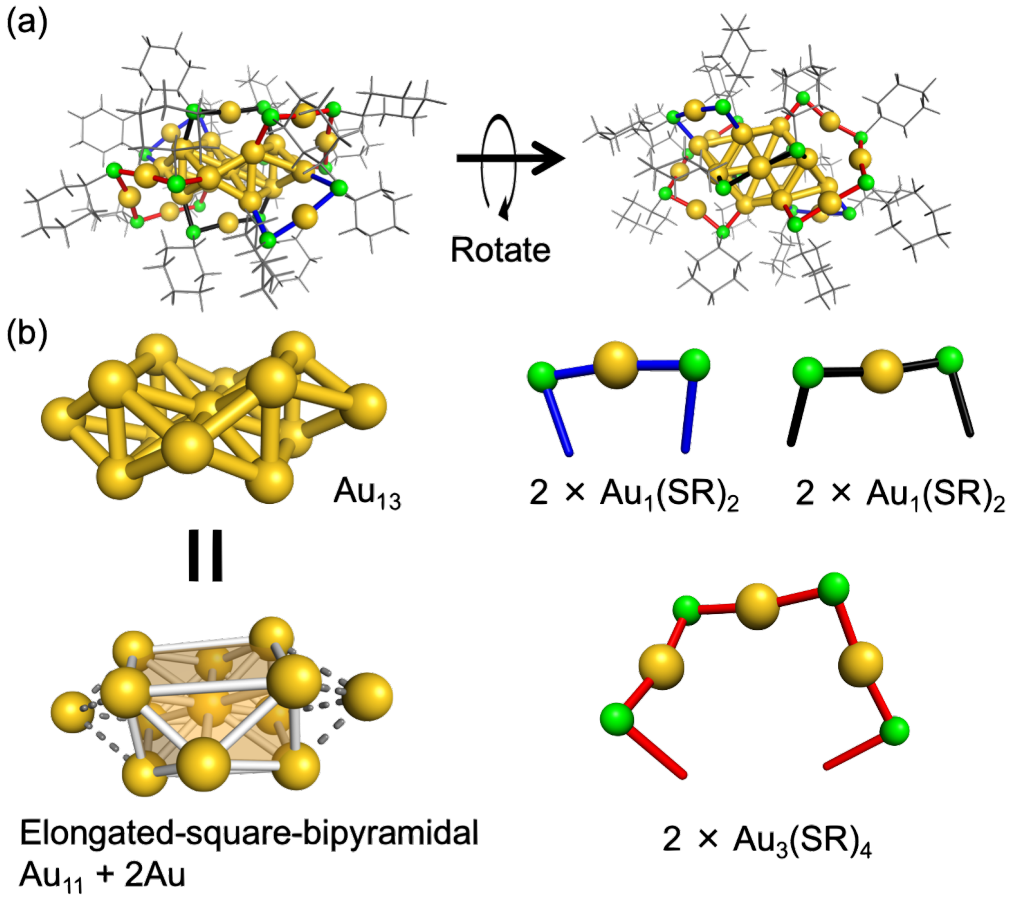

Figure 2.10. (a) Total and (b) decomposed structures of $[Au_{23}(ScHex)_{16}]^-$ determined by single crystal XRD.[38] cHex ring is depicted as gray stick. The black, blue, and red bonds represent the oligomer motifs of $Au_1(ScHex)_2$, $Au_1(ScHex)_2$, and $Au_3(ScHex)_4$, respectively. $Au_1(ScHex)_2$ oligomers are distinguished by the ligation sites. Color code: yellow (Au); green (S).

pairs of $Au_1(ScHex)_2$ oligomers occupy different sites of an anisotropic Au_{13} core (Figure 2.10b). To construct the model structures of $[Au_{25}(SPG)_{18}]^-$, I fixed the anisotropic Au_{13} core of $[Au_{23}(ScHex)_{16}]^-$ and elongated exterior oligomers because the results of optical absorption and EXAFS suggested that the core structures of $[Au_{23}(ScHex)_{16}]^-$ and $[Au_{25}(SPG)_{18}]^-$ are similar (Figures 2.8 and 2.9). The building scheme of the model structures is shown in Figure 2.11. The pairs of $Au_1(ScHex)_2$ and $Au_3(ScHex)_4$ oligomers are symmetrically elongated by adding two units of $Au_1(SR)_1$ and three models (models **1**–**3**) are constructed. In models **1** and **2**, the pair of $Au_1(SR)_2$ oligomers is elongated to $Au_2(SR)_3$ leading a formulation of $Au_{13}[Au_1(SR)_2]_2[Au_2(SR)_3]_2[Au_3(SR)_4]_2$ (Figures

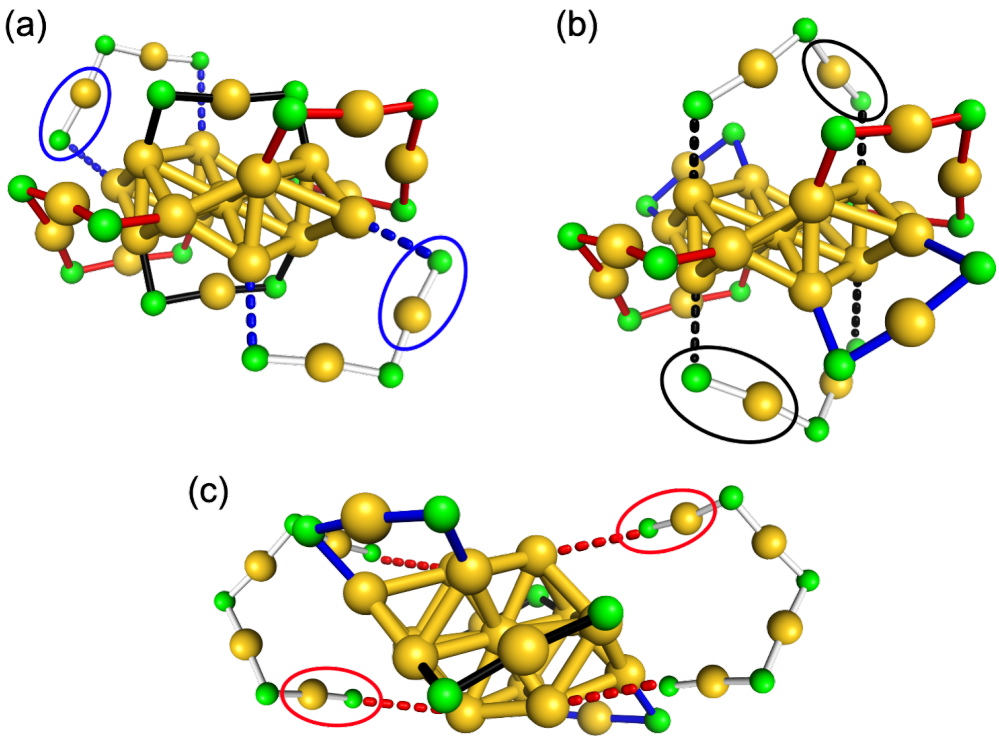

Figure 2.11. Building schemes of models (a) **1**, (b) **2**, and (c) **3** from the Au–S framework of $[Au_{23}(ScHex)_{16}]^-$.[38] The black, blue, and red bonds represent the oligomer motifs of $Au_1(ScHex)_2$, $Au_1(ScHex)_2$, and $Au_3(ScHex)_4$, respectively. $Au_1(ScHex)_2$ oligomers are distinguished by the ligation site. $Au_1(SR)_1$ units added are highlighted by circles. Color code: yellow (Au); green (S).

2.11a and b). In model **3**, the pair of $Au_3(SR)_4$ oligomers is elongated to $Au_4(SR)_5$ leading a formulation of $Au_{13}[Au_1(SR)_2]_4[Au_4(SR)_5]_2$ (Figure 2.11c).

Thus constructed models are evaluated by theoretical calculation. Firstly, structural optimization of $[Au_{25}(SR)_{18}]^-$ (R = CH_3 to reduce the calculation cost) with models **1**–**3** was conducted by DFT. The optimized structures of $[Au_{25}(SCH_3)_{18}]^-$ (cluster **A**) for models **1**–**3** (clusters **A1**–**A3**) are shown in Figure 2.12. All the models are successfully

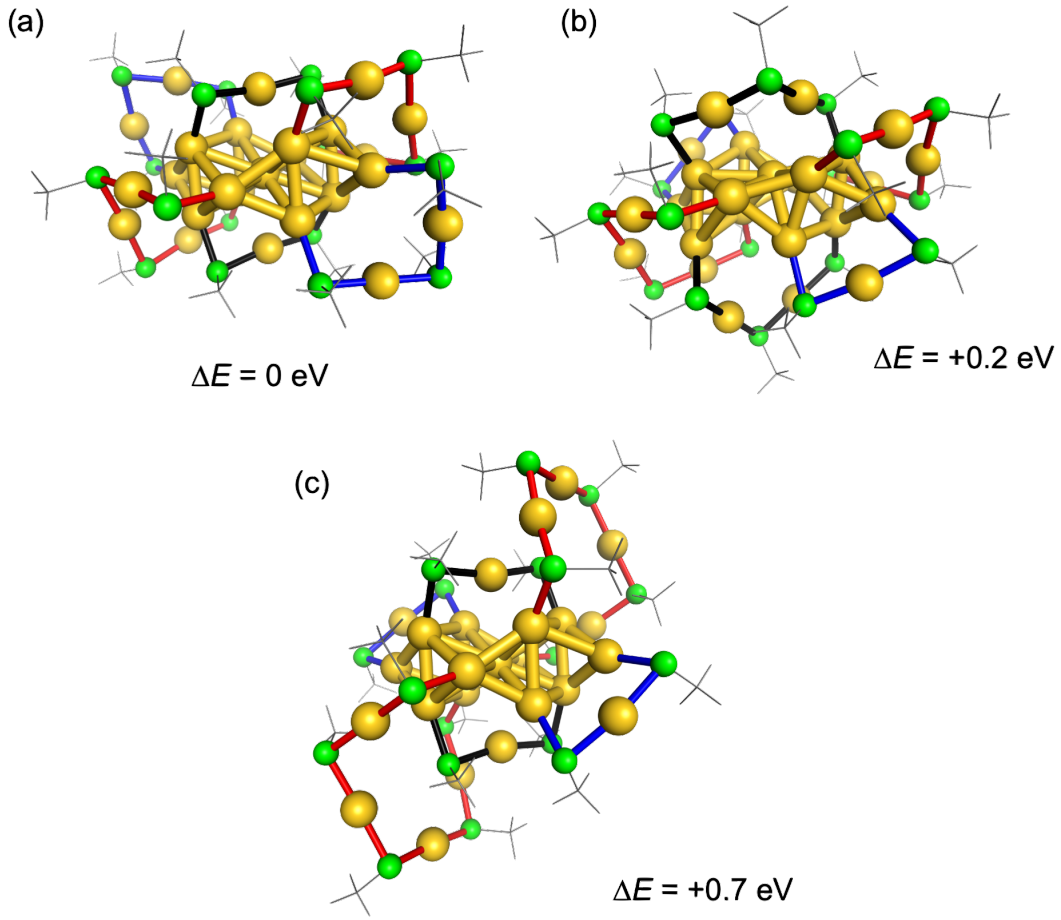

Figure 2.12. DFT-optimized structures of $[Au_{25}(SCH_3)_{18}]^-$ with (a) model **1**, (b) model **2**, and (c) model **3** (clusters **A1**, **A2**, and **A3**, respectively). The relative energy of **A2** and **A3** against model **A1** (ΔE) is also shown. The black, blue, and red bonds represent the oligomer motifs of $Au_1(SCH_3)_2$, $Au_1(SCH_3)_2$, and $Au_3(SCH_3)_4$, respectively. $Au_1(SCH_3)_2$ oligomers are distinguished by the ligation sites. Color code: yellow (Au); green (S). CH_3 group is depicted as gray stick.

optimized with keeping their initial structural motifs shown in Figure 2.11. The total energies of **A1**–**A3** were also obtained with zero-point energy correction. The energies of **A1** and **A2** were comparable, whereas **A3** was less stable. The relative energies against **A1** (ΔE) of **A2** and **A3** are 0.2 and 0.7 eV, respectively (Figure 2.12). Upon **A1**–**A3**, TD-DFT calculations and EXAFS simulations were conducted. Figures 2.13a–d compare the experimental UV-vis absorption spectrum of $[Au_{25}(SPG)_{18}]^-$ and the simulated spectra of **A1**, **A2**, and **A3**. The spectral profiles of **A1** and **A2** reproduce the experimental one rather than that of **A3** especially for the characteristic peak at ~2 eV. Figures 2.13e–g show the experimental FT-EXAFS spectrum of $[Au_{25}(SPG)_{18}]^-$ and the simulated spectra of **A1**,

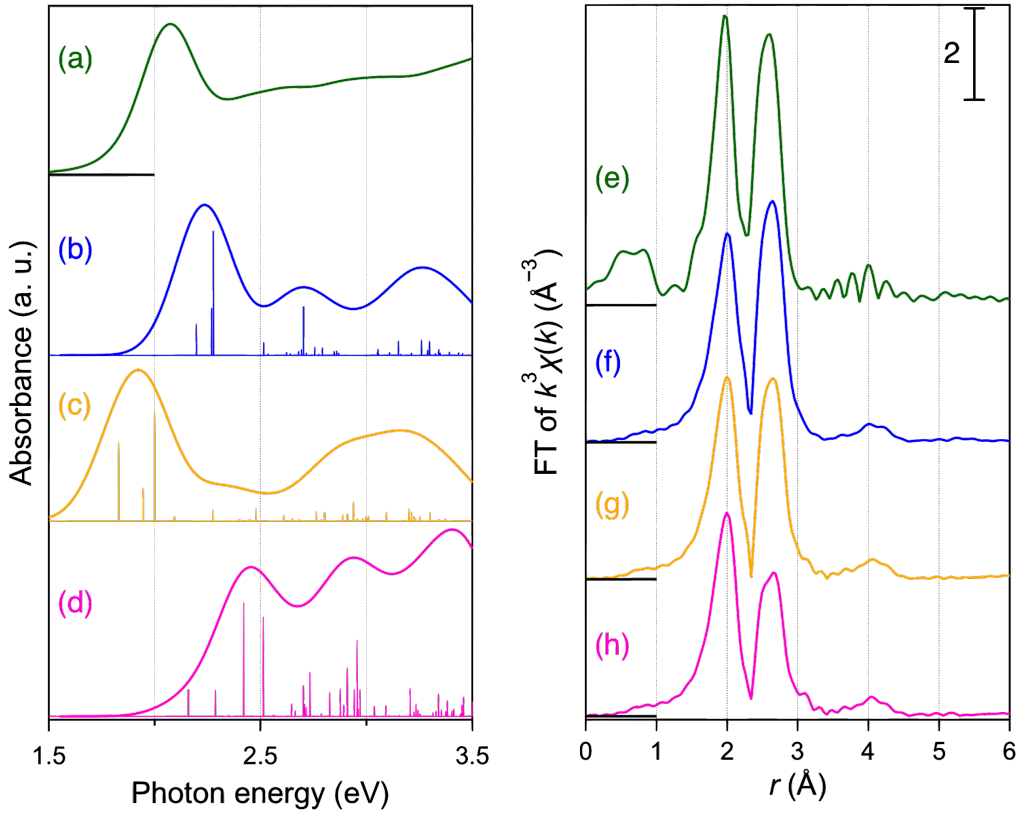

Figure 2.13. UV-vis absorption spectrum of (a) $[Au_{25}(SPG)_{18}]^-$ and those simulated for (b) **A1**, (c) **A2**, and (d) **A3**. The spectra are offset for clarity. In the spectra of (b)–(d), calculated absorption peaks are broadened by Gaussian with HWHM = 0.15 eV. FT-EXAFS spectrum of (e) $[Au_{25}(SPG)_{18}]^-$ and those simulated for (f) **A1**, (g) **A2**, and (h) **A3**. The spectra are offset for clarity.

A2, and **A3**. As in the result of TD-DFT calculation, the simulated spectra of **A1** and **A2** are more similar to the experimental spectrum of $[Au_{25}(SPG)_{18}]^-$ than that of **A3**. From these calculation results, as the model structures of $[Au_{25}(SPG)_{18}]^-$, the models **1** and **2** formulated as $Au_{13}[Au_1(SR)_2]_2[Au_2(SR)_3]_2[Au_3(SR)_4]_2$ were more plausible than model **3** formulated as $Au_{13}[Au_1(SR)_2]_4[Au_4(SR)_5]_2$ as long as $[Au_{25}(SPG)_{18}]^-$ contained only single species.

2.4.3.2. Electronic structure of model structures

Next, I compared electronic structures of **A1** and **A2** with conventional $[Au_{25}(SR)_{18}]^-$. Cluster **A** having the same structural motif as $[Au_{25}(SEtPh)_{18}]^-$, an Ih Au_{13} core protected by six oligomers of $Au_2(SCH_3)_3$, was also optimized under the same calculation set up (cluster **A4**). Figure 2.14 shows the occupied superatomic orbitals of **A1**, **A2**, and **A4**. As explained above, superatomic electron configuration of **A4** was $(1S)^2(1P)^6$ and consistent with the spherical jellium model (Figure 2.14a).[33] On the other hand, the electronic structures of **A1** and **A2** were different from that of **A4** due to the splitting and reordering of superatomic orbitals in their anisotropic core structure. Their superatomic electron configuration was $(1S)^2(1P)^4(1D)^2$ (Figures 2.14b and c) as in the previous calculation result of $[Au_{23}(SR)_{16}]^-$.[21]

The energy levels of superatomic orbitals were also compared. Figure 2.15 shows energy levels near the frontier orbitals in **A1**, **A2**, and **A4**. The HOMOs and LUMOs of **A4** are degenerated superatomic 1P and 1D orbitals, respectively. Its calculated HOMO-LUMO gap (HL^{cal}) is 1.81 eV (Figure 2.15a). In the cases of **A1** and **A2**, some of the split 1D and 1F orbitals are stabilized by the anisotropic deformation of Au_{13} core and become the HOMOs and LUMOs. Alternatively, one of the 1P orbitals is destabilized to the

LUMO + 1 in **A1** and **A2**. The HOMO is one of the split 1D orbitals in both **A1** and **A2**. The LUMOs of **A1** are the split 1D and 1F orbitals and the LUMO of **A2** is the split 1F orbital (Figures 2.15b and c). The HL^{cal} values of **A1** and **A2** are 2.32 and 2.01 eV, respectively, larger than HL^{cal} = 1.81 eV of **A4** (Figure 2.15). These calculation results were consistent with the results of UV-vis absorption spectroscopy; HL^{opt} of $[Au_{25}(SPG)_{18}]^-$ (1.8 eV) was larger than that of $[Au_{25}(SEtPh)_{18}]^-$ (1.3 eV) . Therefore, it is concluded that the significant difference of the optical absorption of $[Au_{25}(SPG)_{18}]^-$ from $[Au_{25}(SEtPh)_{18}]^-$ is due to the reordering of superatomic orbitals by the anisotropic deformation of Au_{13} core.

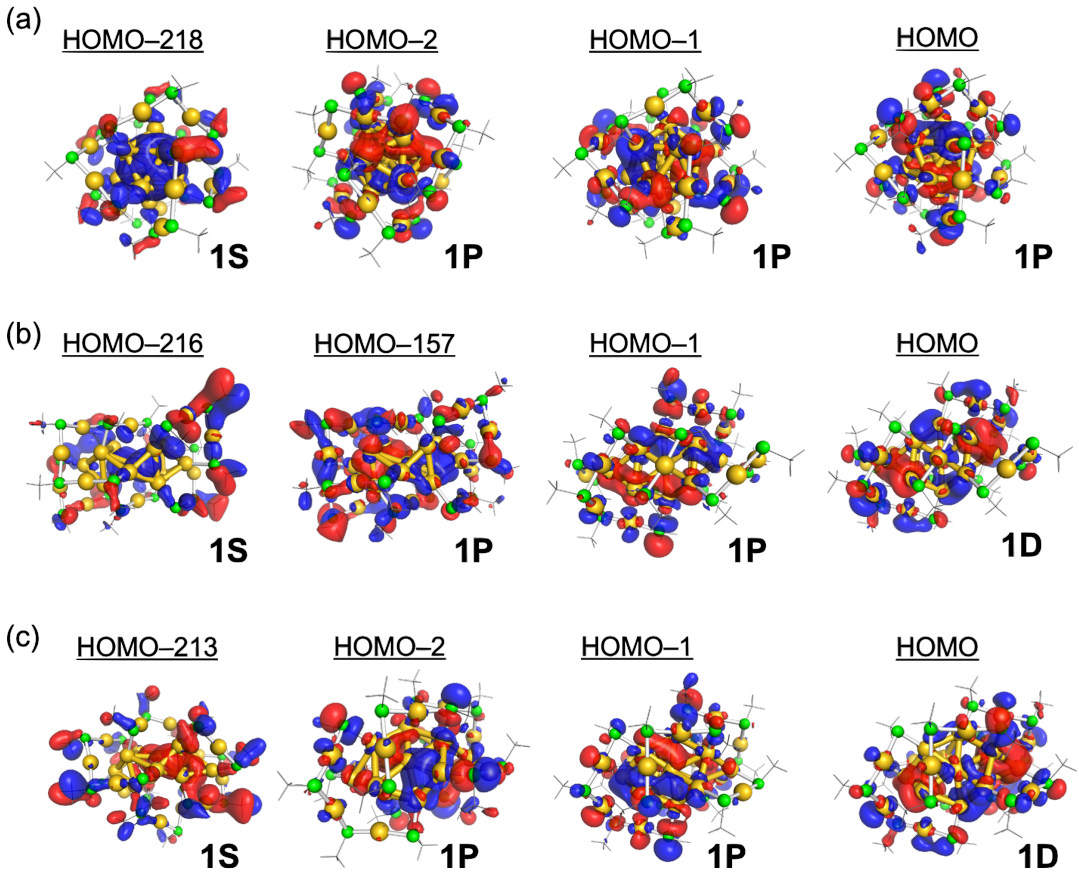

Figure 2.14. Kohn-Sham orbitals corresponding to the occupied superatomic orbitals in (a) **A4**, (b) **A1**, and (c) **A2**. Isovalue of each orbital surface is 0.015.

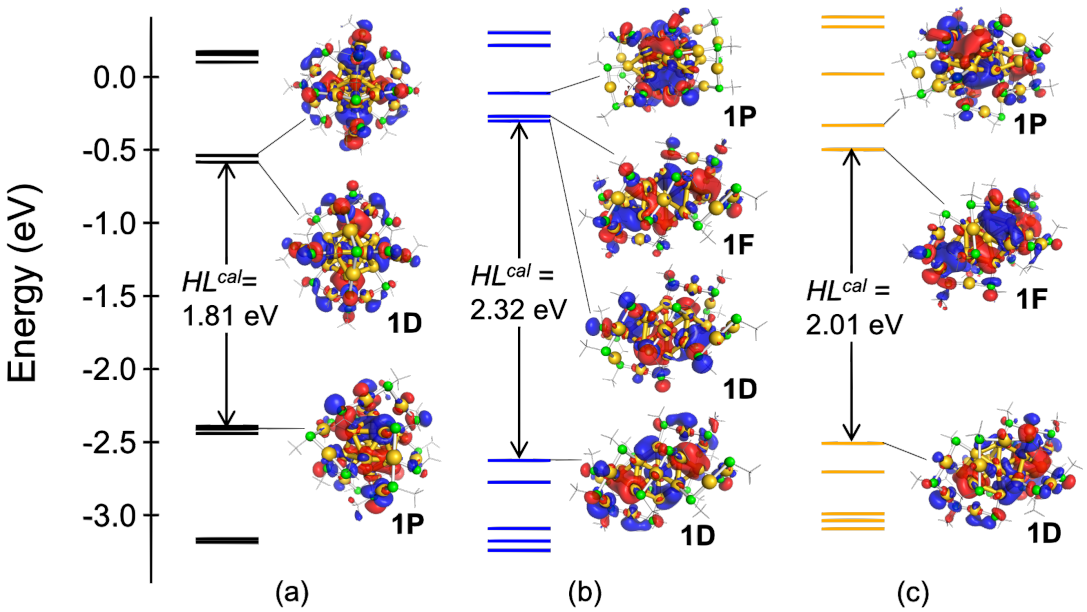

Figure 2.15. Kohn-Sham energy diagrams around the frontier orbitals of (a) **A4**, (b) **A1**, and (c) **A2**. The HOMO, LUMO, and LUMO + 1 and the calculated HOMO-LUMO gaps (HL^{cal}) are also shown.

2.4.4. Origin of an anisotropic core in $Au_{25}(SPG)_{18}$

Why an anisotropic Au_{13} core was formed in $[Au_{25}(SPG)_{18}]^{-}$? From the numerous crystallographic study on $Au_n(SR)_m$ to date, it is widely accepted that a non-Ih and an anisotropic Au core is preferentially formed with using bulky thiols having a secondary or tertiary α-carbon such as *t*BuSH and AdmSH.[48] Because PGSH also has a secondary α-carbon (Figures 2.3 and 2.8), it is natural to attribute the reason for the formation of a non-Ih Au_{13} core to the bulkiness of PGSH as empirically known. Then, I checked whether the presence of secondary α-carbon was enough for the formation of a non-Ih $[Au_{25}(SR)_{18}]^{-}$ or not. For this purpose, Au clusters were synthesized with using PASH (Scheme 2.1) which has a secondary α-carbon and is a substructure of PGSH. Crude Au:SPA clusters were prepared at first and fractionated by PAGE as in the case of Au:SPG clusters. Figure 2.16 shows a typical result of PAGE of crude Au:SPA clusters. They were

clearly separated into six fractions of **Fr1'–6'**, but the green fraction like $[Au_{25}(SPG)_{18}]^{-}$ was not observed. The absence of $Au_{25}(SPA)_{18}$ in **Fr1'–6'** was confirmed by mass spectrometry. In the ESI-mass spectra of **Fr1'–6'**, the mass peaks corresponding to $[Au_{25}(SPA)_{18}]^{z-}$ were not found (Figure 2.16, right). The difference between PGSH and PASH is the terminal glycine moiety (Scheme 2.1, Figures 2.3 and 2.8). Therefore, this

Scheme 2.1. Structure of PASH.

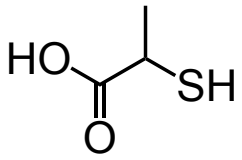

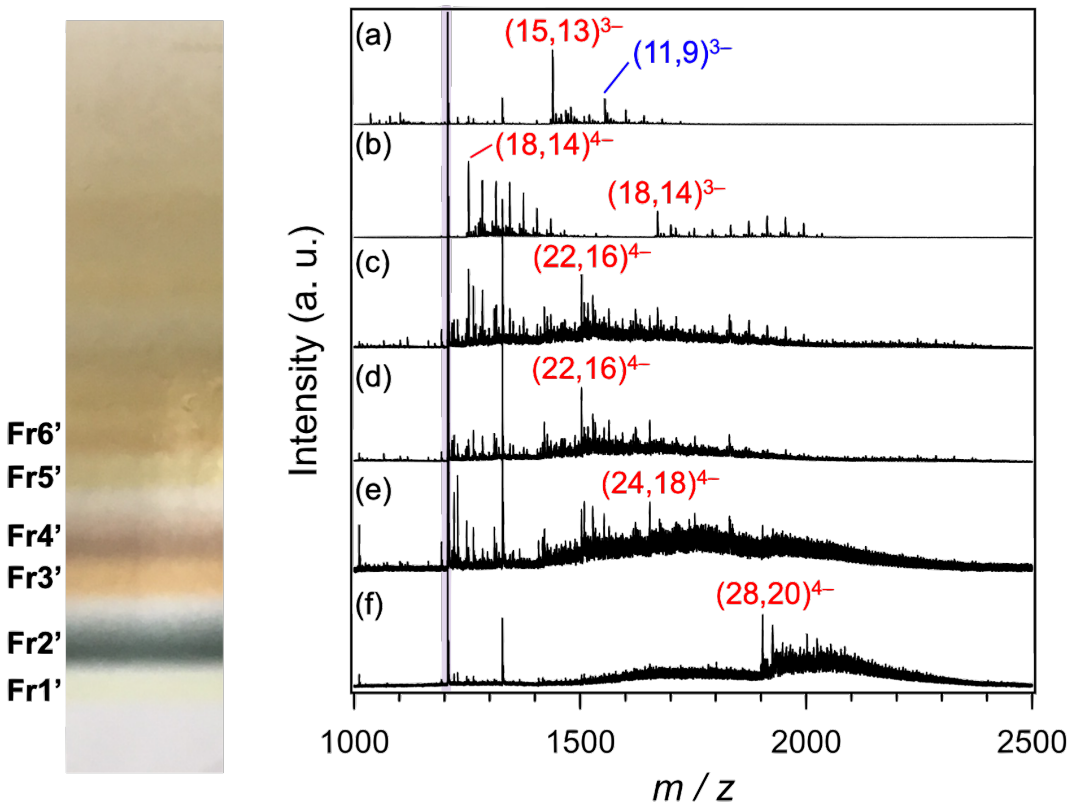

Figure 2.16. (Left) Typical PAGE pattern of crude Au:SPA clusters. (Right) Negative-mode ESI mass spectra of (a) **Fr1'**, (b) **Fr2'**, (c) **Fr3'**, (d) **Fr4'**, (e) **Fr5'**, and (f) **Fr6'**. The major mass peaks can be assigned to the multiply charged anions of $Au_n(SPA)_m$ denoted as $(n,m)^{z-}$. z represents the total charge of $Au_n(SPA)_m$. The prominent peak shaded purply (m/z = 1204) indicates the fragment species of $[Au_4(SPA)_4]^{-}$.

result is ascribed to that not only the bulkiness of a secondary α-carbon around the superatomic Au core, steric repulsion and/or hydrogen bonding involving -COOH (-COO^-) and -NH groups of glycine moiety are also important for the formation of an anisotropic $[Au_{25}(SR)_{18}]^-$. In addition, $[Au_{25}(SPG)_{18}]^-$ was relatively stable under the basic condition of $NaBH_4$ reduction and buffer solution for PAGE. Because the -COOH group of PGSH is deprotonated in such condition, the Coulomb repulsion between -COO^- groups and the solvation around -COO^- might contribute to the stabilization of the anisotropic structure of $[Au_{25}(SPG)_{18}]^-$.

2.5. Summary

In summary, $[Au_{25}(SPG)_{18}]^-$ was successfully synthesized and characterized. The profiles of UV-vis absorption spectrum and EXAFS oscillation of $[Au_{25}(SPG)_{18}]^-$ were different from those of conventional $[Au_{25}(SEtPh)_{18}]^-$ having an Ih Au_{13} core, but similar to those of $[Au_{23}(ScHex)_{16}]^-$ having a non-Ih and anisotropic Au_{13} core. The result indicated that $[Au_{25}(SPG)_{18}]^-$ is the first example of structural isomer of $[Au_{25}(SR)_{18}]^-$ with an anisotropic core. The optical HOMO-LUMO gap of $[Au_{25}(SPG)_{18}]^-$ (1.8 eV) was larger than that of $[Au_{25}(SEtPh)_{18}]^-$ (1.3 eV). According to the theoretical calculations based on the experimental results, the larger HOMO-LUMO gap of $[Au_{25}(SPG)_{18}]^-$ was ascribed to the reordering of superatomic orbitals to form an electron configuration of $(1S)^2(1P)^4(1D)^2$ due to the anisotropic core deformation. The formation of an anisotropic core in $[Au_{25}(SPG)_{18}]^-$ was probably induced by non-covalent interactions between PGS ligands. To gain an insight into the surface structure of $[Au_{25}(SPG)_{18}]^-$, the chirality distribution of PGS ligands should be checked in the future.

References

1. Zhou, M.; Higaki, T.; Li, Y.; Zeng, C.; Li, Q.; Sfeir, M. Y.; Jin, R. *J. Am. Chem. Soc.* **2019**, *141*, 19754.
2. Omoda, T.; Takano, S.; Tsukuda, T. *Small* **2020**, e2001439.
3. Kelly, K. L.; Coronado, E.; Zhao, L. L.; Schatz, G. C. *J. Phys. Chem. B* **2003**, *107*, 668.
4. Negishi, Y.; Nakazaki, T.; Malola, S.; Takano, S.; Niihori, Y.; Kurashige, W.; Yamazoe, S.; Tsukuda, T.; Häkkinen, H. *J. Am. Chem. Soc.* **2015**, *137*, 1206.
5. Higaki, T.; Zhou, M.; Lambright, K. J.; Kirschbaum, K.; Sfeir, M. Y.; Jin, R. *J. Am. Chem. Soc.* **2018**, *140*, 5691.
6. Wen, F.; Englert, U.; Homberger, M.; Simon, U. *Z. Anorg. Allg. Chem.* **2006**, *632*, 2159.
7. Schulz-Dobrick, M.; Jansen, M. *Eur. J. Inorg. Chem.* **2006**, *2006*, 4498.
8. Schulz-Dobrick, M.; Jansen, M. *Inorg. Chem.* **2007**, *46*, 4380.
9. Schulz-Dobrick, M.; Jansen, M. *Z. Anorg. Allg. Chem.* **2008**, *634*, 2880.
10. Wen, F.; Englert, U.; Gutrath, B.; Simon, U. *Eur. J. Inorg. Chem.* **2008**, *2008*, 106.
11. Yamazoe, S.; Matsuo, S.; Muramatsu, S.; Takano, S.; Nitta, K.; Tsukuda, T. *Inorg. Chem.* **2017**, *56*, 8319.
12. Qian, H.; Eckenhoff, W. T.; Zhu, Y.; Pintauer, T.; Jin, R. *J. Am. Chem. Soc.* **2010**, *132*, 8280.
13. Tian, S.; Li, Y. Z.; Li, M. B.; Yuan, J.; Yang, J.; Wu, Z.; Jin, R. *Nat. Commun.* **2015**, *6*, 8667.
14. Chen, Y.; Liu, C.; Tang, Q.; Zeng, C.; Higaki, T.; Das, A.; Jiang, D. E.; Rosi, N. L.; Jin, R. *J. Am. Chem. Soc.* **2016**, *138*, 1482.
15. Xia, N.; Yuan, J.; Liao, L.; Zhang, W.; Li, J.; Deng, H.; Yang, J.; Wu, Z. *J. Am. Chem. Soc.* **2020**, *142*, 12140.
16. Guan, Z. J.; Hu, F.; Li, J. J.; Wen, Z. R.; Lin, Y. M.; Wang, Q. M. *J. Am. Chem. Soc.* **2020**, *142*, 2995.
17. Liu, X.; Xu, W. W.; Huang, X.; Wang, E.; Cai, X.; Zhao, Y.; Li, J.; Xiao, M.; Zhang, C.; Gao, Y.; Ding, W.; Zhu, Y. *Nat. Commun.* **2020**, *11*, 3349.
18. Zhuang, S.; Liao, L.; Zhao, Y.; Yuan, J.; Yao, C.; Liu, X.; Li, J.; Deng, H.; Yang, J.; Wu, Z. *Chem. Sci.* **2018**, *9*, 2437.
19. Zhuang, S.; Liao, L.; Yuan, J.; Xia, N.; Zhao, Y.; Wang, C.; Gan, Z.; Yan, N.; He, L.; Li, J.; Deng, H.; Guan, Z.; Yang, J.; Wu, Z. *Angew. Chem. Int. Ed.* **2019**, *58*, 4510.
20. Chen, S.; Xiong, L.; Wang, S.; Ma, Z.; Jin, S.; Sheng, H.; Pei, Y.; Zhu, M. *J. Am.*

Chem. Soc. **2016**, *138*, 10754.
21. Xiong, L.; Yang, S.; Sun, X.; Chai, J.; Rao, B.; Yi, L.; Zhu, M.; Pei, Y. *J. Phys. Chem. C* **2018**, *122*, 14898.
22. Zeng, C.; Li, T.; Das, A.; Rosi, N. L.; Jin, R. *J. Am. Chem. Soc.* **2013,** *135*, 10011.
23. Dass, A.; Jones, T.; Rambukwella, M.; Crasto, D.; Gagnon, K. J.; Sementa, L.; De Vetta, M.; Baseggio, O.; Aprà, E.; Stener, M.; Fortunelli, A. *J. Phys. Chem. C* **2016**, *120*, 6256.
24. Higaki, T.; Liu, C.; Zeng, C.; Jin, R.; Chen, Y.; Rosi, N. L.; Jin, R. *Angew. Chem. Int. Ed.* **2016**, *55*, 6694.
25. Zeng, C.; Qian, H.; Li, T.; Li, G.; Rosi, N. L.; Yoon, B.; Barnett, R. N.; Whetten, R. L.; Landman, U.; Jin, R. *Angew. Chem. Int. Ed.* **2012**, *51*, 13114.
26. Das, A.; Liu, C.; Zeng, C.; Li, G.; Li, T.; Rosi, N. L.; Jin, R. *J. Phys. Chem. A* **2014**, *118*, 8264.
27. Nimmala, P. R.; Knoppe, S.; Jupally, V. R.; Delcamp, J. H.; Aikens, C. M.; Dass, A. *J. Phys. Chem. B* **2014**, *118*, 14157.
28. Dong, H.; Liao, L.; Zhuang, S.; Yao, C.; Chen, J.; Tian, S.; Zhu, M.; Liu, X.; Li, L.; Wu, Z. *Nanoscale* **2017**, *9*, 3742.
29. Zeng, C.; Chen, Y.; Liu, C.; Nobusada, K.; Rosi, N. L.; Jin, R. *Sci. Adv.* **2015**, *1*, e1500425.
30. Zhuang, S.; Liao, L.; Li, M. B.; Yao, C.; Zhao, Y.; Dong, H.; Li, J.; Deng, H.; Li, L.; Wu, Z. *Nanoscale* **2017**, *9*, 14809.
31. Heaven, M. W.; Dass, A.; White, P. S.; Holt, K. M.; Murray, R. W. *J. Am. Chem. Soc.* **2008**, *130*, 3754.
32. Zhu, M.; Aikens, C. M.; Hollander, F. J.; Schatz, G. C.; Jin, R. *J. Am. Chem. Soc.* **2008**, *130*, 5883.
33. Walter, M.; Akola, J.; Lopez-Acevedo, O.; Jadzinsky, P. D.; Calero, G.; Ackerson, C. J.; Whetten, R. L.; Grönbeck, H.; Häkkinen, H. *Proc. Natl. Acad. Sci. U. S. A.* **2008**, *105*, 9157.
34. Kang, X.; Chong, H.; Zhu, M. *Nanoscale* **2018**, *10*, 10758.
35. Negishi, Y.; Takasugi, Y.; Sato, S.; Yao, H.; Kimura, K.; Tsukuda, T. *J. Phys. Chem. B* **2006**, *110*, 12218.
36. Mooney, J.; Kambhampati, P. *J. Phys. Chem. Lett.* **2013**, *4*, 3316.
37. Negishi, Y.; Nobusada, K.; Tsukuda, T. *J. Am. Chem. Soc.* **2005**, *127*, 5261.
38. Das, A.; Li, T.; Nobusada, K.; Zeng, C.; Rosi, N. L.; Jin, R. *J. Am. Chem. Soc.* **2013**, *135*, 18264.
39. Tofanelli, M. A.; Salorinne, K.; Ni, T. W.; Malola, S.; Newell, B.; Phillips, B.;

Häkkinen, H.; Ackerson, C. J. *Chem. Sci.* **2016**, *7*, 1882.
40. Yamazoe, S.; Takano, S.; Kurashige, W.; Yokoyama, T.; Nitta, K.; Negishi, Y.; Tsukuda, T. *Nat. Commun.* **2016**, *7*, 10414.
41. Ankudinov, A. L.; Ravel, B.; Rehr, J. J.; Conradson, S. D. *Phys. Rev. B* **1998**, *58*, 7565.
42. Frisch, M. J.; Trucks, G. W.; Schlegel, H. B.; Scuseria, G. E.; Robb, M. A.; Cheeseman, J. R.; Scalmani, G.; Barone, V.; Petersson, G. A.; Nakatsuji, H.; Li, X.; Caricato, M.; Marenich, A.; Bloino, J.; Janesko, B. G.; Gomperts, R.; Mennucci, B.; Hratchian, H. P.; Ortiz, J. V.; Izmaylov, A. F.; Sonnenberg, J. L.; Williams-Young, D.; Ding, F.; Lipparini, F.; Egidi, F.; Goings, J.; Peng, B.; Petrone, A.; Henderson, T.; Ranasinghe, D.; Zakrzewski, V. G.; Gao, J.; Rega, N.; Zheng, G.; Liang, W.; Hada, M.; Ehara, M.; Toyota, K.; Fukuda, R.; Hasegawa, J.; Ishida, M.; Nakajima, T.; Honda, Y.; Kitao, O.; Nakai, H.; Vreven, T.; Throssell, K.; Montgomery Jr., J. A.; Peralta, J. E.; Ogliaro, F.; Bearpark, M.; Heyd, J. J.; Brothers, E.; Kudin, K. N.; Staroverov, V. N.; Keith, T.; Kobayashi, R.; Normand, J.; Raghavachari, K.; Rendell, A.; Burant, J. C.; Iyengar, S. S.; Tomasi, J.; Cossi, M.; Millam, J. M.; Klene, M.; Adamo, C.; Cammi, R.; Ochterski, J. W.; Martin, R. L.; Morokuma, K.; Farkas, O.; Foresman, J. B.; Fox, D. J. *Gaussian 09 Rev. C.01/D.01*, Wallingford, CT, 2013.
43. Shichibu, Y.; Negishi, Y.; Tsunoyama, H.; Kanehara, M.; Teranishi, T.; Tsukuda, T. *Small* **2007**, *3*, 835.
44. Wu, Z.; Suhan, J.; Jin, R. *J. Mater. Chem.* **2009**, *19*, 622.
45. Tofanelli, M. A.; Ackerson, C. J. *J. Am. Chem. Soc.* **2012**, *134*, 16937.
46. Jędrzejewska, H.; Szumna, A. *Chem. Rev.* **2017**, *117*, 4863.
47. Knoppe, S.; Bürgi, T. *Acc. Chem. Res.* **2014**, *47*, 1318.
48. Higaki, T.; Zeng, C.; Chen, Y.; Hussain, E.; Jin, R. *CrystEngComm* **2016**, *18*, 6979.

Chapter 3.

Reduction resistance of $[Au_{25}(SR)_{18}]^0$ protected by cyclohexanethiol

Omoda, T.; Takano, S.; Tsukuda, T.

Chem. Lett. **2019**, *48*, 885-887.

3.1. Introduction

Ligand-protected Au superatoms show unique redox properties correlated with their internal structures. Along with the oxidation or reduction, the geometrical structure of small Au superatoms also changes. For example, the two-electron redox process of $[Au_9(PR_3)_8]^{3+}$ and $[Au_9(PR_3)_8]^{+}$ with 6*e* and 8*e*, respectively, involves the structural transformation of Au_9 core between a crown and a cubic shape (Figure 3.1a).[1-8] $Au_{25}(SR)_{18}$ shows the gradual distortion of an icosahedral (Ih) Au_{13} core from an isotropic

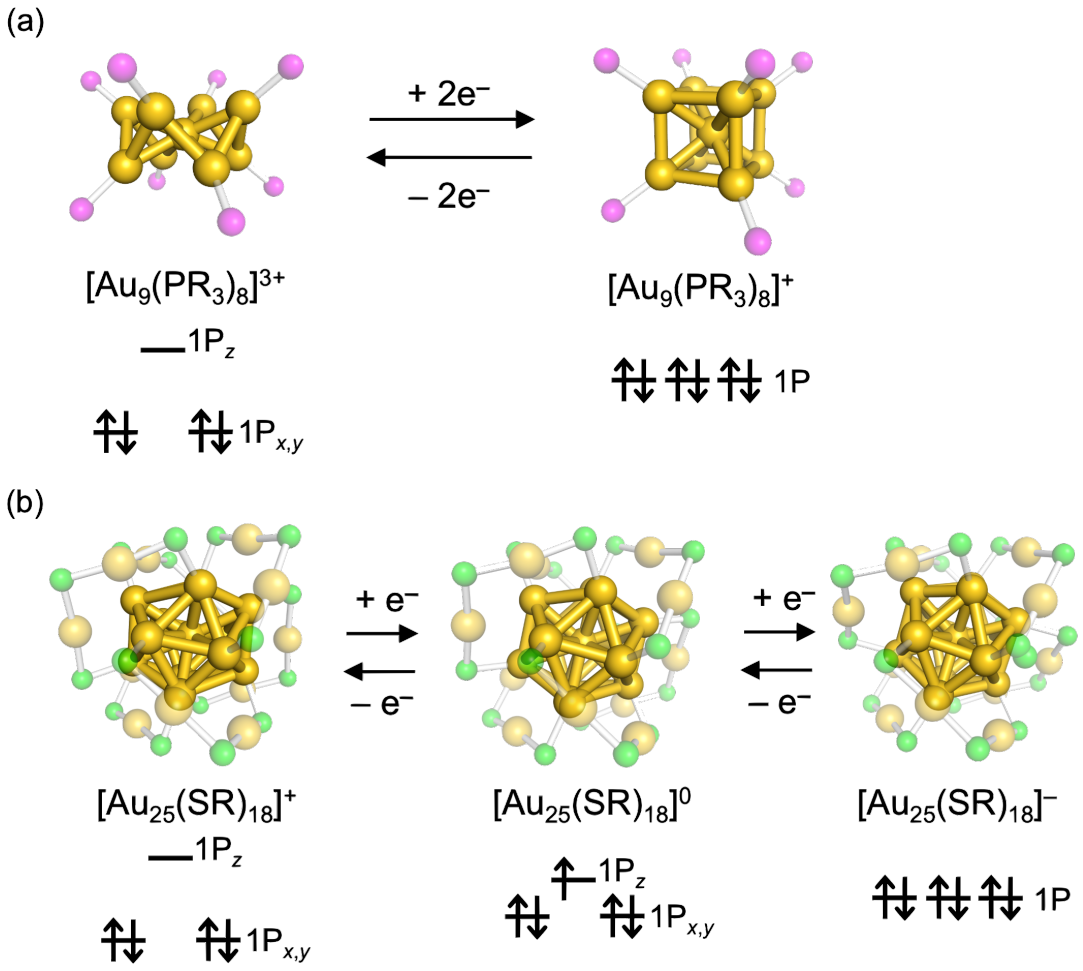

Figure 3.1. Structural transformation in accordance with the redox process in (a) $Au_9(PR_3)_8$ cluster[1-8] and (b) $Au_{25}(SR)_{18}$ cluster.[9-12] The superatomic electron configuration of each cluster is also shown. R group is omitted and the ligand layer is semi-transparently shown for clarity. Color code: yellow (Au); magenta (P); green (S).

to an oblate shape as oxidation proceeds from anion (8*e*) to neutral (7*e*) and cation (6*e*) (Figure 3.1b).[9-12] The structural change in accordance with the oxidation/reduction is due to the Jahn-Teller effect. In 8*e* system, superatoms take an isotropic shape like a cubic or an Ih structure to form a closed shell of $(1S)^2(1P)^6$ (Figure 3.1). However, in 6*e* or 7*e* system, isotropic superatoms oblately deform to stabilize the system by splitting the degenerated superatomic 1P orbitals (Figure 3.1). The degree of structural change in $Au_9(PR_3)_8$ is larger than that in $Au_{25}(SR)_{18}$ probably because of the different nature of ligand layer each other; Au_{13} core of $Au_{25}(SR)_{18}$ is protected by $Au_2(SR)_3$ oligomers in a bidentate fashion through stiff Au–S bonds while Au_9 core of $Au_9(PR_3)_8$ is protected by monodentate PR_3 through relatively soft Au–P bonds.[7,13] On the other hand, large Au superatoms such as $Au_{102}(SR)_{44}$, $Au_{133}(SR)_{52}$, and $Au_{144}(SR)_{60}$ do not show such structural change upon redox process judging from their optical absorption spectra.[14-16] Probably, the degree of structural distortion and the orbital splitting by the Jahn-Teller effect becomes small in the larger size of superatoms.

The redox properties of Au superatoms can be tuned by heterometal doping. The effects of doping on the electronic structure of Au superatoms can be qualitatively predicted by a two-step jellium model in which the host and dopant atoms provide a different but uniform background positively charged.[17-20] Higher valence dopant atoms such as Hg and Cd make the effective potential more attractive and energetically stabilize the superatomic orbitals while the introduction of lower-valence dopant atoms such as Pd and Pt leads to the destabilization of the superatomic orbitals due to the less attractive nature of the potential (Figure 3.2). As a result, the electrochemical response of superatoms is modulated. For example, the electrochemical potentials of $XAu_{24}(SR)_{18}$ (X = Cd, Hg) and $YAu_{24}(SR)_{18}$ (Y = Pd, Pt) show a positive and negative shift, respectively,

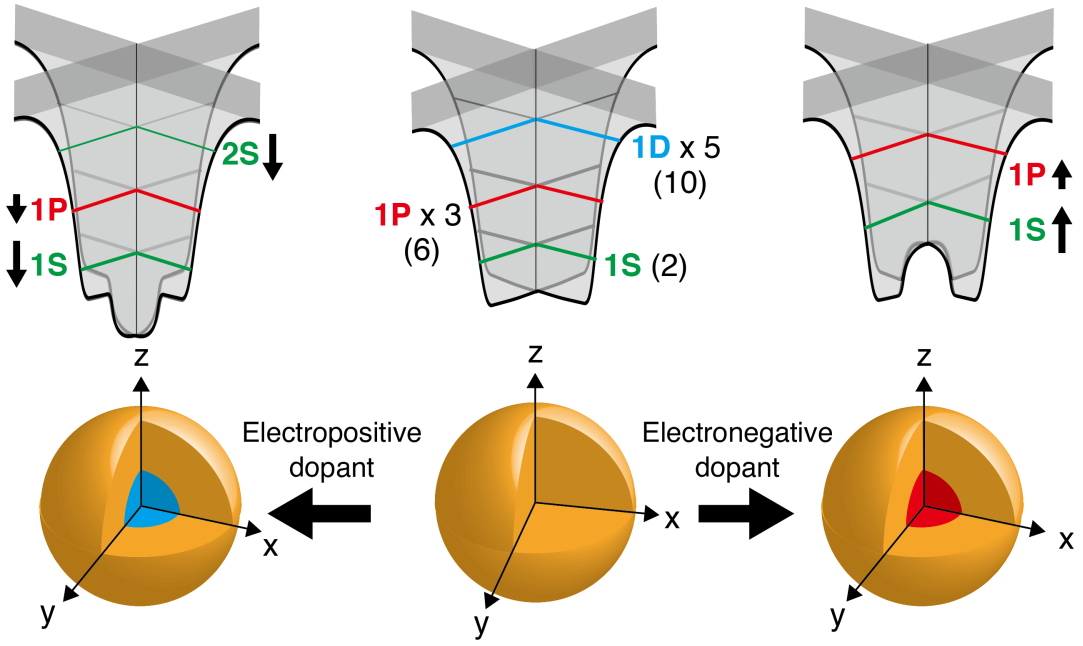

Figure 3.2. Schematic illustration of the doping effect on a jellium potential. The maximum number of electrons confined in superatomic 1S, 1P, and 1D orbitals is shown in parentheses. Reproduced with permission from ref. 20. Copyright 2020 Wiley-VCH.

compared to undoped $Au_{25}(SR)_{18}$.[21-23] In $[Au_{13}(dppe)_5Cl_2]^{3+}$ (dppe = 1,2-bis(diphenylphosphino)ethane), Ir dopant (group IX) induces a larger negative shift of the electrochemical potential than Pt dopant (group X) because the valence of Ir dopant is lower than that of Pt dopant.[24] Especially, when the lower valence elements such as Pd, Pt, and Ir are doped, an Ih Au_{13} core with 8*e* becomes prone to the oxidation to 7*e* or 6*e* system because of the negative shift of oxidation potentials.[21,22,24-29]

The redox property of Au-based superatoms is also modulated by ligands. The electrochemical potentials of $Au_{25}(SR)_{18}$ and $YAu_{24}(SR)_{18}$ are positively shifted by introducing the ligands which have halogen (-X) and nitro ($-NO_2$) substituents because their electron-withdrawing nature make the background potential of Au_{13} and YAu_{12} cores more attractive and stabilize the superatomic orbitals.[22,30,31] Redox potentials of $Au_{25}(SR)_{18}$ and $YAu_{24}(SR)_{18}$ are also tuned by changing RS ligands from the conventional

primary thiolate of PhEtS (PhEtSH = 2-phenylethanethiol) to the aryl thiolate of PhS (PhSH = benzenethiol) or *t*BuPhS (*t*BuPhSH = 4-*tert*-butylbenzenethiol).[29,30] In these cases, the steric effect of RS ligands is suggested because the aryl side chains are more bulky than PhEt group.[29]

In this chapter, to study the effect of the ligand bulkiness on the redox property of Au superatoms, I synthesized $Au_{25}(SR)_{18}$ using a bulky thiolate of cHexS (cHexSH = cyclohexanethiol, Scheme 3.1) which has a secondary α-carbon and larger bulkiness than aryl thiolates in the previous studies. The reduction behavior of $Au_{25}(ScHex)_{18}$ is compared with that of conventional $Au_{25}(SEtPh)_{18}$.

Scheme 3.1. Structure of cHexSH

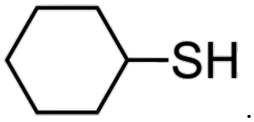

3.2. Experiment

3.2.1. Chemicals

All chemicals were commercially available and used without further purification. Tetrachloroauric acid tetrahydrate ($HAuCl_4 \cdot 4H_2O$), sodium borohydride ($NaBH_4$), dichloromethane (DCM), *n*-pentane, methanol (MeOH), ethanol (EtOH), and toluene were purchased from FUJIFILM Wako Pure Chemical Corporation. 2-phenylethanethiol (PhEtSH) and cyclohexanethiol (cHexSH) were purchased from Tokyo Chemical Industry. Tetrahydrofuran (THF) was purchased from Kanto Chemical. Tetra-*n*-octylammonium bromide (TOABr) was purchased from Sigma-Aldrich. Water was Milli-Q grade (ρ > 18 MΩ·cm).

3.2.2. General

Ultraviolet-visible (UV-vis) absorption spectra were measured by JASCO V-630, V-670, and V-770 spectrophotometers. The raw spectral data as functions of the wavelength could be converted to the energy-dependent data according to the procedure reported.[32]

3.2.3. Synthesis

3.2.3.1. $Au_{25}(ScHex)_{18}$

A crude sample of $Au_n(ScHex)_m$ was prepared by the reported protocol with modification.[33] $HAuCl_4 \cdot 4H_2O$ (0.5 mmol) and TOABr (0.55 mmol) were added in a 100 mL Erlenmeyer flask, dissolved in MeOH (25 mL), and then stirred for 15 min. To this reddish orange solution, cHexSH (2 mmol) was added to give a white suspension. After the stirring for 15 min, an ice-cooled aqueous solution of $NaBH_4$ (0.5 M, 10 mL) was added all at once. The reaction mixture was stirred for 8 h. Then, the transparent supernatant was discarded and the obtained oily product was transferred to two centrifugal tubes with a small amount of DCM. The product was precipitated by centrifugation (2300 rpm) with an excess amount of MeOH. The precipitate was further washed with MeOH by centrifugation (2300 rpm) three times and then dried in vacuo. A crude sample containing $Au_{25}(ScHex)_{18}$ was extracted with toluene from the dried product. The extracted solution was then evaporated and dried in vacuo.

The $Au_{25}(ScHex)_{18}$ cluster was fractionated from the crude mixture using a high-performance liquid chromatography (HPLC) system (Japan Analytical Industry LC-908). A preparative gel permeation chromatography (GPC) column (YMC Co., Ltd. T30000) was equipped with the system and UV chromatograms were monitored at 350 nm. The crude mixture in toluene (< 30 mg/mL, 1.5–2 mL) was eluted and recycled twice using

toluene as a mobile phase with a flow rate of 6 mL/min. The fraction containing $Au_{25}(ScHex)_{18}$ were collected manually, evaporated, and dried in vacuo.

$Au_{25}(ScHex)_{18}$ was recrystallized by the vapor diffusion of *n*-pentane into the toluene solution of the fractionated product at 20 ºC. Typical yield of $Au_{25}(ScHex)_{18}$ was 0.4 mg (~0.3% based on Au).

The synthesis of $Au_{25}(ScHex)_{18}$ was also attempted by the conventional scheme in THF solvent.[12,34] $HAuCl_4 \cdot 4H_2O$ (0.25 mmol) and TOABr (0.29 mmol) were dissolved in THF (7 mL) and then stirred for 15 min. To this reddish orange solution, cHexSH (1.35 mmol) was added and the mixture was further stirred for 8 h to give a colorless solution. Then, an ice-cooled aqueous solution of $NaBH_4$ (1.1 M, 2.4 mL) was added to the mixture all at once and the reaction was allowed to proceed for 88 h. After that, the optical absorption spectrum of crude product was taken.

3.2.3.2. $Au_{25}(SEtPh)_{18}$

$[Au_{25}(SEtPh)_{18}]^-$ and $[Au_{25}(SEtPh)_{18}]^0$ were synthesized by the reported protocols.[12]

3.2.4. Chemical reduction of $[Au_{25}(SR)_{18}]^0$

3.2.4.1. Reduction by 1 equiv of $NaBH_4$

To the THF solution of $[Au_{25}(SR)_{18}]^0$ (10 μM), 1/100 volume of EtOH solution of $NaBH_4$ (1 mM, 1 equiv for $[Au_{25}(SR)_{18}]^0$) was added and the mixed solution was stirred for 1 h. During the reduction, the UV-vis absorption spectrum of the solution was taken at certain period.

3.2.4.2. Reduction by 100 equiv of $NaBH_4$

To the mixed solution of THF and EtOH (THF:EtOH = 9:1) of $NaBH_4$ (2 mM, 2.15 mL), THF solution of $[Au_{25}(SR)_{18}]^0$ (20 μM, 2.15 mL) was added by drop for ~5 min. The solution was stirred for 1 h. During the reduction, the UV-vis absorption spectrum of the solution was taken at certain period.

3.2.5. X-ray crystallography

Single crystals suitable for X-ray study were grown by the vapor diffusion of *n*-pentane into the toluene solution of $Au_{25}(ScHex)_{18}$ at 5°C. The crystals were immersed in Paratone-N oil, scooped up, and rapidly frozen at 93 K by a cooled N_2 stream. A diffraction experiment was performed using a Rigaku VariMax Dual with a Saturn 724+ CCD detector and MoKα radiation. The data was corrected for Lorentz polarization and the absorption correction was done numerically. The obtained data was solved by SHELXS-2016 and the structure was refined using the full-matrix least-squares method on F^2 using SHLEXL-2018.[35] The diffused electron density of the crystal was treated by the SQUEEZE option in the PLATON program.[36,37] The void accessible by the solvent found by the SQUEEZE program was localized at a specific position (0.500, 0.500, 1.000) and the volume and electron density of the void were estimated to be 171 $Å^3$ and 53*e*, respectively. Assuming that the C and N atoms (r = 1.5 Å) and the H atom (r = 0.9 Å) occupy ca. 14 and ca. 3 $Å^3$, respectively, the volume and electron density of the void do not agree with those of TOA^+ ($N_1C_{32}H_{68}$: ca. 700 $Å^3$; 266*e*), but agree with those of toluene (C_7H_8: ca. 120$Å^3$; 50*e*). This comparison strongly suggests that the diffused solvent is mainly composed of a single toluene molecule. All non-hydrogen atoms except for solvent molecules were refined anisotropically and the hydrogens atoms were treated

as riding models. Since some cHex rings and toluene molecules showed static disorders, the bond length of organic parts has relatively large uncertainty. In addition, a few reflections were damped by a direct beam stopper due to the use of the MoKα radiation. However, these problems do not affect the main conclusion of this work because we mainly focused on the location of heavy atoms.

3.3. Results and discussion

3.3.1. Isolation of $Au_{25}(ScHex)_{18}$

For the synthesis of $Au_{25}(ScHex)_{18}$ cluster, the crude mixture of Au:ScHex was firstly prepared according to the procedure for $[Au_{23}(ScHex)_{16}]^-$.[33] To the MeOH solution of $HAuCl_4$ and TOABr, cHexSH was added to obtain Au(I)-ScHex complex. The complex was reduced by $NaBH_4$ and the crude mixture of Au:ScHex was obtained. Although this mixture majorly contained $[Au_{23}(ScHex)_{16}]^-$, it was easily separated by the precipitation with toluene. Figure 3.3a shows the UV-vis absorption spectra of the extract and precipitate with toluene. The spectral profile of the extract is featureless, but the precipitate has a characteristic peak at 575 nm and a hump at 460 nm which are consistent with the reported UV-vis absorption spectrum of $[Au_{23}(ScHex)_{16}]^-$ (Figure 3.3b).[33]

After the removal of $[Au_{23}(ScHex)_{16}]^-$, the crude mixture of Au:ScHex was further purified by HPLC with a preparative GPC column. Figure 3.4a shows a typical chromatogram of crude Au:ScHex clusters. The major portion was collected as **Fr1** and the small tail with longer retention time was collected as **Fr2**. Figure 3.4b shows the UV-vis absorption spectra of **Fr1** and **Fr2**. The spectral profile of **Fr1** is almost featureless, whereas the spectrum of **Fr2** has humps at 400–500 nm. Then, **Fr2** was purified by recrystallization with toluene/*n*-pentane. Figure 3.4b shows the UV-vis absorption

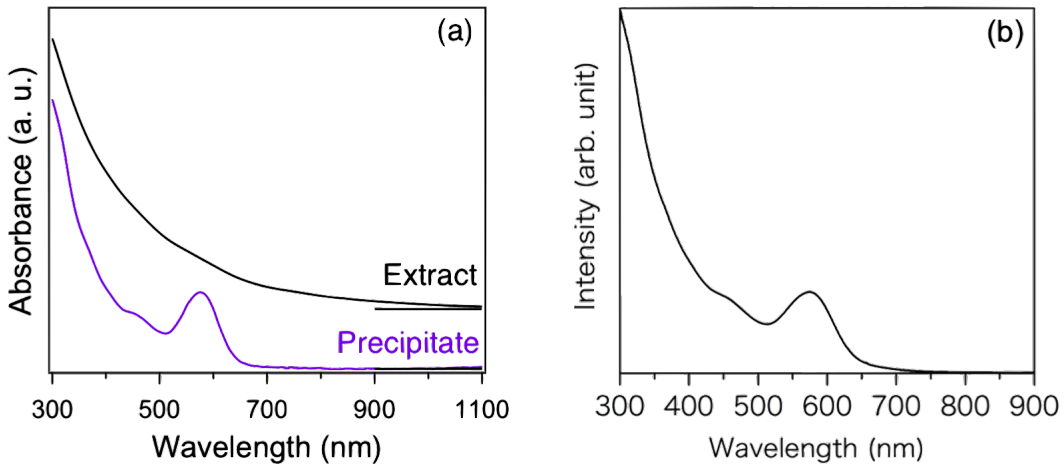

Figure 3.3. (a) UV-vis absorption spectra of (black) the extract and (purple) the precipitate of crude Au:ScHex with toluene. The spectrum of precipitate was taken after the washing with toluene several times. The spectrum of the extract is offset for clarity. (b) UV-vis absorption spectrum of $[Au_{23}(ScHex)_{16}]^{-}$.[33] (b) Adapted with permission from ref. 33. Copyright 2013, American Chemical Society.

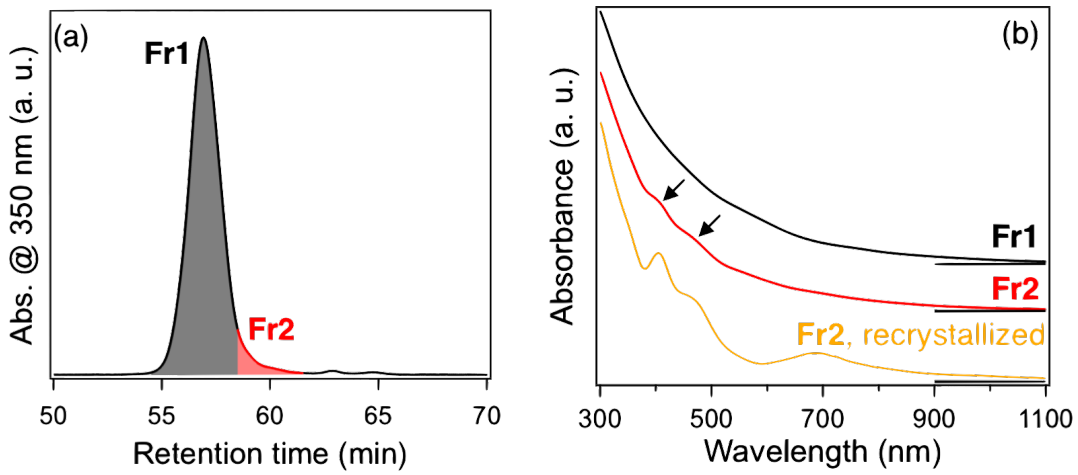

Figure 3.4. (a) Typical chromatogram of the crude Au:ScHex after recycled twice. (b) UV-vis absorption spectra of (black) **Fr1**, (red) **Fr2**, and (yellow) **Fr2** after the recrystallization by diffusing the vapor of *n*-pentane into toluene. The spectra are offset for clarity.

spectrum of thus purified product as yellow line. The spectral profile is quite similar to that of conventional $Au_{25}(SEtPh)_{18}$ in which there are one peak at 680 nm and two peaks around 400 nm.[10,12] From this result, it is concluded that $Au_{25}(ScHex)_{18}$ was successfully isolated. Because **Fr1** showed the shorter retention time than **Fr2** and the featureless UV-

vis absorption spectrum, it seemed to be a mixture of larger clusters such as $[Au_{28}(ScHex)_{20}]^0$, $[Au_{34}(ScHex)_{22}]^0$, $[Au_{42}(ScHex)_{26}]^0$, and $[Au_{43}(ScHex)_{25}]^0$.[38-40] It is worth mentioning that the yield of $Au_{25}(ScHex)_{18}$ was ~0.3 % based on Au, quite smaller than that of conventional $[Au_{25}(SEtPh)_{18}]^-$ (20–30 %).[12] This means that other sizes of clusters such as $[Au_{23}(ScHex)_{16}]^-$ and $[Au_{28}(ScHex)_{20}]^0$ are more stable and preferentially form rather than $Au_{25}(ScHex)_{18}$ at the present synthetic condition.[33,38] I also tried to synthesize $Au_{25}(ScHex)_{18}$ using THF as a solvent according to the conventional procedure for $Au_{25}(SR)_{18}$.[12,34] To the THF solution of $HAuCl_4$ and TOABr, cHexSH was added to obtain Au(I)-ScHex complex. The complex was reduced by $NaBH_4$ and the reaction solution was aged by stirring for 88 h. However, with using cHexSH, size-focusing into $Au_{25}(ScHex)_{18}$ was not observed. The characteristic peak of $Au_{25}(SR)_{18}$ around 700 nm is not observed in the UV-vis absorption spectrum of the reaction mixture after the aging (Figure 3.5). Probably, steric hinderance of a secondary α-carbon in cHexSH near the superatomic core inhibited the formation of $Au_{25}(ScHex)_{18}$ as empirically known.[41]

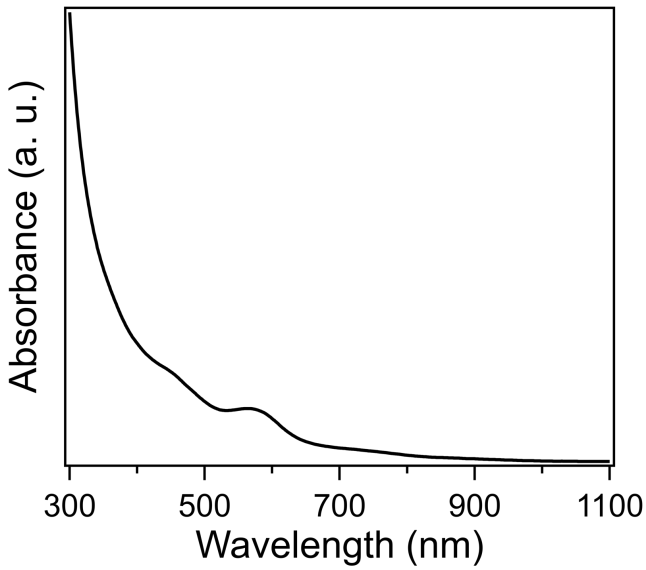

Figure 3.5. UV-vis absorption spectrum of the crude mixture of Au:ScHex clusters aged for 88 h in THF solvent.

3.3.2. Characterization of $Au_{25}(ScHex)_{18}$

3.3.2.1. Structure of $Au_{25}(ScHex)_{18}$

The single crystal X-ray structure of $Au_{25}(ScHex)_{18}$ is shown in Figure 3.6 and its crystal data obtained is summarized in Table 3.1. $Au_{25}(ScHex)_{18}$ is composed of an Ih Au_{13} core and six oligomers of $Au_2(cHex)_3$ as in the case of the conventional $[Au_{25}(SEtPh)_{18}]^-$.[9,10] To the best of my knowledge, this is the first example of $Au_{25}(SR)_{18}$ having an Ih Au_{13} core protected by a secondary thiolate. The crystal of $Au_{25}(ScHex)_{18}$ did not have a counter cation although TOA^+ firstly added in the synthesis is conventionally observed in the crystal of $[Au_{25}(SR)_{18}]^-$.[9,10] Instead of TOA^+, the crystal of $Au_{25}(ScHex)_{18}$ had toluene molecules as crystalline solvent as in the case of neutral $[Au_{25}(SEtPh)_{18}]^0$.[12]

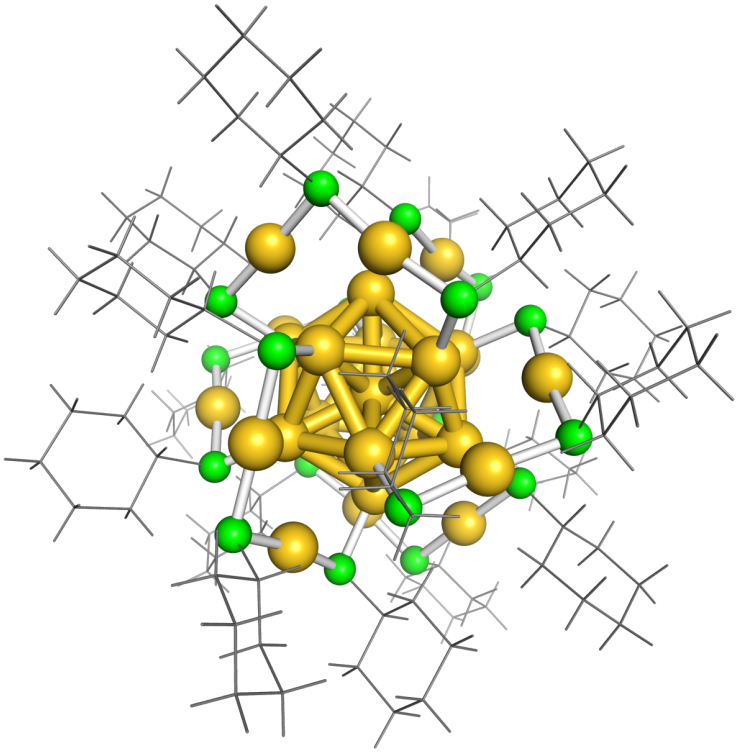

Figure 3.6. Single crystal X-ray structure of $Au_{25}(ScHex)_{18}$. Solvent molecules and disordered cHex rings are omitted for clarity. Color code: yellow (Au); Green (S). cHex ring is depicted as gray stick.

Table 3.1. Crystal data of $Au_{25}(ScHex)_{18}$.

Formula[a]	$C_{122}H_{214}Au_{25}S_{18}$
FW[a] (g mol^{-1})	7182.16
Crystal color and habit	Black platelet
Crystal size (mm)	0.14 × 0.10 × 0.02
Crystal system	Triclinic
Space group	*P*-1
a (Å)	16.2117(14)
b (Å)	16.9365(14)
c (Å)	17.8025(15)
α (º)	111.820(9)
β (º)	116.781(5)
γ (º)	93.400(7)
V (Å^3)	3896.5(6)
Z	1
T (K)	90(2)
Completeness to theta =	99.7 %
ρ_{calc} (g cm^{-3})	3.061
μ (mm^{-1})	23.704
Max. and min. transmission	0.639 and 0.162
F(000)	3209
θ range (º)	2.420–27.104
Index ranges	$-20 \le h \le 18$, $-21 \le k \le 21$, $-22 \le l \le 22$
Collected reflections	66216
Independent reflections	17117 (R_{int} = 0.0523)
Data/restrains/parameters	17117/1206/966
Goodness-of-fit on F^2	1.074
Final $R^{b,c}$ indices [$I > 2\sigma(I)$]	R_1 = 0.0443, wR_2 = 0.0896
Final $R^{b,c}$ indices [all data]	R_1 = 0.0520, wR_2 = 0.0944
$(\Delta\rho)_{max,min}$ (e Å^{-3})	2.956–3.075

[a]Including solvent molecules. [b]$R_1 = \Sigma(||F_o| - |F_c||)/\Sigma|F_o|$. [c]$wR_2 = [\Sigma[w(F_o^2 - F_c^2)^2]/\Sigma[w(F_o^2)^2]]^{1/2}$, $w = 1/[\sigma^2(F_o^2) + (ap)^2 + bp]$, where $p = [\max(F_o^2, 0) + 2F_c^2]/3$.

3.3.2.2. Charge state of $Au_{25}(ScHex)_{18}$ cluster

To check the charge state of $Au_{25}(ScHex)_{18}$, its UV-vis absorption spectrum was measured. Figure 3.7 compares UV-vis absorption spectra of $Au_{25}(ScHex)_{18}$ and the references of $[Au_{25}(SEtPh)_{18}]^{0/-}$ with anionic and neutral charge. As explained above (section 3.1), $[Au_{25}(SR)_{18}]^{-}$ has 8*e* with a closed shell of $(1S)^2(1P)^6$, whereas $[Au_{25}(SR)_{18}]^{0}$ has 7*e* with an open electron configuration of $(1S)^2(1P)^5$.[12,42,43] The spectrum of $Au_{25}(ScHex)_{18}$ shows three common features with $[Au_{25}(SEtPh)_{18}]^{0}$ which

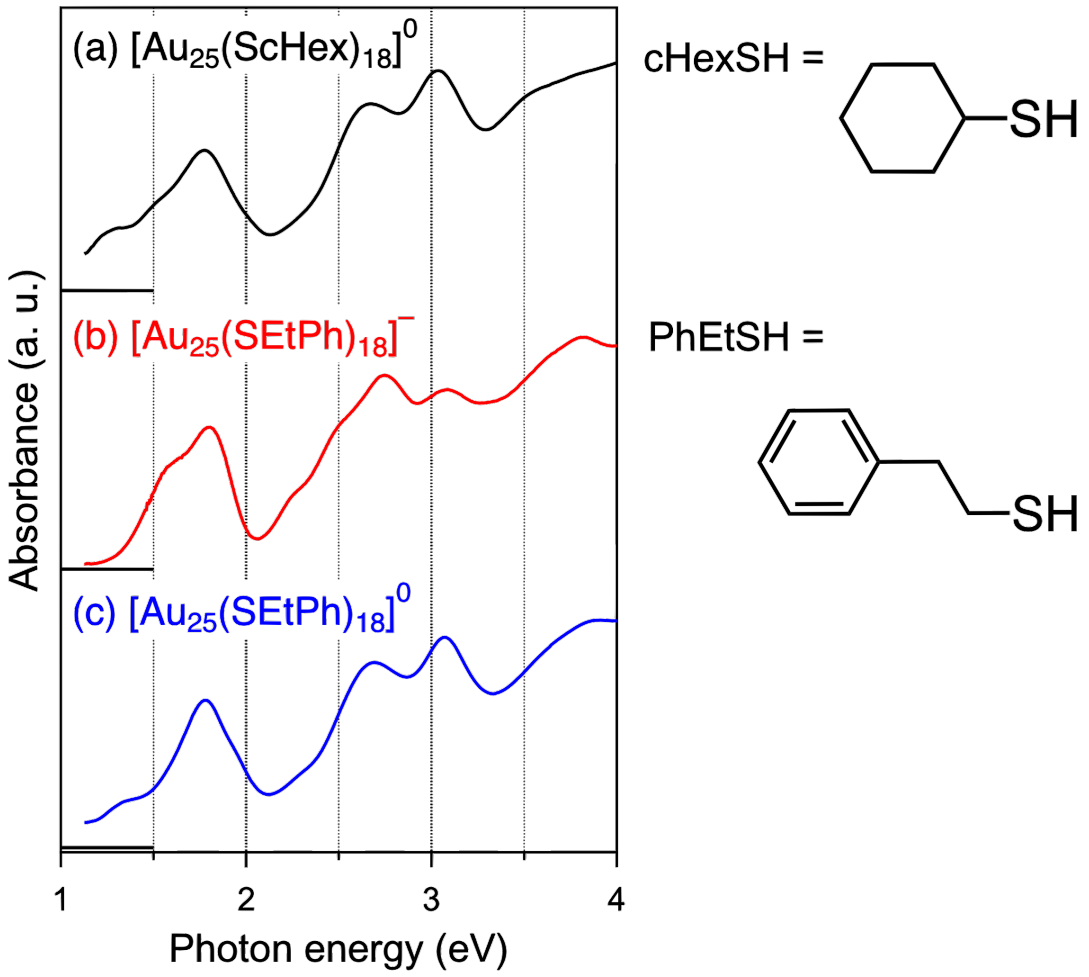

Figure 3.7. UV-vis absorption spectra of (a) $Au_{25}(ScHex)_{18}$, (b) $[Au_{25}(SEtPh)_{18}]^{-}$, and $[Au_{25}(SEtPh)_{18}]^{0}$. The spectra are offset for clarity. The structures of cHexSH and PhEtSH are also shown

are different from the spectrum of $[Au_{25}(SEtPh)_{18}]^{-}$; (1) the spectral onset was red-shifted < 1.1 eV. (2) the hump at 1.6 eV observed for $[Au_{25}(SEtPh)_{18}]^{-}$ is absent. (3) the peak at 2.7 eV is weaker than the peak at 3.1 eV. From the results of X-ray crystallography and UV-vis absorption spectroscopy, it is concluded that $Au_{25}(ScHex)_{18}$ was isolated as neutral species, although the conventional $Au_{25}(SR)_{18}$ prefers a singly charged anion to form a closed shell with 8*e*.

3.3.3. Reduction behavior of $[Au_{25}(SR)_{18}]^0$

3.3.3.1. Chemical reduction by 1 equiv of $NaBH_4$

The results of X-ray crystallography and UV-vis absorption spectroscopy suggest that $Au_{25}(ScHex)_{18}$ prefers the neutral state with an open electron configuration of $(1S)^2(1P)^5$ rather than the anion with a closed shell of $(1S)^2(1P)^6$. This hypothesis was tested by comparing the chemical reduction rate between $[Au_{25}(ScHex)_{18}]^0$ and $[Au_{25}(SEtPh)_{18}]^0$ with using $NaBH_4$ as a reducing agent. Figure 3.8 displays the time-course UV-vis absorption spectra of $[Au_{25}(ScHex)_{18}]^0$ and $[Au_{25}(SEtPh)_{18}]^0$ with 1 equiv of $NaBH_4$. The spectral feature of $[Au_{25}(ScHex)_{18}]^0$ did not change even 60 min after the addition of $NaBH_4$ (Figure 3.8a), indicating the negligibly small reduction rate of $[Au_{25}(ScHex)_{18}]^0$. In contrast, Figure 3.8b shows that the spectral profile of conventional $[Au_{25}(SEtPh)_{18}]^0$ became similar to that of $[Au_{25}(SEtPh)_{18}]^{-}$ (Figure 3.7b) within 20 min after the addition of $NaBH_4$. This result indicates that a one-electron reduction completed as reported previously.[43] From these results, it is concluded that $Au_{25}(ScHex)_{18}$ had resistance to the formation of 8*e* closed shell compared to conventional $[Au_{25}(SEtPh)_{18}]^0$.

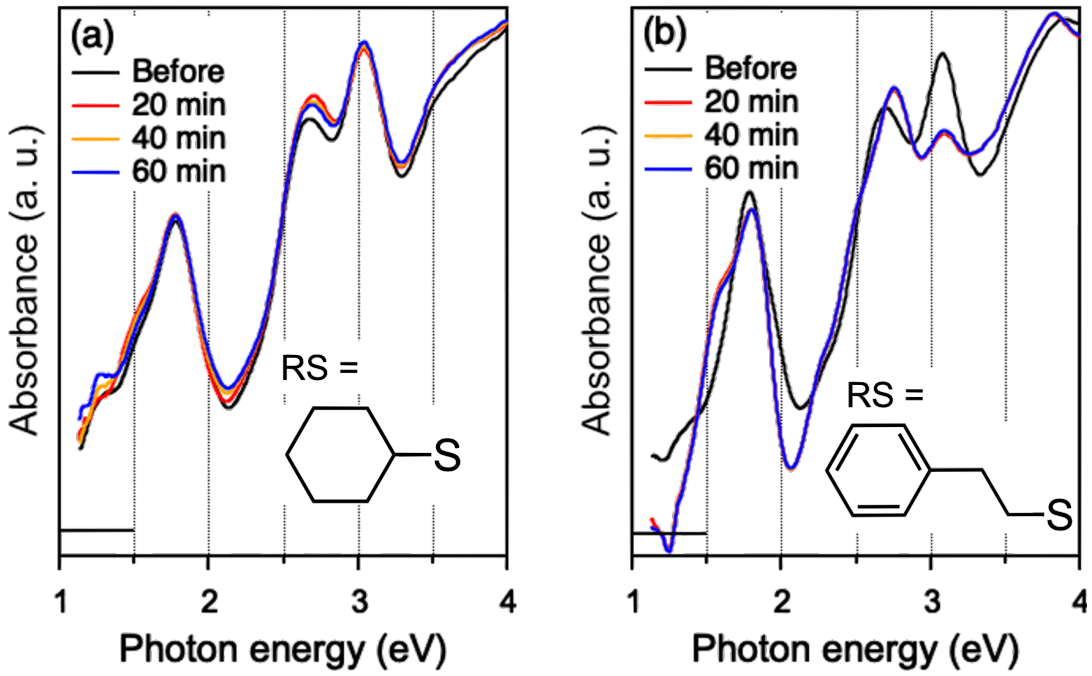

Figure 3.8. Time-course UV-vis absorption spectra of (a) $[Au_{25}(ScHex)_{18}]^0$ and (b) $[Au_{25}(SEtPh)_{18}]^0$ after the addition of 1 equiv of $NaBH_4$. The spectra are normalized by the concentration of the solution. The structures of RS ligands are shown in each panel.

3.3.3.2. Reduction resistance of $[Au_{25}(SR)_{18}]^0$

To gain an insight into the origin of the reduction-resistant nature of $[Au_{25}(ScHex)_{18}]^0$, I closely compared the geometrical structure of the Au_{13} core in $[Au_{25}(ScHex)_{18}]^0$, $[Au_{25}(SEtPh)_{18}]^0$, and $[Au_{25}(SEtPh)_{18}]^-$. Figure 3.9 shows the heatmaps and histograms of Au–Au bond lengths within the Ih Au_{13} cores of $[Au_{25}(ScHex)_{18}]^0$, $[Au_{25}(SEtPh)_{18}]^0$, and $[Au_{25}(SEtPh)_{18}]^-$.[10,12] The average lengths of radial and lateral Au–Au bonds are shown in Table 3.2. A comparison of Figures 3.9a and b demonstrates that the Au_{13} core of $[Au_{25}(SEtPh)_{18}]^0$ is oblately distorted by the Jahn-Teller effect while that of $[Au_{25}(SEtPh)_{18}]^-$ is isotropic as reported previously.[12] Because of such distortion, the length distribution of Au–Au bonds in $[Au_{25}(SEtPh)_{18}]^0$ is broader than that of

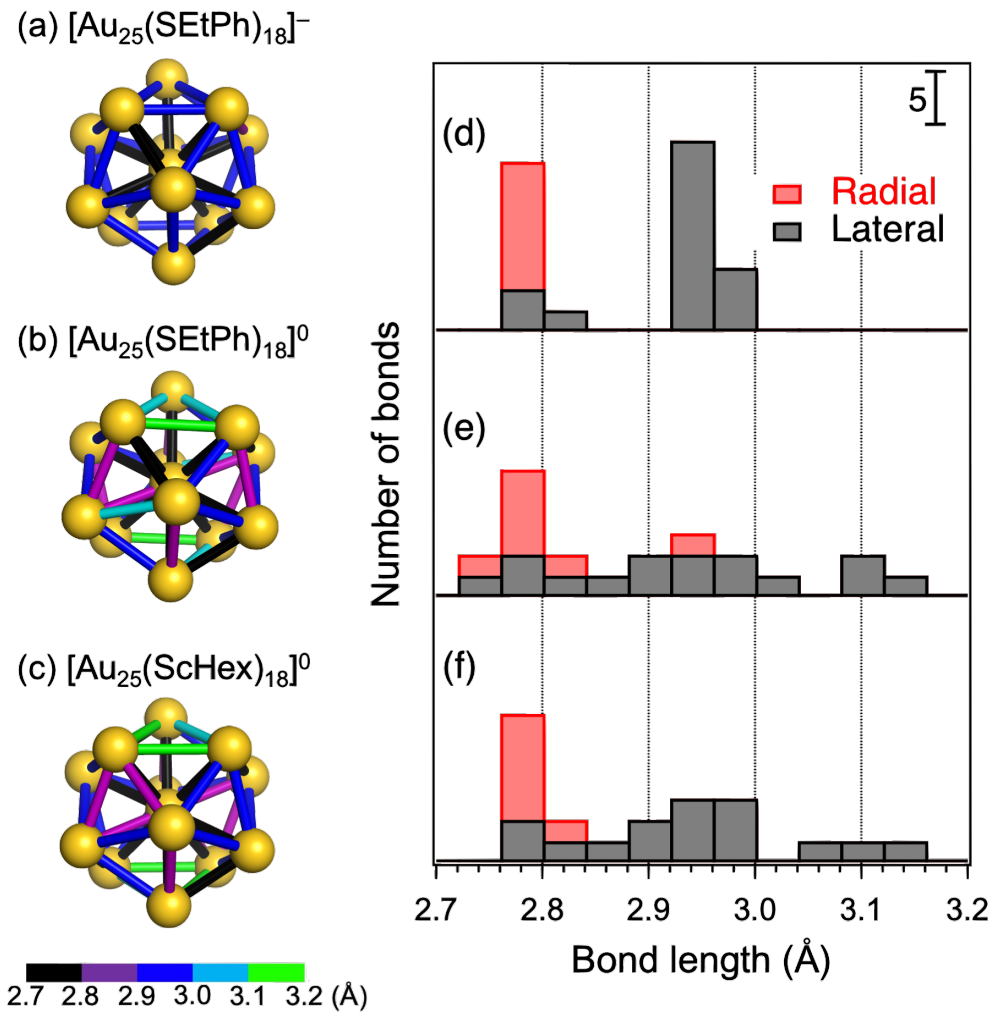

Figure 3.9. (Left) Heatmaps of Au–Au bond lengths within the Ih Au_{13} cores of (a) $[Au_{25}(SEtPh)_{18}]^{-}$, (b) $[Au_{25}(SEtPh)_{18}]^{0}$, and (c) $[Au_{25}(ScHex)_{18}]^{0}$.[10,12] (Right) Histograms of Au–Au bond lengths within the Ih Au_{13} cores of (d) $[Au_{25}(SEtPh)_{18}]^{-}$, (e) $[Au_{25}(SEtPh)_{18}]^{0}$, and (f) $[Au_{25}(ScHex)_{18}]^{0}$.[10,12] The red and black bars indicate the radial and lateral Au–Au bonds, respectively.

Table 3.2. Average lengths of the radial and lateral Au–Au bonds within the Ih Au_{13} cores of $[Au_{25}(SEtPh)_{18}]^{-}$, $[Au_{25}(SEtPh)_{18}]^{0}$, and $[Au_{25}(ScHex)_{18}]^{0}$.[10,12]

Cluster	Radial length (Å)	Lateral length (Å)
$[Au_{25}(SEtPh)_{18}]^{-}$ (ref. 10)	2.78(1)	2.92(6)
$[Au_{25}(SEtPh)_{18}]^{0}$ (ref. 12)	2.78(2)	2.92(12)
$[Au_{25}(ScHex)_{18}]^{0}$	2.79(1)	2.94(10)

$[Au_{25}(SEtPh)_{18}]^{-}$, especially for the lateral bonds on the surface (Figures 3.9d and e, Table 3.2).[10,12] Therefore, the fast reduction of $[Au_{25}(SEtPh)_{18}]^{0}$ indicates that its oblately deformed Au_{13} core can be easily relaxed to the higher symmetrical structure upon the reduction. Figures 3.9c and f and Table 3.2 show that the Ih Au_{13} core of $[Au_{25}(ScHex)_{18}]^{0}$ is also distorted like that of $[Au_{25}(SEtPh)_{18}]^{0}$. Thus, the retardation of the reduction of $[Au_{25}(ScHex)_{18}]^{0}$ is ascribed to the difficulty in structural relaxation from the oblately distorted Ih Au_{13} core to the symmetrical one.

In order to verify the above hypothesis, I checked the cHexS ligand layer of $[Au_{25}(ScHex)_{18}]^{0}$ in detail. Compared with $[Au_{25}(SEtPh)_{18}]^{0}$ protected by primary thiolate of PhEtS, the ligand layer of $[Au_{25}(ScHex)_{18}]^{0}$ protected by secondary thiolate of cHexS was more crowded. Although the bond length of organic parts has uncertainty in the crystal structure of $[Au_{25}(ScHex)_{18}]^{0}$, there were close contacts between cHexS ligands and $Au_2(ScHex)_3$ oligomers; some of the distances between α- or β-H of cHexS and Au atoms in $Au_2(ScHex)_3$ were almost equal to 2.9 Å which corresponds to the sum of van der Waals radii of H (1.20 Å) and Au (1.66 Å) (Figure 3.10).[44] Therefore, the reduction-resistance of $[Au_{25}(ScHex)_{18}]^{0}$ can be understood as the schematic illustration in Figure 3.11. During the reduction from $[Au_{25}(ScHex)_{18}]^{0}$ to $[Au_{25}(ScHex)_{18}]^{-}$, it is necessary to relax the Jahn-Teller distorted Au_{13} core to a spherical one after the electron attachment. However, the ligand layer of cHexS is so bulky and crowded that such relaxation was inhibited. As a result, the electron was detached and the reduction of $[Au_{25}(ScHex)_{18}]^{0}$ did not proceed.

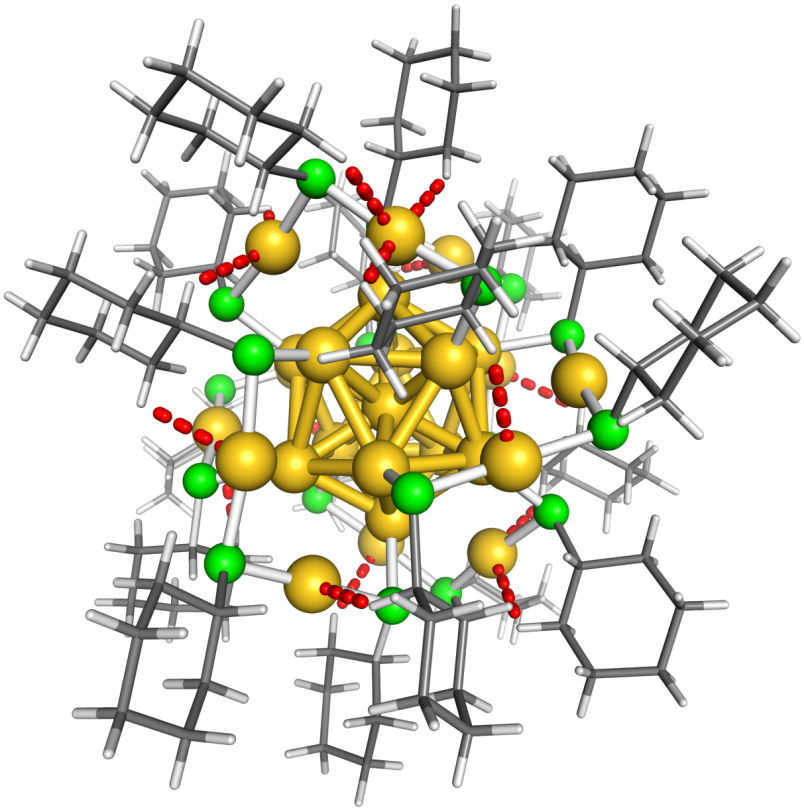

Figure 3.10. Single crystal X-ray structure of $[Au_{25}(ScHex)_{18}]^0$ with showing the contacts between α- or β-H of cHexS group and Au in $Au_2(ScHex)_3$ oligomer (~2.9 Å) as red dashed lines. The number of contacts were 18. C and H atoms in cHex ring are depicted as gray and white sticks, respectively. Solvent molecules and disordered cHex rings are omitted for clarity. Color code: yellow (Au); Green (S).

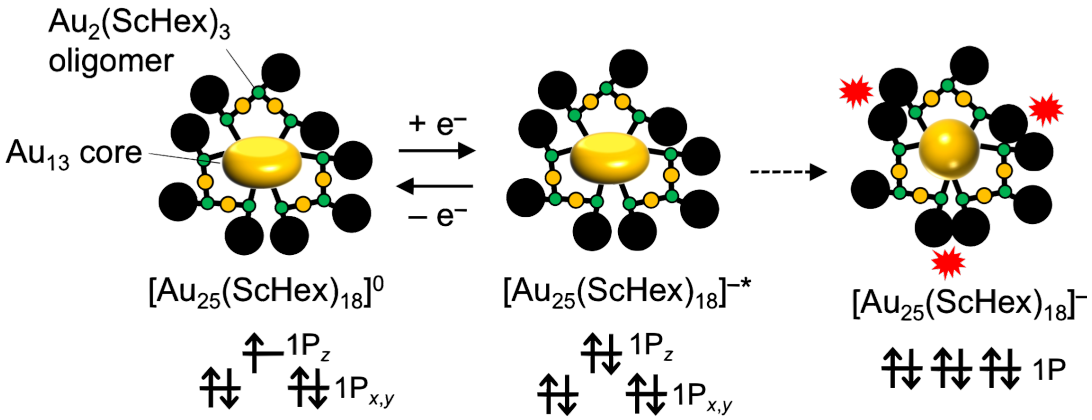

Figure 3.11. Schematic illustration of the reduction-resistant nature of $[Au_{25}(ScHex)_{18}]^0$. Au_{13} core and cHexS group are depicted as a yellow oval or sphere and a black circle, respectively. Color code: yellow (Au); green (S).

3.3.3.3. Chemical reduction by 100 equiv of $NaBH_4$

According to the proposed mechanism, the reduction from $[Au_{25}(ScHex)_{18}]^0$ to $[Au_{25}(ScHex)_{18}]^-$ proceeds if the electron detachment from an intermediate species is suppressed. To check that, I tentatively tried the reduction of $[Au_{25}(ScHex)_{18}]^0$ with an excess amount of $NaBH_4$. Figure 3.12 shows the time-course UV-vis absorption spectra of $[Au_{25}(ScHex)_{18}]^0$ with 100 equiv of $NaBH_4$. After the addition of $NaBH_4$, the spectral profile gradually became similar to that of conventional $[Au_{25}(SEtPh)_{18}]^-$ (Figure 3.7b); the hump at 1.6 eV emerged and the relative intensity of the peaks at 2.7 eV and 3.1 eV was inversed. This result indicates that the reduction of $[Au_{25}(ScHex)_{18}]^0$ proceeds with an excess amount of $NaBH_4$ as expected.

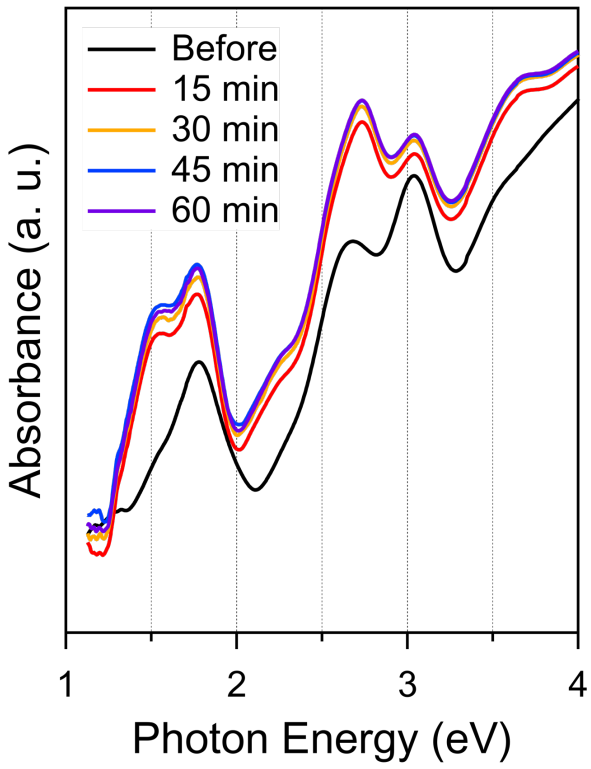

Figure 3.12. Time-course UV-vis absorption spectra of $[Au_{25}(ScHex)_{18}]^0$ after the addition of 100 equiv of $NaBH_4$. The spectra are normalized by the concentration of solution.

3.4. Summary

In this Chapter, I successfully synthesized $[Au_{25}(ScHex)_{18}]^0$ as a minor byproduct of $[Au_{23}(ScHex)_{16}]^-$. From the results of single crystal X-ray diffraction analysis and UV-vis absorption spectroscopy, $[Au_{25}(ScHex)_{18}]^0$ had the same structural motif as the conventional $[Au_{25}(SEtPh)_{18}]^0$, an oblately distorted Ih Au_{13} core by the Jahn-Teller effect with six oligomers of $Au_2(ScHex)_3$. Interestingly, $[Au_{25}(ScHex)_{18}]^0$ with an open electron configuration of $(1S)^2(1P)^5$ had resistance to the reduction to form an electronic shell closure of $(1S)^2(1P)^6$. In contrast, conventional $[Au_{25}(SEtPh)_{18}]^0$ was easily reduced to $[Au_{25}(SEtPh)_{18}]^-$ along with the transformation of its Au_{13} core from an oblate to an isotropic shape. The retardation of the reduction of $[Au_{25}(ScHex)_{18}]^0$ was ascribed to that the structural relaxation of the Jahn-Teller distorted Au_{13} core to an isotropic shape was inhibited by the steric hinderance of cHexS ligands (Figure 3.11).

References

1. Hall, K. P.; Theoblad, B. R. C.; Gilmour, D. I.; Mingos, D. M. P.; Welch, A. J. *J. Chem. Soc., Chem. Commun.* **1982**, 528.
2. Briant, C. E.; Hall, K. P.; Mingos, D. M. P. *J. Chem. Soc., Chem. Commun.* **1984**, 290.
3. van der Velden, J. W. A.; Bour, J. J.; Bosman, W. P.; Noordik, J. H.; Beurskens, P. T. *Recl. Trav. Chim. Pays-Bas* **1984**, *103*, 13.
4. Schulz-Dobrick, M.; Jansen, M. *Eur. J. Inorg. Chem.* **2006**, *2006*, 4498.
5. Schulz-Dobrick, M.; Jansen, M. *Z. Anorg. Allg. Chem.* **2008**, *634*, 2880.
6. Gutrath, B. S.; Merkens, C.; Schiefer, F.; Englert, U.; Schmid, G.; Simon, U. *Z. Naturforsch. B* **2013**, *68*, 569.
7. Yamazoe, S.; Matsuo, S.; Muramatsu, S.; Takano, S.; Nitta, K.; Tsukuda, T. *Inorg. Chem.* **2017**, *56*, 8319.
8. Shen, H.; Selenius, E.; Ruan, P.; Li, X.; Yuan, P.; Lopez-Estrada, O.; Malola, S.; Lin, S.; Teo, B. K.; Häkkinen, H.; Zheng, N. *Chem. Euro. J.* **2020**, *26*, 8465.
9. Heaven, M. W.; Dass, A.; White, P. S.; Holt, K. M.; Murray, R. W. *J. Am. Chem. Soc.* **2008**, *130*, 3754.
10. Zhu, M.; Aikens, C. M.; Hollander, F. J.; Schatz, G. C.; Jin, R. *J. Am. Chem. Soc.* **2008**, *130*, 5883.
11. Zhu, M.; Eckenhoff, W. T.; Pintauer, T.; Jin, R. *J. Phys. Chem. C* **2008**, *112*, 14221.
12. Tofanelli, M. A.; Salorinne, K.; Ni, T. W.; Malola, S.; Newell, B.; Phillips, B.; Häkkinen, H.; Ackerson, C. J. *Chem. Sci.* **2016**, *7*, 1882.
13. Yamazoe, S.; Takano, S.; Kurashige, W.; Yokoyama, T.; Nitta, K.; Negishi, Y.; Tsukuda, T. *Nat. Commun.* **2016**, *7*, 10414.
14. Chaki, N. K.; Negishi, Y.; Tsunoyama, H.; Shichibu, Y.; Tsukuda, T. *J. Am. Chem. Soc.* **2008**, *130*, 8608.
15. Zeng, C.; Weitz, A.; Withers, G.; Higaki, T.; Zhao, S.; Chen, Y.; Gil, R. R.; Hendrich, M.; Jin, R. *Chem. Sci.* **2019**, *10*, 9684.
16. Window, P. S.; Ackerson, C. J. *Inorg. Chem.* **2020**, *59*, 3509.
17. Zhang, S. B.; Cohen, M. L.; Chou, M. Y. *Phys. Rev. B* **1987**, *36*, 3455.
18. Baladron, C.; Alonso, J. A. *Phys. B* **1988**, *154*, 73.
19. Janssens, E.; Neukermans, S.; Lievens, P. *Curr. Opin. Solid State Mater. Sci.* **2004**, *8*, 185.
20. Omoda, T.; Takano, S.; Tsukuda, T. *Small* **2020**, e2001439.
21. Fei, W.; Antonello, S.; Dainese, T.; Dolmella, A.; Lahtinen, M.; Rissanen, K.; Venzo, A.; Maran, F. *J. Am. Chem. Soc.* **2019**, *141*, 16033.

22. Takano, S.; Ito, S.; Tsukuda, T. *J. Am. Chem. Soc.* **2019**, *141*, 15994.
23. Suyama, M.; Takano, S.; Tsukuda, T. *J. Phys. Chem. C* **2020**, *124*, 23923.
24. Hirai, H.; Takano, S.; Nakamura, T.; Tsukuda, T. *Inorg. Chem.* **2020**, *59*, 17889.
25. Negishi, Y.; Kurashige, W.; Niihori, Y.; Iwasa, T.; Nobusada, K. *Phys. Chem. Chem. Phys.* **2010**, *12*, 6219.
26. Qian, H.; Jiang, D. E.; Li, G.; Gayathri, C.; Das, A.; Gil, R. R.; Jin, R. *J. Am. Chem. Soc.* **2012**, *134*, 16159.
27. Tofanelli, M. A.; Ni, T. W.; Phillips, B. D.; Ackerson, C. J. *Inorg. Chem.* **2016**, *55*, 999.
28. Tian, S.; Liao, L.; Yuan, J.; Yao, C.; Chen, J.; Yang, J.; Wu, Z. *Chem. Commun.* **2016**, *52*, 9873.
29. Hossain, S.; Imai, Y.; Suzuki, D.; Choi, W.; Chen, Z.; Suzuki, T.; Yoshioka, M.; Kawawaki, T.; Lee, D.; Negishi, Y. *Nanoscale* **2019**, *11*, 22089.
30. Guo, R.; Murray, R. W. *J. Am. Chem. Soc.* **2005**, *127*, 12140.
31. Parker, J. F.; Kacprzak, K. A.; Lopez-Acevedo, O.; Häkkinen, H.; Murray, R. W. *J. Phys. Chem. C* **2010**, *114*, 8276.
32. Mooney, J.; Kambhampati, P. *J. Phys. Chem. Lett.* **2013**, *4*, 3316.
33. Das, A.; Li, T.; Nobusada, K.; Zeng, C.; Rosi, N. L.; Jin, R. *J. Am. Chem. Soc.* **2013**, *135*, 18264.
34. Wu, Z.; Suhan, J.; Jin, R. *J. Mater. Chem.* **2009**, *19*, 622.
35. Sheldrick, G. M. *Acta Crystallogr. C* **2015**, *71*, 3.
36. van der Sluis, P.; Spek, A. L. *Acta Crystallogr. A* **1990**, *46*, 194.
37. Spek, A. L. *J. Appl. Crystallogr.* **2003**, *36*, 7.
38. Chen, Y.; Liu, C.; Tang, Q.; Zeng, C.; Higaki, T.; Das, A.; Jiang, D. E.; Rosi, N. L.; Jin, R. *J. Am. Chem. Soc.* **2016**, *138*, 1482.
39. Dong, H.; Liao, L.; Wu, Z. *J. Phys. Chem. Lett.* **2017**, *8*, 5338.
40. Dong, H.; Liao, L.; Zhuang, S.; Yao, C.; Chen, J.; Tian, S.; Zhu, M.; Liu, X.; Li, L.; Wu, Z. *Nanoscale* **2017**, *9*, 3742.
41. Higaki, T.; Zeng, C.; Chen, Y.; Hussain, E.; Jin, R. *CrystEngComm* **2016**, *18*, 6979.
42. Walter, M.; Akola, J.; Lopez-Acevedo, O.; Jadzinsky, P. D.; Calero, G.; Ackerson, C. J.; Whetten, R. L.; Grönbeck, H.; Häkkinen, H. *Proc. Natl. Acad. Sci. U. S. A.* **2008**, *105*, 9157.
43. Zhu, M.; Aikens, C. M.; Hendrich, M. P.; Gupta, R.; Qian, H.; Schatz, G. C.; Jin, R. *J. Am. Chem. Soc.* **2009**, *131*, 2490.
44. Bondi, A. *J. Phys. Chem.* **1964**, *68*, 441.

Chapter 4.

Luminescence enhancement by introducing dendritic thiols

4.1. Introduction

Photoluminescence (PL) is a typical non-metallic property of ligand-protected Au superatoms.[1,2] Experimental and theoretical studies have shown that the origin of their PL is an electronic transition involving superatomic orbitals within Au core.[3-5] Ligand-protected Au superatoms have large molar absorption coefficient ($\varepsilon \sim 10^4$ $M^{-1}cm^{-1}$)[6] and their absorption can be tuned from ultraviolet (UV) to near infrared (NIR) region by controlling their size and shape as explained in Chapter 2.[7] These features are suitable for PL application. Additionally, recent reports have shown the unique PL properties of ligand-protected Au superatoms; dual emission due to structural distortion upon photoexcitation,[8] the switching of fluorescence/phosphorescence and the tuning of PL intensity by assemblying,[9,10] and PL enhancement through energy transfer from chromophores such as dansyl and pyrene groups in ligand layer.[11,12] For these characters, ligand-protected Au superatoms have a high potential for novel illuminant materials.

However, most ligand-protected Au superatoms show relatively low PL quantum yield (< 1 %).[1,2] This is probably because the photoexcited Au core undergoes fast non-radiative relaxation due to its fluxionality. X-ray absorption fine structure (XAFS) study reveals that Au–Au bonds on the surface of superatomic Au core is softer than those in bulk Au.[13,14] Density functional theory (DFT) calculations show that a large structural change occurs during the excitation from S_0 to S_1 state.[3,4] To overcome this situation, rigidification of Au core has been conducted by post synthetic modification of ligand layer. For example, the PL intensity of $Au_{22}(SR)_{18}$ is enhanced by suppressing the motion of ligands through ion-pairing with tetraalkylammonium cations or the host-guest interaction with cucurbiturils (CB[*n*]) (Figure 4.1).[15,16] However, for such modifications, the use of ligands having a high affinity toward modifiers is necessary. Without modifiers,

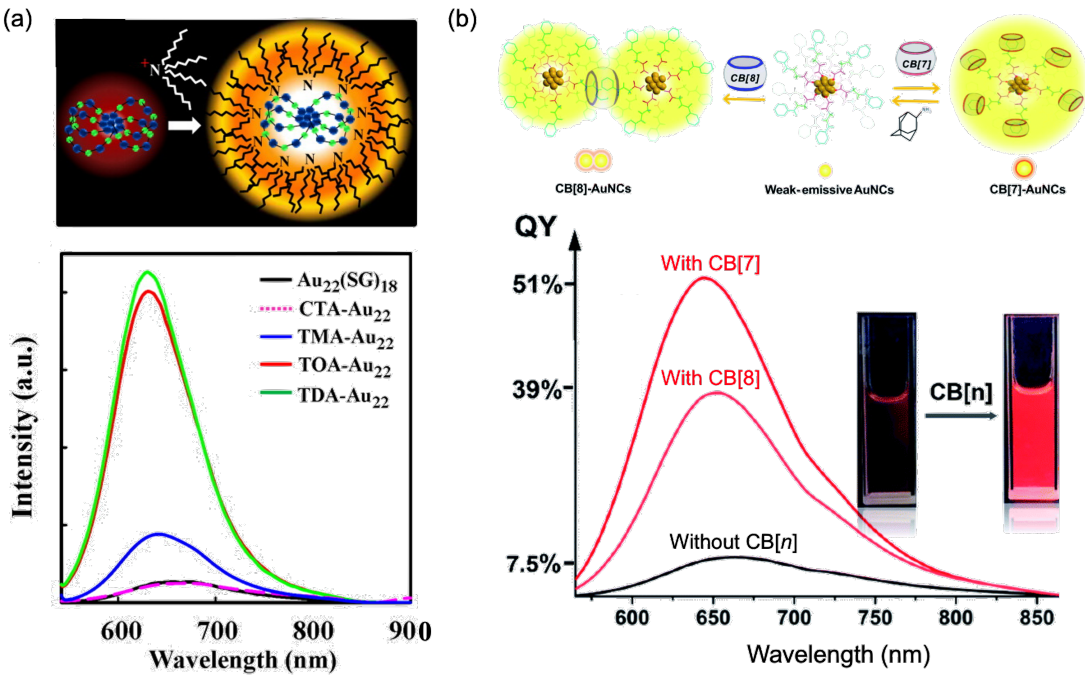

Figure 4.1. (a) PL spectra of $Au_{22}(SG)_{18}$ (GSH = glutathione) ion-paired with tetraalkylammonium cation. Rigidification of $Au_{22}(SG)_{18}$ by ion-paring is also schematically shown. CTA = cetyltrimethylammonium cation, TMA = tetramethylammonium cation, TOA = tetra-*n*-octylammonium cation, TDA = tetra-*n*-decylammonium cation. (b) PL spectra of $Au_{22}(FGGC)_{18}$ (FGGC = Phe–Gly–Gly–Cys peptide) associated with CB[*n*] (*n* = 7,8). Rigidification of $Au_{22}(FGGC)_{18}$ by the host-guest interaction with CB[*n*] is schematically shown. (a) Adapted with permission from ref. 15. Copyright 2015 American Chemical Society. (b) Adapted with permission from ref. 16. Copyright 2020 Royal Society of Chemistry.

it is known that attractive interaction between ligand side chains can rigidify the Au core. In *N*-heterocyclic carbene (NHC)-protected Au_{13} superatom $[Au_{13}(NHC)_9Cl_3]^{2+}$, the Au_{13} core is rigidified by CH–π and/or π–π interactions between adjacent NHC ligands and shows PL with a high quantum yield (16%).[17] It is expected that PL intensity is also enhanced by the introduction of interactive ligands through ligand-exchange reaction which is known as a versatile method to modify the ligand layer of thiolate-protected Au superatoms $Au_n(SR)_m$. Although the product is a mixture of partial exchanged cluster, we can introduce various thiolate ligands into any size of clusters under a mild condtion.[18-23]

Indeed, ligand exchange of $[Au_{24}(SMePh\textit{t}Bu)_{20}]^0$ (*t*BuPhMeSH = 4-*tert*-butylbenzyl mercaptan) with 11-mercaptoundecanoic acid (11-MUA) having a longer alkyl chain and protein thiol of bovine serum albumin (BSA) enhances its PL intensity by ~4 and ~5 times higher, respectively (Figure 4.2). This result is ascribed to that dispersive interaction and/or hydrogen bonding between exchanged ligands rigidify the Au core.[24] The further PL enhancement in $Au_n(SR)_m$ is expected by introducing designed interactive thiols.

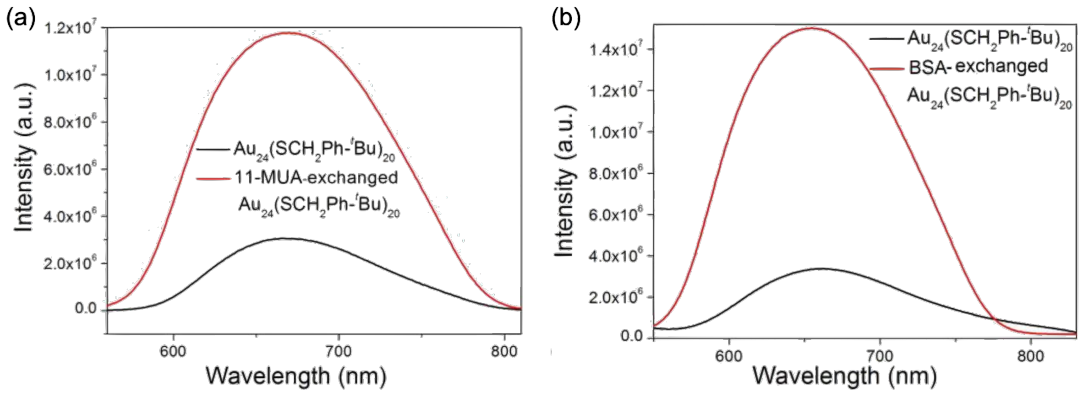

Figure 4.2. PL spectra of $[Au_{24}(SMePh\textit{t}Bu)_{20}]^0$ partially exchanged with (a) 11-MUA and (b) BSA. Adapted with permission from ref. 24. Copyright 2016 Wiley-VCH.

In this Chapter, I synthesized the Fréchet-type dendritic thiol (DenSH) having benzyloxy groups (Scheme 4.1)[25,26] with expecting the accumulation of CH–π and/or π–π interactions in ligand layer. DenSH with generation one and two ($Den^{G1}SH$ and $Den^{G2}SH$, Scheme 4.1) were introduced into $Au_n(SR)_m$ by ligand-exchange reaction. The target superatoms were $[Au_{25}(SEtPh)_{18}]^-$ (PhEtSH = 2-phenylethanethiol) and $[Au_{23}(ScHex)_{16}]^-$ (cHexSH = cyclohexanethiol) (Figure 4.3).[27–29] $[Au_{25}(SEtPh)_{18}]^-$ has an icosahedral (Ih) Au_{13} core protected by $Au_2(SEtPh)_3$ oligomers (Figure 4.3a)[27,28] and $[Au_{23}(ScHex)_{16}]^-$ has an anisotropic Au_{13} core protected by $Au_1(ScHex)_2$ and $Au_3(ScHex)_4$ oligomers (Figure4.3b).[29] An anisotropic shape of $[Au_{23}(ScHex)_{16}]^-$ would be more accessible by DenS ligands with large R group. I investigated how the PL

quantum yields (QYs) of $[Au_{25}(SEtPh)_{18}]^-$ and $[Au_{23}(ScHex)_{16}]^-$ (0.05% and 0.4 %, respectively)[5,30] are changed as functions of the numbers and generations of DenS ligands introduced.

Scheme 4.1. Structures of $Den^{G1}SH$ and $Den^{G2}SH$

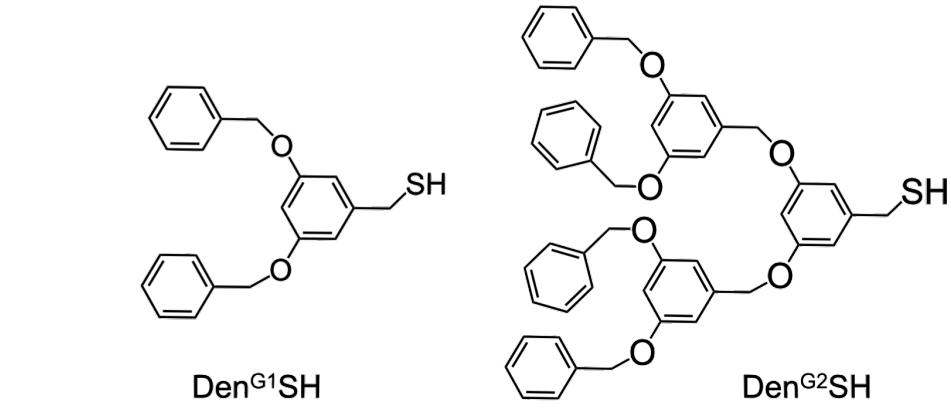

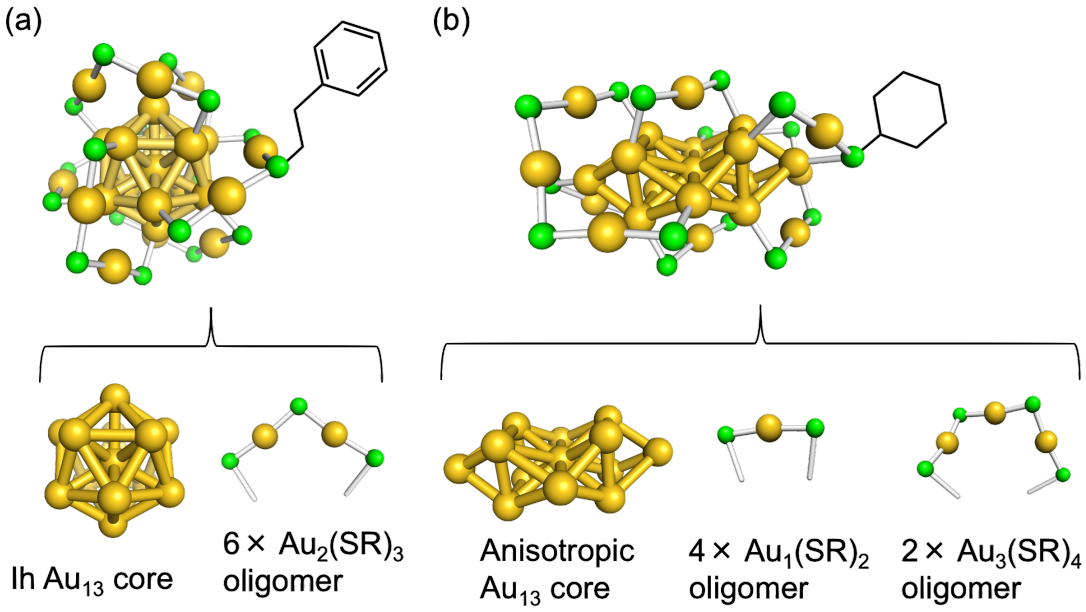

Figure 4.3. Anatomies of (a) $[Au_{25}(SEtPh)_{18}]^-$ and (b) $[Au_{23}(ScHex)_{16}]^-$.[27-29] The Au_{13} cores are highlighted by yellow bonds. Only one PhEt and cHex group is schematically shown for clarity. Color codes: yellow (Au); green (S).

4.2. Experiment

4.2.1. Chemicals

All chemicals were commercially available and used without further purification. Tetrachloroauric acid tetrahydrate ($HAuCl_4 \cdot 4H_2O$), sodium borohydride ($NaBH_4$), dichloromethane (DCM), methanol (MeOH), ethanol (EtOH), toluene, *n*-hexane, and Wakosil® 60 were purchased from FUJIFILM Wako Pure Chemical Corporation. 2-phenylethanethiol (PhEtSH), cyclohexanthiol (cHexSH), 3,5-dibenzyloxybenzyl bromide ($Den^{G1}Br$), 3,5-bis[3,5-bis(benzyloxy)benzyloxy]benzyl bromide ($Den^{G2}Br$), potassium hydroxide (KOH), 12 M hydrochloric acid (HCl*aq*), and thiourea were purchased from Tokyo Chemical Industry. Tetrahydrofuran (THF), chloroform-d_1 ($CDCl_3$), and dichloromethane-d_2 (CD_2Cl_2) were obtained from Kanto Chemical. Tetra-*n*-octylammonium bromide (TOABr) and acetonitrile (MeCN) was obtained from Sigma-Aldrich. Water was Milli-Q grade (ρ > 18 MΩ·cm).

4.2.2. General

^1H (400 MHz) and $^{13}C\{^1H\}$ (100 MHz) nuclear magnetic resonance (NMR) spectra were measured by a JEOL JNM-ECS400 spectrometer. The chemical shifts of NMR charts were calibrated by the residual proton signal of the solvent: ^1H NMR spectra were referenced to the signals of $CDCl_3$ at 7.26 ppm and of CD_2Cl_2 at 5.32 ppm and ^{13}C NMR spectra were referenced to the signals of $CDCl_3$ at 77.16 ppm and of CD_2Cl_2 at 53.84 ppm.[31] Ultraviolet-visible (UV-vis) absorption spectra were measured by JASCO V-630 and V-670 spectrophotometers. PL spectra were measured by HORIBA Fluorolog-NIR spectrophotometer at room temperature. PL of $[Au_{25}(SR)_{18}]^-$ excited at 1.81 eV (685 nm) was detected by an InGaAs solid-state detector cooled by liquid N_2. A photomultiplier

tube was used to detect the PL of $[Au_{23}(SR)_{16}]^-$ excited at 2.16 eV (575 nm). The absorbance of all the samples were ~0.1 at the excitation wavelength. The raw spectral data of absorption and PL as functions of the wavelength could be converted to the energy-dependent data according to the procedure reported.[32] Electrospray ionization (ESI) mass spectra were measured with using a JEOL JMS-T100LP AccuTOF mass spectrometer. $[Au_{23}(SR)_{16}]^-$ and $[Au_{25}(SR)_{18}]^-$ clusters were dispersed in DCM/MeCN = 1:1 (v/v) at a concentration of 0.5–1 mg/mL. The mixed dispersion was electrosprayed in a negative-ion mode. The temperatures of a desolvation chamber and an orifice were 120 and 80 °C, respectively. The mass spectra were calibrated by those of $[Au_{25}(S\text{-}n\text{-}C_3H_8)_{18}]^-$, $[Au_{25}(S\text{-}n\text{-}C_6H_{13})_{18}]^-$, and $[Au_{25}(S\text{-}n\text{-}C_{12}H_{25})_{18}]^-$ as external standards. The average x values x_{ave} in $[Au_{25}(SEtPh)_{18-x}(SDen)_x]^-$ and $[Au_{23}(ScHex)_{16-x}(SDen)_x]^-$ were calculated as follows:

$$x_{\text{ave}} = \frac{\sum_{i=0}^{n} nI_n}{\sum_{i=0}^{n} I_n} \tag{4.1}$$

where n = 18 and 16 for $[Au_{25}(SEtPh)_{18-x}(SDen)_x]^-$ and $[Au_{23}(ScHex)_{16-x}(SDen)_x]^-$, respectively. I_x is the peak area of peaks of $[Au_{25}(SEtPh)_{18-x}(SDen)_x]^-$ or $[Au_{23}(ScHex)_{16-x}(SDen)_x]^-$.

4.2.3. Synthesis

4.2.3.1. Den^{G1}SH

Den^{G1}SH was synthesized according to the published procedure with modification.[26] Den^{G1}Br (1 mmol) and thiourea (1 mmol) were mixed in 5 mL of EtOH/THF = 1:1 (v/v). The mixed solution was stirred for 4 h at 80 ºC with connecting a balloon filled with Ar gas. Then, 1 M KOH*aq* (2 mL) was added to the reaction solution using a syringe. After further stirred for 4 h at 80 ºC, the solution was cooled to r.t. followed by the addition of

1 M HCl*aq* (4 mL) using a syringe and stirred for a few minutes. The obtained white suspension was transferred to a round-bottomed flask with DCM and evaporated to remove a volatile. A crude product was extracted from the aqueous solution with DCM three times and the extract was evaporated. Thus obtained oil was purified by SiO_2 column chromatography (Wakosil® 60). The oil was firstly dissolved in a minimum amount of DCM and loaded onto SiO_2 column packed with DCM. The product was eluted with ~3 column volume of DCM. DCM solvent used for column chromatography was bubbled with Ar gas prior to the experiment. The eluted product was evaporated and dried in vacuo. Storage of thus obtained oil at –20 ºC gave a white solid of title compound. Evaporation of the oil with *n*-hexane helped to give a solid. Yield: 91 %. ^{1}H NMR (400 MHz, $CDCl_3$): δ 7.45-7.32 (m, 10H), 6.60 (d, J = 2.3 Hz, 2H), 6.52 (t, J = 2.3 Hz, 1H), 5.04 (s, 4H), 3.68 (d, J = 7.8 Hz, 2H), 1.78 (t, J = 7.6 Hz, 1H). ^{13}C{^{1}H} NMR (100 MHz, $CDCl_3$): δ 160.2, 143.6, 136.9, 128.7, 128.2, 127.7, 107.4, 100.9, 70.2, 29.3. Anal. Calcd. for $C_{21}H_{20}O_2S$: C, 74.97; H, 5.99; N, 0.00; S, 9.53. Found: C, 74.89; H, 6.00; N, 0.00; S, 9.37.

4.2.3.2. Den^{G2}SH

Den^{G2}SH was synthesized according to the published procedure with modification.[26] Den^{G2}Br (1 mmol) and thiourea (1 mmol) were mixed in 5 mL of EtOH/THF = 1:1 (v/v). The mixture was stirred for 4 h at 80 ºC with connecting a balloon filled with Ar gas. Then, 1 M KOH*aq* (2 mL) was added to the reaction solution using a syringe. After further stirred for 4 h at 80 ºC, the solution was cooled to r.t. followed by the addition of 1 M HCl*aq* (4 mL) using a syringe and stirred for a few minutes. The obtained white suspension and solid was transferred to a round-bottomed flask with DCM and

evaporated to remove a volatile. The formed solid was collected by centrifugation and subsequently washed with water two times and with MeOH three times. The white solid of title compound was dried in vacuo. Yield: 84 %. ^{1}H NMR (400 MHz, CD_2Cl_2): δ 7.44-7.31 (m, 20H), 6.69 (d, J = 1.8 Hz, 4H), 6.57 (dd, J = 2.5 Hz, 4H), 6.47 (t, J = 2.3 Hz, 1H), 5.05 (s, 8H), 4.98 (s, 4H), 3.68 (d, J = 7.8 Hz, 2H), 1.84 (t, J = 7.8 Hz, 1H). ^{13}C{^{1}H} NMR (100 MHz, CD_2Cl_2): δ 160.6, 160.4, 144.2, 139.9, 137.4, 128.9, 128.4, 128.0, 107.6, 106.8, 101.8, 101.0, 70.5, 70.3, 29.5. Anal. Calcd. for $C_{49}H_{44}O_6S$: C, 77.34; H, 5.82; N, 0.00; S, 4.21. Found: C, 77.37; H, 5.83; N, 0.00; S, 4.09.

4.2.3.3. $[Au_{25}(SEtPh)_{18}]^-$ and $[Au_{23}(ScHex)_{16}]^-$

$[Au_{25}(SEtPh)_{18}]^-$ and $[Au_{23}(ScHex)_{16}]^-$ were synthesized by the reported protocols.[29,33]

4.2.3.4. Ligand exchange of $[Au_{25}(SEtPh)_{18}]^-$ with DenSH

To the DCM solution of $[Au_{25}(SEtPh)_{18}]^-$ (1 mM, 1 mL), a given amount of $Den^{G1}SH$ or $Den^{G2}SH$ (5, 20, 50, and 100 equiv) was added. The mixed solution was stirred for 12 h at r.t. After that, MeOH was added to this solution and DCM was evaporated. The obtained suspension of MeOH was transferred to Eppendorf tubes. The tubes were filled with MeOH and centrifuged (14000 rpm) to precipitate ligand-exchanged products. $Den^{G1}S$-exchanged products were further washed with MeOH by centrifugation (14000 rpm) three times. $Den^{G2}S$-exchanged products were washed with MeOH (14000 rpm) twice and by centrifugal reprecipitation with DCM and *n*-hexane (14000 rpm). The number of washing and the ratio of DCM:*n*-hexane (v/v) were changed depending on the amount of $Den^{G2}SH$ firstly added: five times for 1:10 (5 equiv); three times for 1:10 and

then two times for 1:8 (20 equiv); six times for 1:5 (50 equiv); five times 1:5 and then three times for 1:4 (100 equiv). After the repeated extraction of washed products with MeCN, the solvent was evaporated and dried in vacuo. The ligand-exchanged products were obtained as a brown powder.

4.2.3.5. Ligand exchange of $[Au_{23}(ScHex)_{16}]^-$ with DenSH

To the DCM solution of $[Au_{23}(ScHex)_{16}]^-$ (1 mM, 1 mL), a given amount of $Den^{G1}SH$ or $Den^{G2}SH$ (5, 20, 50, and 100 equiv) was added. The mixed solution was stirred for 12 h at r.t. After that, MeOH was added to this solution and DCM was evaporated. The obtained suspension of MeOH was transferred to Eppendorf tubes. The tubes were filled with MeOH and centrifuged (14000 rpm) to precipitate ligand-exchanged products. $Den^{G1}S$-exchanged products were further washed with MeOH by centrifugation (14000 rpm) three times. $Den^{G2}S$-exchanged products were washed with MeOH (14000 rpm) three times and by centrifugal reprecipitation with DCM and *n*-hexane (14000 rpm). The number of washing and the ratio of DCM:*n*-hexane (v/v) were changed by the amount of $Den^{G2}SH$ firstly added: five times for 1:10 (5 equiv); five times for 1:8 (20 equiv); six times for 1:4 (50 equiv and 100 equiv). The washed precipitates were then dried in vacuo. The ligand-exchanged products were obtained as a purple powder.

4.3. Results and discussion

4.3.1. $Den^{G1}SH$ and $Den^{G2}SH$

$Den^{G1}SH$ and $Den^{G2}SH$ were synthesized from the corresponding bromides ($Den^{G1}Br$, $Den^{G2}Br$) and thiourea according to the previous report with modification.[26]

At first, the bromide salt of isothiouronium cation (R-SC$(NH_2)_2^+$) was prepared by the reaction of thiourea and Den^{G1}Br or Den^{G2}Br. It was then hydrolyzed by KOH and protonated by HCl to obtain Den^{G1}SH or Den^{G2}SH in a good yield (80–90 %). Figure 4.4 shows ^{1}H and ^{13}C{^{1}H} NMR charts of Den^{G1}SH in $CDCl_3$ and Den^{G2}SH in CD_2Cl_2. The peaks were clearly assigned to aryl (Ar-), -CH_2O-, -CH_2S-, and -SH groups in Den^{G1}SH and Den^{G2}SH and consistent with the previously reported result.[26]

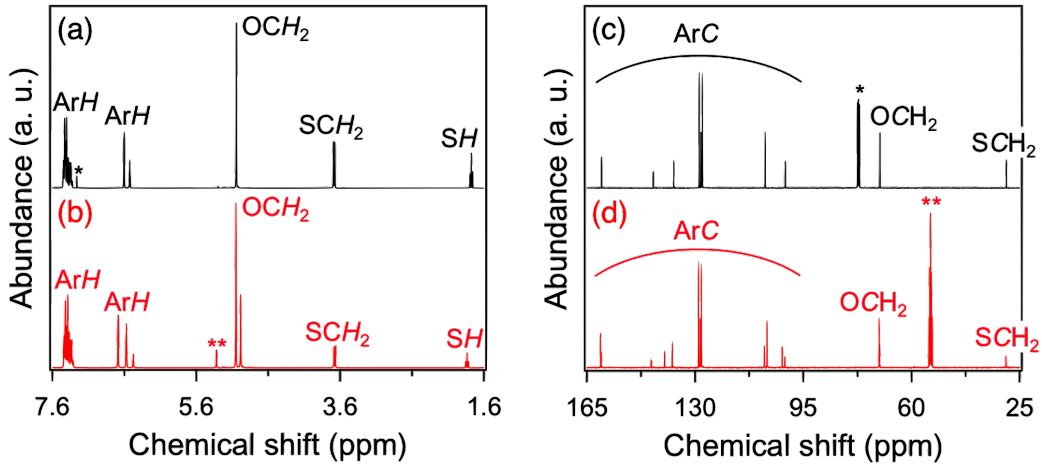

Figure 4.4. ^{1}H NMR charts of (a) Den^{G1}SH and (b) Den^{G2}SH. ^{13}C{^{1}H} NMR charts of (c) Den^{G1}SH and (d) Den^{G2}SH. The assignment of peaks is also shown. * and ** indicate the residual solvent peaks of $CDCl_3$ and CD_2Cl_2, respectively.

4.3.2. $[Au_{25}(SEtPh)_{18-x}(SDen)_x]^-$

4.3.2.1. Ligand exchange of $[Au_{25}(SEtPh)_{18}]^-$ with DenSH

Den^{G1}SH and Den^{G2}SH were introduced to $[Au_{25}(SEtPh)_{18}]^-$ through a ligand-exchange reaction. To the DCM solution of $[Au_{25}(SEtPh)_{18}]^-$, a given amount of Den^{G1}SH and Den^{G2}SH was added and the solution was stirred at r.t. Figure 4.5 shows ESI-mass spectra of $[Au_{25}(SEtPh)_{18-x}(SDen^{G1})_x]^-$ and $[Au_{25}(SEtPh)_{18-x}(SDen^{G2})_x]^-$ obtained. The gaps between the mass peaks in the progression (Δm = 198 in Figures 4.5a–d, Δm = 623 in Figures 4.5e–g) correspond to the mass difference between PhEtS and Den^{G1}S or

Den^{G1}S. The average number of Den^{G1}S or Den^{G2}S introduced (x_{ave}) was calculated by eq 4.1 and is presented in the inset of Figure 4.5. Overall, the x_{ave} value of Den^{G1}S was larger than that of Den^{G2}S when the same mol equivalence of the ligands was mixed. This trend is explained in terms of easier accessibility of smaller Den^{G1}SH to $[Au_{25}(SEtPh)_{18}]^-$ than larger Den^{G2}SH.

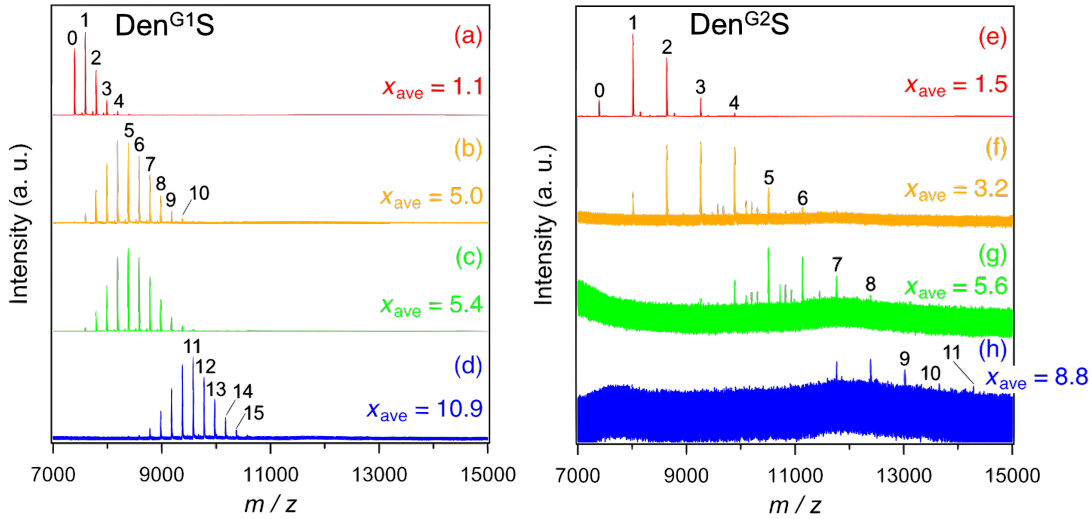

Figure 4.5. Negative-mode ESI mass spectra of $[Au_{25}(SEtPh)_{18}]^-$ exchanged with (a) 5 equiv, (b) 20 equiv, (c) 50 equiv, and (d) 100 equiv of Den^{G1}SH and (e) 5 equiv, (f) 20 equiv, (g) 50 equiv, and (h) 100 equiv of Den^{G2}SH. The number on each peak represents the x value. The inset shows the calculated x_{ave} value of each sample.

4.3.2.2. Optical property of $[Au_{25}(SEtPh)_{18-x}(SDen)_x]^-$

Figure 4.6 shows UV-vis absorption spectra of $[Au_{25}(SEtPh)_{18-x}(SDen^{G1})_x]^-$ and $[Au_{25}(SEtPh)_{18-x}(SDen^{G2})_x]^-$. Their spectral profiles especially for the first bands peaked at ~1.8 eV are similar to that of $[Au_{25}(SEtPh)_{18}]^-$. Appreciable change in the profile at higher energy region (> 2.5 eV) was ascribed to the difference of ligand side chains because of metal-to-ligand charge transfer (MLCT) nature of the electronic transition in this region as revealed by the previous calculation studies.[34-36]

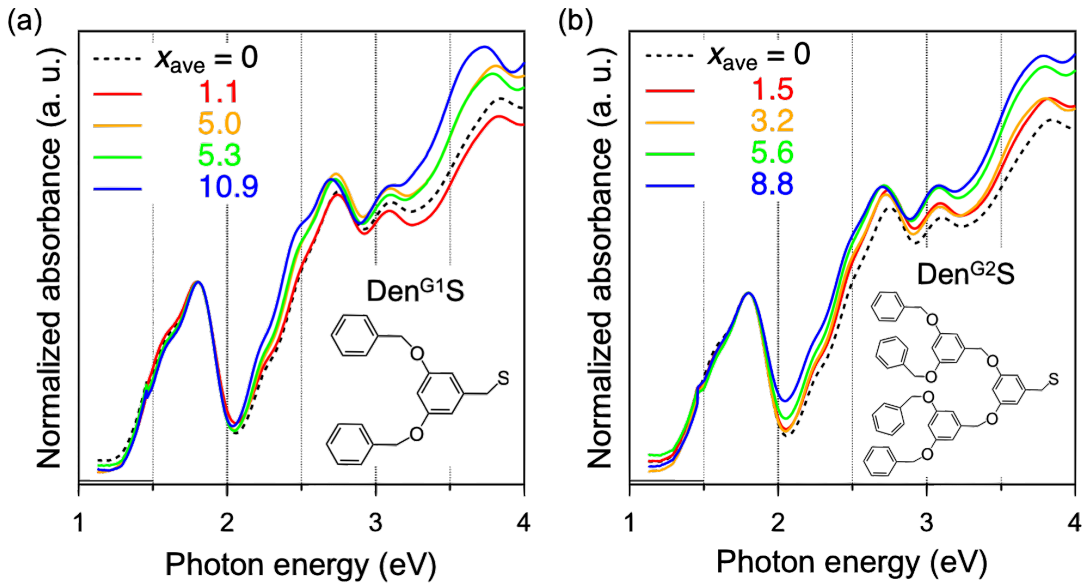

Figure 4.6. UV-vis absorption spectra of (a) $[Au_{25}(SEtPh)_{18-x}(SDen^{G1})_x]^-$ and (b) $[Au_{25}(SEtPh)_{18-x}(SDen^{G2})_x]^-$. The spectra are normalized by the absorbance at 1.81 eV. Inset shows the x_{ave} value of each spectrum. The structures of Den^{G1}S and Den^{G2}S ligands are shown in the inset.

Figure 4.7 shows the emission, excitation, and absorption spectra of $[Au_{25}(SEtPh)_{18}]^-$, $[Au_{25}(SEtPh)_{7.1}(SDen^{G1})_{10.9}]^-$, and $[Au_{25}(SEtPh)_{9.2}(SDen^{G2})_{8.8}]^-$. The emission spectra of $[Au_{25}(SEtPh)_{18}]^-$, $[Au_{25}(SEtPh)_{7.1}(SDen^{G1})_{10.9}]^-$, and $[Au_{25}(SEtPh)_{9.2}(SDen^{G2})_{8.8}]^-$ exhibit peaks at 1.16, 1.17, and 1.17 eV, respectively, resulting in the comparable Stokes shifts (0.66, 0.65, and 0.65 eV, respectively). These results indicate that the electronic structures are not affected appreciably by the introduction of Den^{G1}S and Den^{G2}S. On the other hand, the PL intensity was enhanced by introducing both Den^{G1}S and Den^{G2}S ligands. This result is ascribed to the suppression of the non-radiative decay processes by the rigidification of the Ih Au_{13} core via CH–π and/or π–π interactions between DenS ligands. The enhancement factor of PL in $[Au_{25}(SEtPh)_{9.2}(SDen^{G2})_{8.8}]^-$ was smaller than that in $[Au_{25}(SEtPh)_{7.1}(SDen^{G1})_{10.9}]^-$ although the calculated total number of benzyloxy groups in the former (61.6) was larger

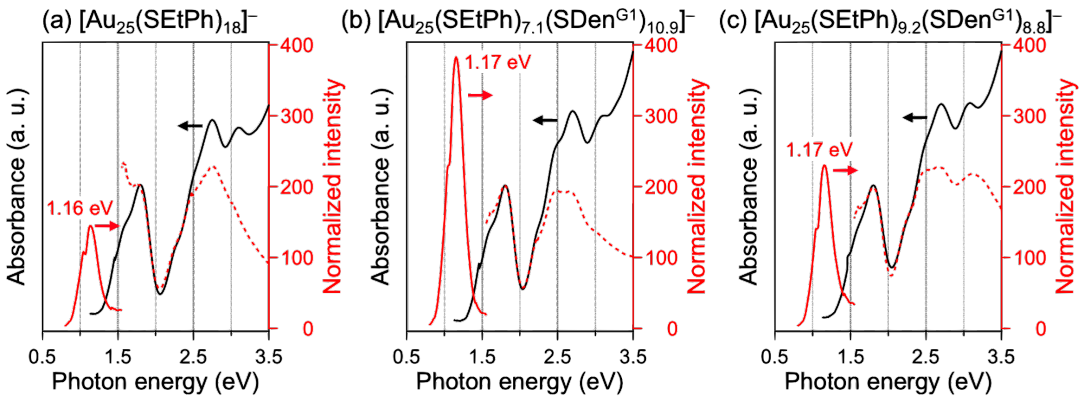

Figure 4.7. Optical spectra of (a) $[Au_{25}(SEtPh)_{18}]^-$, (b) $[Au_{25}(SEtPh)_{7.1}(SDen^{G1})_{10.9}]^-$, and (c) $[Au_{25}(SEtPh)_{9.2}(SDen^{G2})_{8.8}]^-$ measured in DCM. The black solid, red solid, and red dashed lines represent the absorption, PL, and excitation spectra, respectively. The peak energy of PL is also shown in the inset. The PL and absorption spectra are normalized by the absorbance at 1.81 eV. Excitation spectra are shown with arbitrary normalization.

than that in the latter (32.7). This phenomenon suggests that the benzyloxy groups located at outer region do not play an important role in the decay dynamics of the electronically excited state of $[Au_{25}(SEtPh)_{18-x}(SDen)_x]^-$.

The PL properties of $[Au_{25}(SEtPh)_{18-x}(SDen)_x]^-$ were investigated in more detail as a function of x_{ave}. Figures 4.8a and b show the PL spectra of $[Au_{25}(SEtPh)_{18-x}(SDen^{G1})_x]^-$ and $[Au_{25}(SEtPh)_{18-x}(SDen^{G2})_x]^-$ dissolved in DCM. Relative PL intensity is plotted against x_{ave} in Figures 4.8c. Table 4.1. summarizes the peak energy of the lowest-energy absorption bands (E_{abs}) and of the PL bands (E_{emi}) and the Stokes shift ($E_{abs} - E_{emi}$) in $[Au_{25}(SEtPh)_{18}]^-$ and $[Au_{25}(SEtPh)_{18-x}(SDen)_x]^-$. The E_{abs}, E_{emi}, and Stokes shifts of DenS-exchanged products remain similar to those of the unexchanged $[Au_{25}(SEtPh)_{18}]^-$, indicating that the small effect of DenS ligands on the electronic structure of $[Au_{25}(SEtPh)_{18}]^-$. In contrast, the PL intensity of $[Au_{25}(SEtPh)_{18-x}(SDen^{G1})_x]^-$ was enhanced with the increase of x_{ave}. Especially, the PL intensity of $[Au_{25}(SEtPh)_{7.1}(SDen^{G1})_{10.9}]^-$ was more intense by 2.7 times than that of the unexchanged

$[Au_{25}(SEtPh)_{18}]^-$ although the PLQY calculated with reference to $[Au_{25}(SEtPh)_{18}]^-$ was only 0.13 %.[30] On the other hand, the PL intensity of $[Au_{25}(SEtPh)_{18-x}(SDen^{G2})_x]^-$ was saturated at $x_{ave} \sim 3$. The origin of this behavior is not clear at this moment. In summary, I found that DenS ligands with smaller generation enhanced the PL of an isotropic $[Au_{25}(SEtPh)_{18}]^-$ more than those with larger generation.

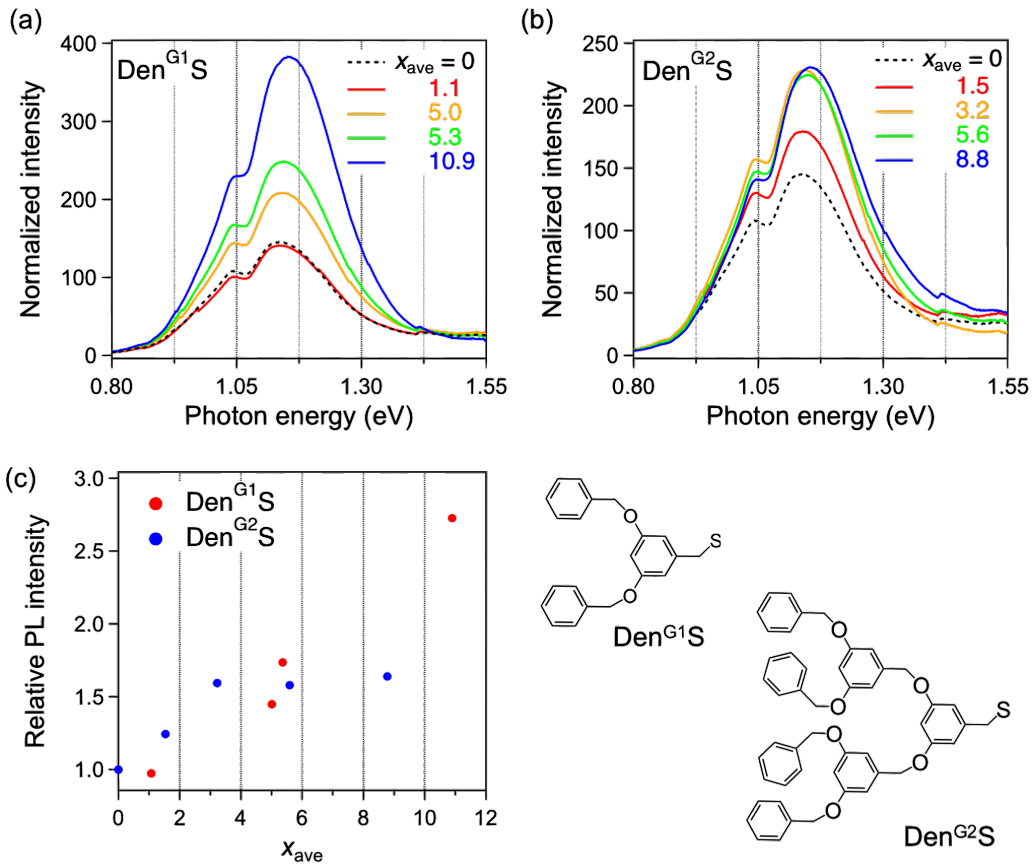

Figure 4.8. PL spectra of (a) $[Au_{25}(SEtPh)_{18-x}(SDen^{G1})_x]^-$ and (b) $[Au_{25}(SEtPh)_{18-x}(SDen^{G2})_x]^-$ with different number of x_{ave} measured in DCM. The PL spectra are normalized by the absorbance at 1.81 eV. (c) Plots of relative PL intensity against x_{ave}. The structures of $Den^{G1}S$ and $Den^{G2}S$ ligands are also shown.

Table 4.1. E_{abs}, E_{emi}, and Stokes shifts of $[Au_{25}(SEtPh)_{18}]^-$ and $[Au_{25}(SEtPh)_{18-x}(SDen)_x]^-$.

Sample	x_{ave}	E_{abs} (eV)	E_{emi} (eV)	Stokes shift (eV)
$[Au_{25}(SEtPh)_{18}]^-$	0	1.82	1.16	0.66
$[Au_{25}(SEtPh)_{18-x}(SDen^{G1})_x]^-$	1.1	1.82	1.16	0.67
	5.0	1.82	1.16	0.66
	5.3	1.82	1.16	0.66
	10.9	1.82	1.17	0.65
$[Au_{25}(SEtPh)_{18-x}(SDen^{G2})_x]^-$	1.5	1.82	1.16	0.67
	3.2	1.82	1.16	0.66
	5.6	1.82	1.16	0.66
	8.8	1.82	1.17	0.65

4.3.3. $[Au_{23}(ScHex)_{16-x}(SDen)_x]^-$

4.3.3.1. Ligand exchange of $[Au_{23}(ScHex)_{16}]^-$ with DenSH

$Den^{G1}SH$ or $Den^{G2}SH$ were also introduced into $[Au_{23}(ScHex)_{16}]^-$ with an anisotropic Au_{13} core.[29] Figure 4.9 shows the typical ESI mass spectra of ligand-exchange products of $[Au_{23}(ScHex)_{16}]^-$ with $Den^{G1}SH$ or $Den^{G2}SH$. The progression of mass peaks assignable to $[Au_{23}(ScHex)_{16-x}(SDen)_x]^-$ is observed. The x_{ave} values calculated by eq 4.1 are shown in the inset of Figure 4.9. Overall, the x_{ave} values of $[Au_{23}(ScHex)_{16-x}(SDen)_x]^-$ are larger than those of $[Au_{25}(SEtPh)_{18-x}(SDen)_x]^-$ prepared at the same mixing ratios of the clusters and DenSH (Figure 4.5). This tendency suggests that DenS ligands can access more easily to an anisotropic $[Au_{23}(ScHex)_{16}]^-$ than to an isotropic $[Au_{25}(SEtPh)_{18}]^-$.[27-29] Counterintuitively, the x_{ave} values of $[Au_{23}(ScHex)_{16-x}(SDen^{G2})_x]^-$ are larger than those of $[Au_{23}(ScHex)_{16-x}(SDen^{G1})_x]^-$ (Figure 4.9). This result suggests that $[Au_{23}(ScHex)_{16}]^-$ protected by bulky secondary thiolate of cHexS prefers larger $Den^{G2}S$ ligands to smaller $Den^{G1}S$. Figures 4.9b–d also show that the distribution of mass peaks is asymmetrical and has a maximum at $x \sim 8$. In $[Au_{23}(ScHex)_{16}]^-$, its anisotropic Au_{13} core is protected by

two different Au-ScHex oligomers: four oligomers of $Au_1(ScHex)_2$ and two oligomers of $Au_3(ScHex)_4$ (Figure 4.3b).[29] Given that the total numbers of cHexS in both oligomers are 8, the asymmetric distribution of the mass peaks in Figures 4.9b–d implies that the accessibility of $Den^{G1}S$ ligands is different between $Au_1(ScHex)_2$ and $Au_3(ScHex)_4$; longer $Au_3(ScHex)_4$ may be flexible and be replaced by $Den^{G1}S$ ligands more preferentially.

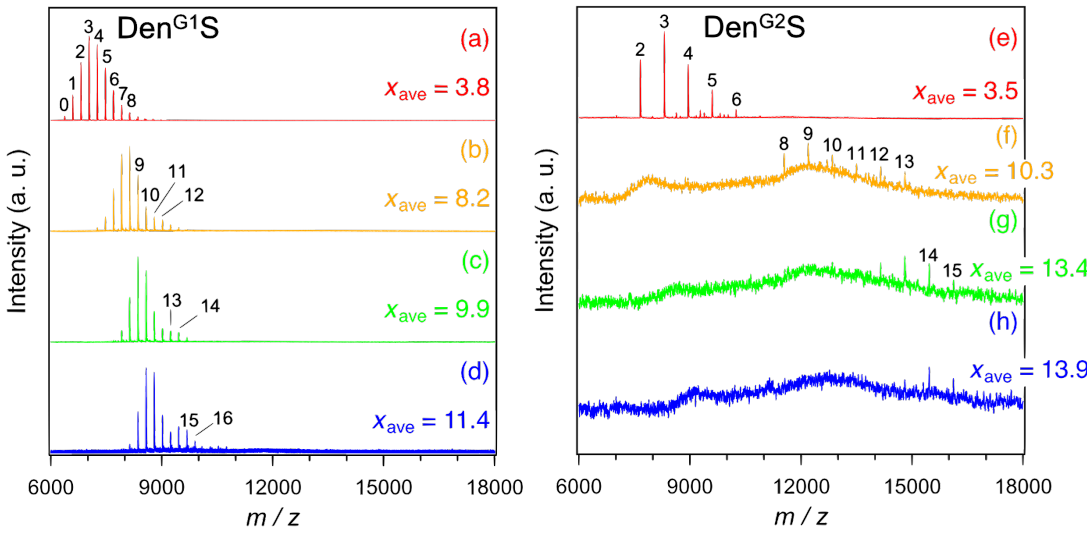

Figure 4.9. Negative-mode ESI mass spectra of $[Au_{23}(ScHex)_{16}]^-$ exchanged with (a) 5 equiv, (b) 20 equiv, (c) 50 equiv, and (d) 100 equiv of $Den^{G1}SH$ and (e) 5 equiv, (f) 20 equiv, (g) 50 equiv, and (h) 100 equiv of $Den^{G2}SH$. The spectra in (e-h) are smoothed by using binominal algorithm built in Igor Pro v7. 08 with smoothing parameter = 10 and Bounce end effect. The number on each peak represents the x value. The inset shows the calculated x_{ave} value of each sample.

4.3.3.2. Optical property of $[Au_{23}(ScHex)_{16-x}(SDen)_x]^-$

Figure 4.10 shows UV-vis absorption spectra of $[Au_{23}(ScHex)_{16-x}(SDen^{G1})_x]^-$ and $[Au_{23}(ScHex)_{16-x}(SDen^{G2})_x]^-$. The overall profiles of $[Au_{23}(ScHex)_{16-x}(SDen^{G1})_x]^-$ and $[Au_{23}(ScHex)_{16-x}(SDen^{G2})_x]^-$ are similar to that of $[Au_{23}(ScHex)_{16}]^-$ although the relative

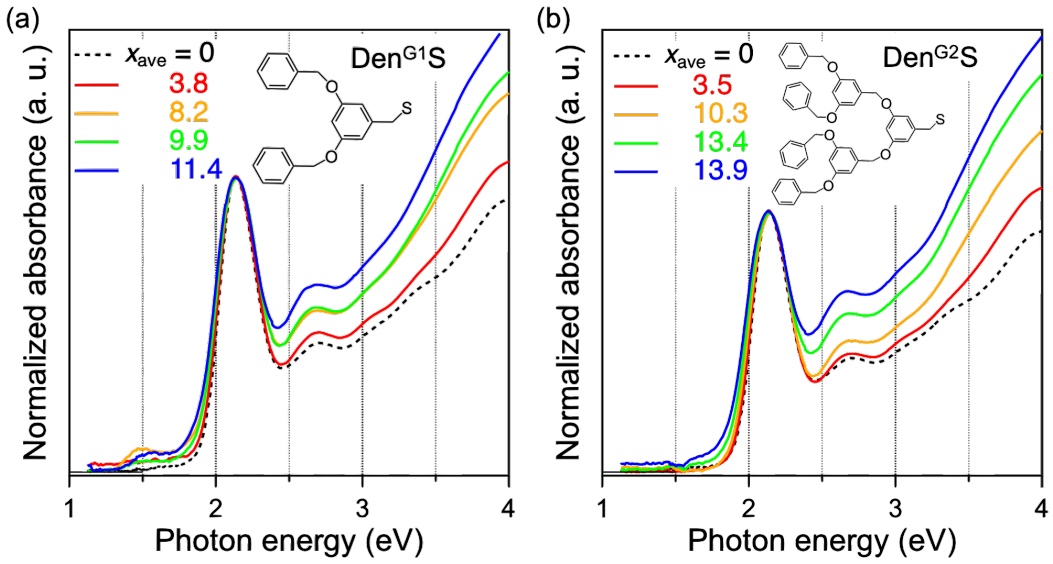

Figure 4.10. UV-vis absorption spectra of (a) $[Au_{23}(ScHex)_{16-x}(SDen^{G1})_x]^-$ and (b) $[Au_{25}(ScHex)_{16-x}(SDen^{G2})_x]^-$. The spectra are normalized by the absorbance at 2.16 eV. Inset shows the x_{ave} value of each spectrum. The structures of Den^{G1}S and Den^{G2}S ligands are shown in the inset.

intensity of high energy region with respect to the peak intensity at 2.1 eV monotonically increase with x_{ave}.

Figure 4.11 shows the emission, excitation and the absorption spectra of $[Au_{23}(ScHex)_{16}]^-$, $[Au_{23}(ScHex)_{4.6}(SDen^{G1})_{11.4}]^-$, and $[Au_{23}(ScHex)_{2.1}(SDen^{G2})_{13.9}]^-$. The emission spectra of $[Au_{23}(ScHex)_{16}]^-$ and $[Au_{23}(ScHex)_{2.1}(SDen^{G2})_{13.9}]^-$ exhibit a peak at the same energy (1.66 eV), whereas the emission peak of $[Au_{23}(ScHex)_{4.6}(SDen^{G1})_{11.4}]^-$ is red-shifted (1.61 eV). As a result, the Stokes shift of $[Au_{23}(ScHex)_{4.6}(SDen^{G1})_{11.4}]^-$ (0.56 eV) was larger than that of $[Au_{23}(ScHex)_{16}]^-$ (0.49 eV) and $[Au_{23}(ScHex)_{2.1}(SDen^{G2})_{13.9}]^-$ (0.50 eV). The excitation spectrum of $[Au_{23}(ScHex)_{4.6}(SDen^{G1})_{11.4}]^-$ is also different from that of $[Au_{23}(ScHex)_{16}]^-$ and $[Au_{23}(ScHex)_{2.1}(SDen^{G2})_{13.9}]^-$ and has a new peak at ~1.9 eV (Figure 4.11). These results are ascribed to that the electronic structure of an excited state of $[Au_{23}(ScHex)_{16}]^-$ is affected by Den^{G1}S ligands. On the other hand, PL intensity was enhanced by introducing

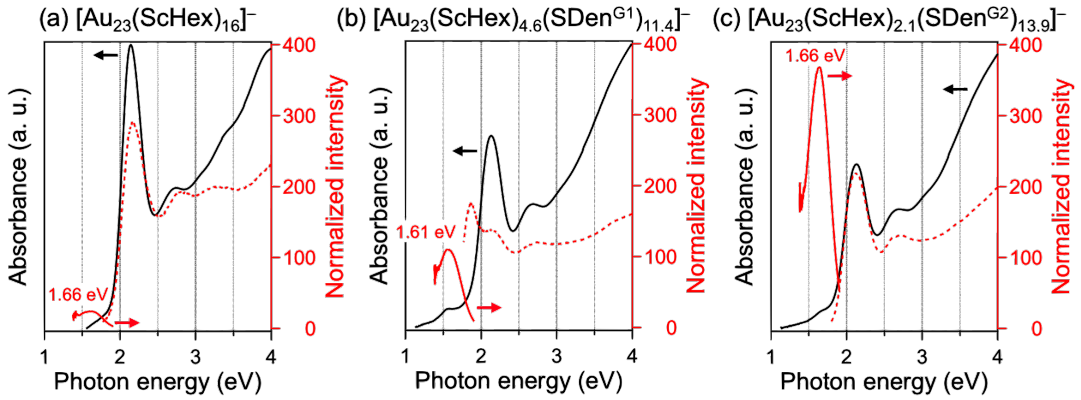

Figure 4.11. Optical spectra of (a) $[Au_{23}(ScHex)_{16}]^-$, (b) $[Au_{23}(ScHex)_{4.6}(SDen^{G1})_{11.4}]^-$, and (c) $[Au_{23}(ScHex)_{2.1}(SDen^{G2})_{13.9}]^-$ measured in DCM. The black solid, red solid, and red dashed lines represent the absorption, PL, and excitation spectra, respectively. The peak energy of PL is also shown in the inset. The PL and absorption spectra are normalized by the absorbance at 2.16 eV. Excitation spectra are shown with arbitrary normalization.

both $Den^{G1}S$ and $Den^{G2}S$ ligands. This result is ascribed to that non-radiative decay processes in the anisotropic Au_{13} core of $[Au_{23}(ScHex)_{16}]^-$ is also suppressed via CH–π and/or π–π interactions between DenS ligands. This time, the enhancement factor of PL in $[Au_{23}(ScHex)_{2.1}(SDen^{G2})_{13.9}]^-$ was larger than that in $[Au_{23}(ScHex)_{4.6}(SDen^{G1})_{11.4}]^-$ The benzyloxy groups located at outer region seemed to play an important role in the decay dynamics of the electronically excited state of $[Au_{23}(ScHex)_{16-x}(SDen)_x]^-$.

The PL properties of $[Au_{23}(ScHex)_{16-x}(SDen)_x]^-$ were investigated in more detail as a function of x_{ave}. Figures 4.12a and b show the PL spectra of $[Au_{23}(ScHex)_{16-x}(SDen^{G1})_x]^-$ and $[Au_{23}(ScHex)_{16-x}(SDen^{G2})_x]^-$ dissolved in DCM. Relative PL intensity is plotted against x_{ave} in Figure 4.12c. Table 4.2 summarizes the E_{abs}, E_{emi}, and Stokes shift in $[Au_{23}(ScHex)_{16}]^-$ and $[Au_{23}(ScHex)_{16-x}(SDen)_x]^-$. The E_{abs}, E_{emi}, and Stokes shifts of $[Au_{23}(ScHex)_{16-x}(SDen^{G2})_x]^-$ and of the unexchanged $[Au_{23}(ScHex)_{16}]^-$ are similar. However, the values of E_{emi} and Stokes shifts of $[Au_{23}(ScHex)_{16-x}(SDen^{G!})_x]^-$ appreciably differ from those of $[Au_{23}(ScHex)_{16}]^-$. This result indicates that $Den^{G1}S$ ligands modulate

the electronic structure of $[Au_{23}(ScHex)_{16}]^-$ while $Den^{G2}S$ ligands do not. In contrast, the PL intensity of both $[Au_{23}(ScHex)_{16-x}(SDen^{G1})_x]^-$ and $[Au_{23}(ScHex)_{16-x}(SDen^{G2})_x]^-$ was enhanced with the increase of x_{ave}. Especially, the PL intensity of $[Au_{23}(ScHex)_{16-x}(SDen^{G2})_x]^-$ was more intense by 15 times than that of the unexchanged $[Au_{23}(ScHex)_{16}]^-$ and the PLQY calculated with reference to $[Au_{23}(ScHex)_{16}]^-$ was 6 %.[5] In summary, I found that DenS ligands with larger generation enhanced the PL of an anisotropic $[Au_{25}(SEtPh)_{18}]^-$ more than those with smaller generation.

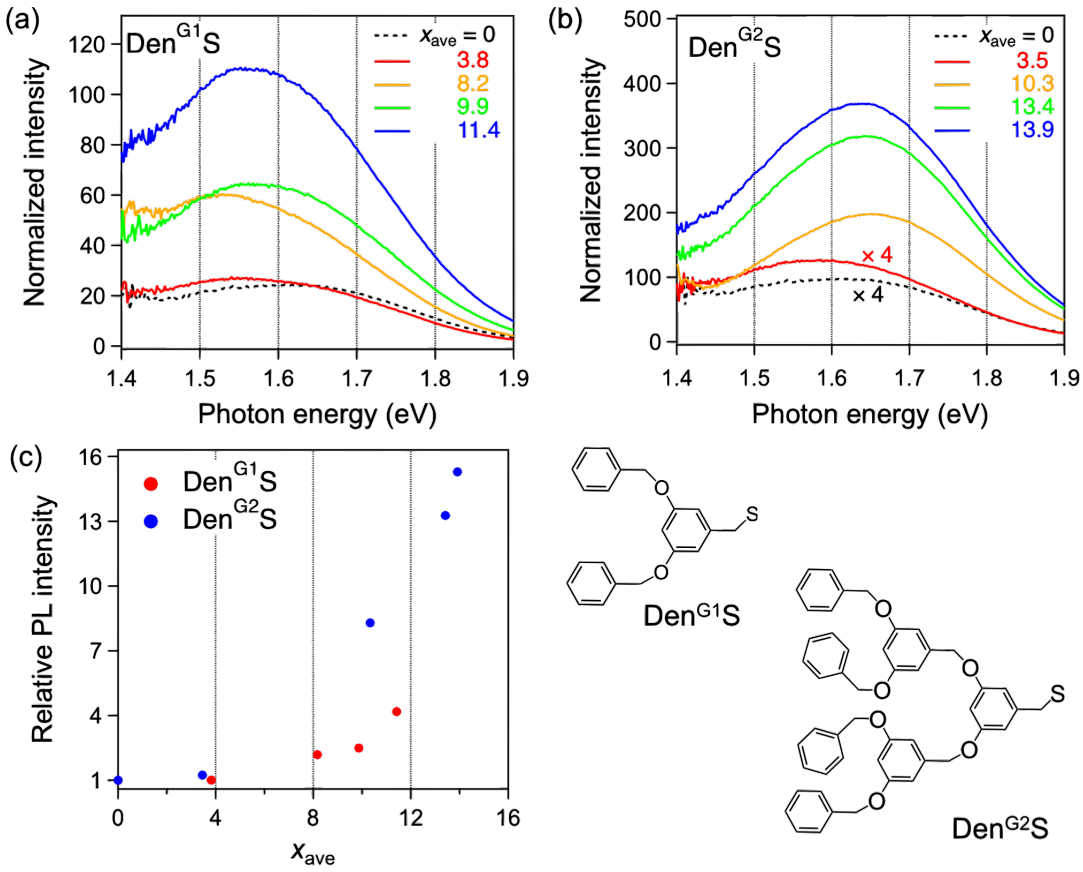

Figure 4.12. PL spectra of (a) $[Au_{23}(ScHex)_{16-x}(SDen^{G1})_x]^-$ and (b) $[Au_{23}(ScHex)_{16-x}(SDen^{G2})_x]^-$ with different number of x_{ave} measured in DCM. The PL spectra are normalized by the absorbance at 2.16 eV. (c) Plots of relative PL intensity against x_{ave}. The structures of $Den^{G1}S$ and $Den^{G2}S$ ligands are also shown.

Table 4.2. E_{abs}, E_{emi}, and Stokes shifts of $[Au_{23}(ScHex)_{16}]^-$ and $[Au_{23}(ScHex)_{16-x}(SDen)_x]^-$

Sample	x_{ave}	E_{abs} (eV)	E_{emi} (eV)	Stokes shift (eV)
$[Au_{23}(ScHex)_{16}]^-$	0	2.15	1.66	0.49
$[Au_{23}(ScHex)_{16-x}(SDen^{G1})_x]^-$	3.8	2.16	1.61	0.55
	8.2	2.17	1.58	0.59
	9.9	2.17	1.62	0.55
	11.4	2.17	1.61	0.56
$[Au_{23}(ScHex)_{16-x}(SDen^{G2})_x]^-$	3.5	2.15	1.63	0.53
	10.3	2.17	1.68	0.49
	13.4	2.17	1.67	0.50
	13.9	2.16	1.66	0.50

4.4. Summary

In summary, the Fréchet-type dendritic thiols with generation one and two ($Den^{G1}SH$, $Den^{G2}SH$) were introduced into thiolate-protected Au superatoms by ligand-exchange reaction. The target superatoms are $[Au_{25}(SEtPh)_{18}]^-$ with an isotropic Ih Au_{13} core and $[Au_{23}(ScHex)_{16}]^-$ with an anisotropic Au_{13} core. In both superatoms, PL intensity was enhanced by the introduction of DenS ligands. This result is ascribed to that non-radiative decay processes are suppressed by the rigidification of the Au cores via CH–π and/or π–π interactions between DenS ligands. Especially for $[Au_{23}(ScHex)_{16}]^-$, its PLQY was enhanced up to 15 times (0.4 $\rightarrow$ 6 %).[5] In the case of $[Au_{25}(SEtPh)_{18}]^-$ with an isotropic structure, the introduction of $Den^{G1}S$ more enhanced the PL intensity than $Den^{G2}S$. On the other hand, in an anisotropic $[Au_{23}(ScHex)_{16}]^-$, the PL enhancement in $Den^{G2}S$-exchanged product was larger than that in $Den^{G1}S$-exchanged products. Au superatoms with an anisotropic structure seemed to be able to accept DenS ligands with larger generation. In the next study, PL lifetime of DenS-exchanged products should be measured to study the rate of radiative and non-radiative processes. The core

rigidification by DenS ligands can be studied by measuring the temperature dependance of extended X-ray absorption fine structure (EXAFS) as previously reported.[13,14]

References

1. Cantelli, A.; Guidetti, G.; Manzi, J.; Caponetti, V.; Montalti, M. *Eur. J. Inorg. Chem.* **2017**, *2017*, 5068.
2. Kang, X.; Zhu, M. *Chem. Soc. Rev.* **2019**, *48*, 2422.
3. Weerawardene, K. L.; Aikens, C. M. *J. Am. Chem. Soc.* **2016**, *138*, 11202.
4. Weerawardene, K.; Pandeya, P.; Zhou, M.; Chen, Y.; Jin, R.; Aikens, C. M. *J. Am. Chem. Soc.* **2019**, *141*, 18715.
5. Li, Q.; Zhou, M.; So, W. Y.; Huang, J.; Li, M.; Kauffman, D. R.; Cotlet, M.; Higaki, T.; Peteanu, L. A.; Shao, Z.; Jin, R. *J. Am. Chem. Soc.* **2019**, *141*, 5314.
6. Negishi, Y.; Nobusada, K.; Tsukuda, T. *J. Am. Chem. Soc.* **2005**, *127*, 5261.
7. Omoda, T.; Takano, S.; Tsukuda, T. *Small* **2020**, e2001439.
8. Li, Q.; Zhou, D.; Chai, J.; So, W. Y.; Cai, T.; Li, M.; Peteanu, L. A.; Chen, O.; Cotlet, M.; Wendy Gu, X.; Zhu, H.; Jin, R. *Nat. Commun.* **2020**, *11*, 2897.
9. Sugiuchi, M.; Maeba, J.; Okubo, N.; Iwamura, M.; Nozaki, K.; Konishi, K. *J. Am. Chem. Soc.* **2017**, *139*, 17731.
10. Sugiuchi, M.; Zhang, M.; Hakoishi, Y.; Shichibu, Y.; Horimoto, N. N.; Yamauchi, Y.; Ishida, Y.; Konishi, K. *J. Phys. Chem. C* **2020**, *124*, 16209.
11. Muhammed, M. A. H.; Shaw, A. K.; Pal, S. K.; Pradeep, T. *J. Phys. Chem. C* **2008**, *112*, 14324.
12. Pyo, K.; Thanthirige, V. D.; Yoon, S. Y.; Ramakrishna, G.; Lee, D. *Nanoscale* **2016**, *8*, 20008.
13. Yamazoe, S.; Takano, S.; Kurashige, W.; Yokoyama, T.; Nitta, K.; Negishi, Y.; Tsukuda, T. *Nat. Commun.* **2016**, *7*, 10414.
14. Yamazoe, S.; Matsuo, S.; Muramatsu, S.; Takano, S.; Nitta, K.; Tsukuda, T. *Inorg. Chem.* **2017**, *56*, 8319.
15. Pyo, K.; Thanthirige, V. D.; Kwak, K.; Pandurangan, P.; Ramakrishna, G.; Lee, D. *J. Am. Chem. Soc.* **2015**, *137*, 8244.
16. Jiang, T.; Qu, G.; Wang, J.; Ma, X.; Tian, H. *Chem. Sci.* **2020,** *11*, 3531.
17. Narouz, M. R.; Takano, S.; Lummis, P. A.; Levchenko, T. I.; Nazemi, A.; Kaappa, S.; Malola, S.; Yousefalizadeh, G.; Calhoun, L. A.; Stamplecoskie, K. G.; Häkkinen, H.; Tsukuda, T.; Crudden, C. M. *J. Am. Chem. Soc.* **2019**, *141*, 14997.
18. Dass, A.; Stevenson, A.; Dubay, G. R.; Tracy, J. B.; Murray, R. W. *J. Am. Chem. Soc.* **2008**, *130*, 5940.
19. Dass, A.; Holt, K.; Parker, J. F.; Feldberg, S. W.; Murray, R. W. *J. Phys. Chem. C* **2008**, *112*, 20276.
20. Shibu, E. S.; Muhammed, M. A. H.; Tsukuda, T.; Pradeep, T. *J. Phys. Chem. C* **2008**,

112, 12168.
21. Fields-Zinna, C. A.; Parker, J. F.; Murray, R. W. *J. Am. Chem. Soc.* **2010**, *132*, 17193.
22. Heinecke, C. L.; Ni, T. W.; Malola, S.; Mäkinen, V.; Wong, O. A.; Häkkinen, H.; Ackerson, C. J. *J. Am. Chem. Soc.* **2012**, *134*, 13316.
23. Ni, T. W.; Tofanelli, M. A.; Phillips, B. D.; Ackerson, C. J. *Inorg. Chem.* **2014**, *53*, 6500.
24. Gan, Z.; Lin, Y.; Luo, L.; Han, G.; Liu, W.; Liu, Z.; Yao, C.; Weng, L.; Liao, L.; Chen, J.; Liu, X.; Luo, Y.; Wang, C.; Wei, S.; Wu, Z. *Angew. Chem., Int. Ed.* **2016**, *55*, 11567.
25. Hawker, C. J.; Fréchet, J. M. J. *J. Am. Chem. Soc.* **1990**, *112*, 7638.
26. Zhang, L.; Huo, F.; Wang, Z.; Wu, L.; Zhang, X.; Höppener, S.; Chi, L.; Fuchs, H.; Zhao, J.; Niu, L.; Dong, S. *Langmuir* **2000**, *16*, 3813.
27. Heaven, M. W.; Dass, A.; White, P. S.; Holt, K. M.; Murray, R. W. *J. Am. Chem. Soc.* **2008**, *130*, 3754.
28. Zhu, M.; Aikens, C. M.; Hollander, F. J.; Schatz, G. C.; Jin, R. *J. Am. Chem. Soc.* **2008**, *130*, 5883.
29. Das, A.; Li, T.; Nobusada, K.; Zeng, C.; Rosi, N. L.; Jin, R. *J. Am. Chem. Soc.* **2013**, *135*, 18264.
30. Suyama, M.; Takano, S.; Tsukuda, T. *J. Phys. Chem. C* **2020**, *124*, 23923.
31. Fulmer, G. R.; Miller, A. J. M.; Sherden, N. H.; Gottlieb, H. E.; Nudelman, A.; Stoltz, B. M.; Bercaw, J. E.; Goldberg, K. I. *Organometallics* **2010**, *29*, 2176.
32. Mooney, J.; Kambhampati, P. *J. Phys. Chem. Lett.* **2013**, *4*, 3316.
33. Tofanelli, M. A.; Salorinne, K.; Ni, T. W.; Malola, S.; Newell, B.; Phillips, B.; Häkkinen, H.; Ackerson, C. J. *Chem. Sci.* **2016**, *7*, 1882.
34. Aikens, C. M. *J. Phys. Chem. Lett.* **2010**, *1*, 2594.
35. Tlahuice-Flores, A.; Whetten, R. L.; Jose-Yacaman, M. *J. Phys. Chem. C* **2013**, *117*, 20867.
36. Baseggio, O.; De Vetta, M.; Fronzoni, G.; Toffoli, D.; Stener, M.; Sementa, L.; Fortunelli, A. *Int. J. Quantum Chem.* **2018**, *118*.

Chapter 5.

Concluding remarks

5.1. Summary

In order to study ligand effects on the redox and optical properties of thiolate (RS)-protected Au superatoms, I synthesized and characterized Au superatoms protected by two types of bulky RS ligands: *N*-2-(mercaptopropionyl)glycine (PGSH, Scheme 5.1a), cyclohexanethiol (cHexSH, Scheme 5.1b) having a secondary α-carbon and the Fréchet-type dendritic thiol (DenSH, Scheme 5.1c) with benzyloxy groups.

Scheme 5.1. Structures of (a) PGSH, (b) cHexSH, and (c) DenSH. The generation of DenSH is two.

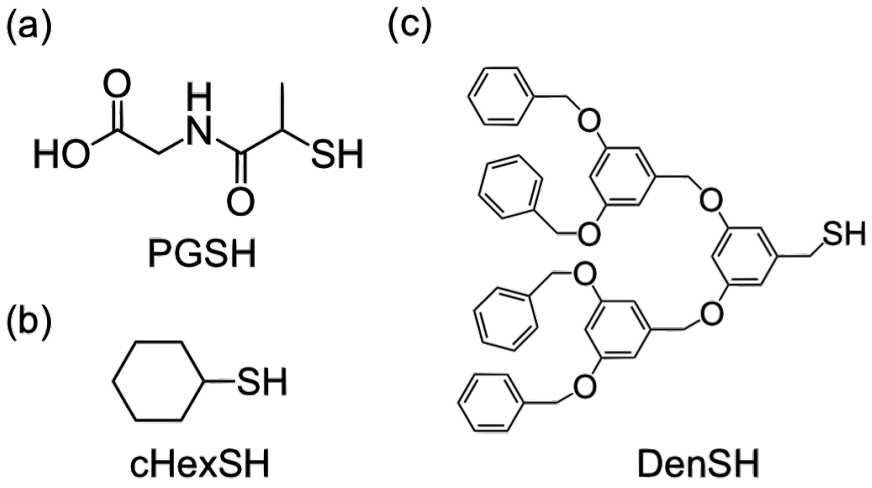

In chapter 2, I synthesized and characterized $[Au_{25}(SPG)_{18}]^-$. Ultraviolet-visible (UV-vis) absorption spectrum and extended X-ray absorption fine structure (EXAFS) oscillation of $[Au_{25}(SPG)_{18}]^-$ were different from those of conventional $[Au_{25}(SEtPh)_{18}]^-$ (PhEtSH = 2-phenylethanethiol) having an icosahedral (Ih) Au_{13} core with the superatomic electron configuration of $(1S)^2(1P)^6$. Instead, the results indicated that $[Au_{25}(SPG)_{18}]^-$ had an anisotropic Au_{13} core like that in $[Au_{23}(ScHex)_{16}]^-$. The optical highest occupied molecular orbital (HOMO)-lowest unoccupied molecular orbital (LUMO) gap (*HL*) of $[Au_{25}(SPG)_{18}]^-$ was 1.8 eV, larger than the *HL* of $[Au_{25}(SEtPh)_{18}]^-$ (1.3 eV). According to the density functional theory (DFT) calculations, widening of *HL*

in $[Au_{25}(SPG)_{18}]^-$ was ascribed to the reordering of the superatomic orbitals to form an electron configuration of $(1S)^2(1P)^4(1D)^2$ due to the anisotropic deformation of the Au_{13} core. The formation of such anisotropic Au core in $[Au_{25}(SPG)_{18}]^-$ was probably induced by non-covalent interactions between PGS ligands.

In Chapter 3, I synthesized $[Au_{25}(ScHex)_{18}]^0$ with an open electron configuration of $(1S)^2(1P)^5$ as a minor byproduct of $[Au_{23}(ScHex)_{16}]^-$. The results of single crystal X-ray diffraction analysis and UV-vis absorption spectroscopy showed that $[Au_{25}(ScHex)_{18}]^0$ had the same structural motif as conventional $[Au_{25}(SEtPh)_{18}]^0$, an oblately distorted Ih Au_{13} core by the Jahn-Teller effect. Conventional $[Au_{25}(SEtPh)_{18}]^0$ was easily reduced to $[Au_{25}(SEtPh)_{18}]^-$ to form a closed shell of $(1S)^2(1P)^6$ along with the transformation of its distorted Au_{13} core to the isotropic one. On the other hand, $[Au_{25}(ScHex)_{18}]^0$ had resistance to the reduction and preferred the neutral state. This result implied that the structural relaxation of the Jahn-Teller distorted Au_{13} core was inhibited by the steric hinderance of bulky cHexS ligands.

In chapter 4, I introduced DenSH into $[Au_{25}(SEtPh)_{18}]^-$ with an Ih Au_{13} core and $[Au_{23}(ScHex)_{16}]^-$ with an anisotropic Au_{13} core through ligand-exchange reaction. In both cases, exchanged products showed stronger photoluminescence (PL) than unexchanged $[Au_{25}(SEtPh)_{18}]^-$ and $[Au_{23}(ScHex)_{16}]^-$. The PL of $[Au_{25}(SEtPh)_{18-x}(SDen)_x]^-$ was more enhanced with shorter generation of DenS ligands, whereas the opposite trend was observed in the case of $[Au_{23}(ScHex)_{16-x}(SDen)_x]^-$. The PL enhancement by DenS ligands was ascribed to the suppression of non-radiative decay processes by the rigidification of the Au_{13} cores via CH–π and/or π–π interactions between benzyloxy groups of DenS ligands.

In conclusion, I demonstrated that the optical properties and chemical reduction

behavior of thiolate-protected Au superatoms are significantly affected by inter-ligand interactions (steric repulsion, hydrogen bonding, CH–π and/or π–π interaction…).

5.2. Future prospects

In this thesis, I found that the internal structure within Au superatom was sensitive to ligand layer. It is possible to tune the structures and associated properties of Au-based superatoms by ligands. The results in Chapters 2 and 3 suggest that by using bulky thiols with a secondary or tertiary α-carbon, an isotropic Ih core structure becomes unstable and an anisotropic and non-Ih structure tend to form. Indeed, Au superatoms with a variety of structures and packings have been hitherto synthesized by changing the bulkiness of ligands.[1-3] However, for the synthesis, commercially available ligands are just exhaustively used. The strategy to improve the properties of Au superatoms is still poor. Beyond these studies, we would give Au superatoms novel functions by designing ligands. One plausible function is a switching behavior responsible for external stimuli. By introducing photoisomerizable functional groups or redox-active metal complexes into ligand side chains, the reversible structural change of Au superatoms would be possible along with the change of ligand conformation upon photoexcitation or redox process (Figure 5.1a). It is expected that the redox and optical properties of Au superatoms also reversibly switch concomitantly. Several Au superatoms have been synthesized with using functionalized ligands by conventional bottom-up approach: azobenzene-thiolate-protected $Au_{25}(SR)_{18}$ and 1,1'-bis(diphenylphosphino)ferrocene (dppf)-protected Au_8 and Au_{11} superatoms.[4,5] In addition, it is also plausible to introduce the functional groups through post-synthetic ligand modification by organic reactions such as click reaction of strain-promoted alkyne-azide cycloaddition.[6,7]

Inter-ligand interactions used for the tuning of redox and PL properties in this thesis (steric repulsion, CH–π and/or π–π interactions) were relatively weak. For further modulation of these properties, it is necessary to introduce strong bonds between ligands. One plausible method is bridging between ligands by linker molecules through C–C bond formation reactions such as cross coupling reactions, Grignard reactions, and amide bond formations (Figure 5.1b). Upon bridging, ligand conformation is fixed by strong and stiff C–C bonds and thus the redox and PL properties would be modulated significantly. The introduction of circular dichroism (CD) in achiral Au superatoms by using chiral linkers is also expected. Because the degree of bridging is easily changed by the amount of linkers, we can quantitatively correlate the surface structure and properties of Au superatoms.

In Chapters 2 and 3, ligand bulkiness induced the structural distortion/deformation of Au superatoms. Besides, steric repulsion between bulky ligands can expose the surface of Au superatoms. For example, the previous report shows that with using the bulky arenethiol of 1,1,3,3,5,5,7,7-octaethyl-*s*-hydrindacene-4-thiol (EindSH), $Au_{41}(SEind)_{12}$ with a low coverage is synthesized.[8] It is expected that thus exposed surface is accessible by small molecules and acts as an active site for catalytic reactions (Figure 5.1c) as observed in polymer-stabilized Au superatoms.[9] Such ligand-protected Au superatom is an ideal model catalyst with defined size, composition, and structure. DenSH with larger generation is one of the promising ligands to synthesize Au superatoms with exposed surface.

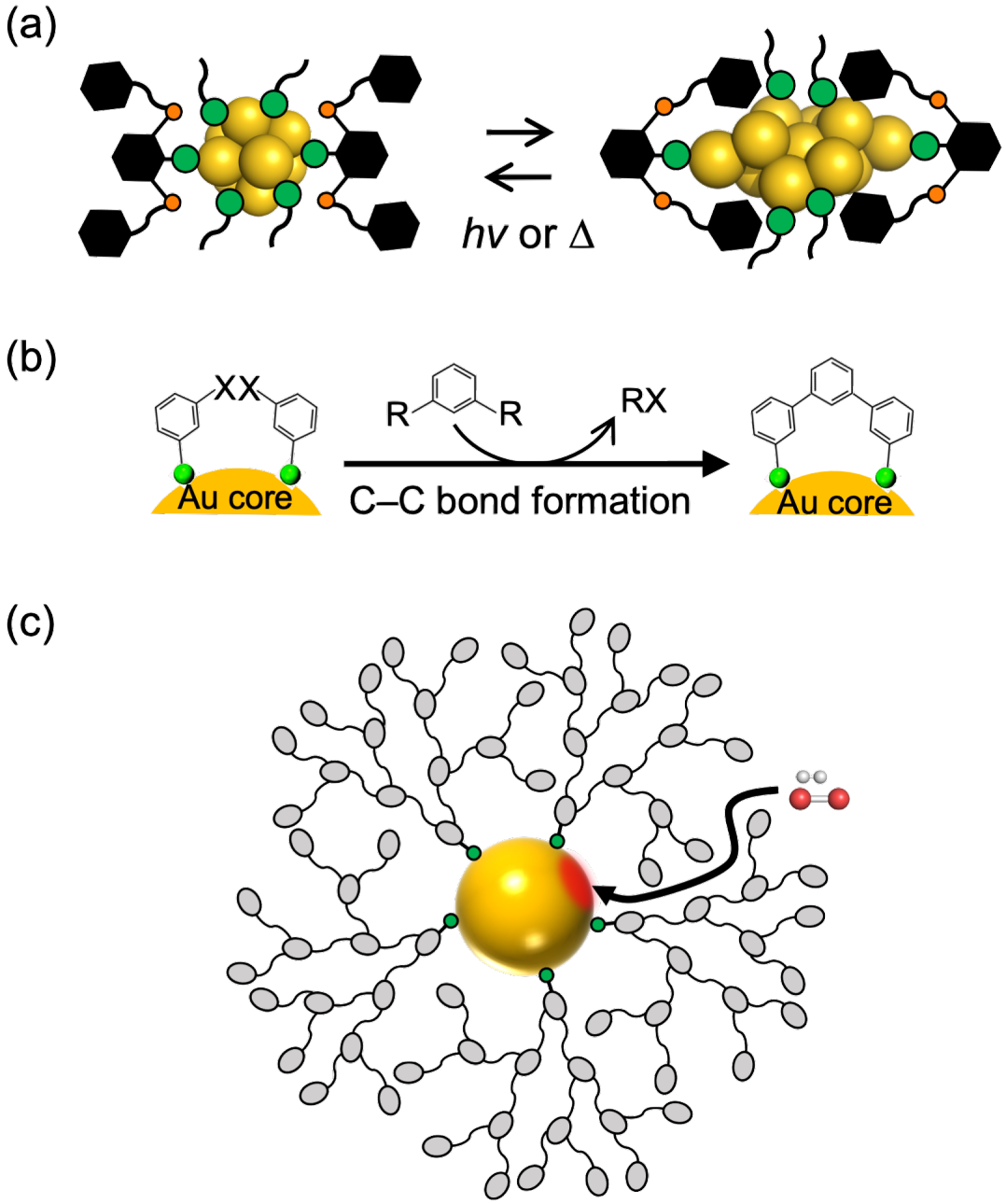

Figure 5.1. Schematic images of (a) reversible structural change of Au superatom, (b) inter-ligand bridging, and (c) bulky ligand-protected Au superatom with exposed uncoordinated sites.

References

1. Higaki, T.; Li, Q.; Zhou, M.; Zhao, S.; Li, Y.; Li, S.; Jin, R. *Acc. Chem. Res.* **2018**, *51*, 2764.
2. Nasaruddin, R. R.; Chen, T.; Yan, N.; Xie, J. *Coord. Chem. Rev.* **2018**, *368*, 60.
3. Kang, X.; Zhu, M. *Chem. Mater.* **2019**, *31*, 9939.
4. Negishi, Y.; Kamimura, U.; Ide, M.; Hirayama, M. *Nanoscale* **2012**, *4*, 4263.
5. Yao, L. Y.; Yam, V. W. *J. Am. Chem. Soc.* **2016**, *138*, 15736.
6. Gunawardene, P. N.; Corrigan, J. F.; Workentin, M. S. *J. Am. Chem. Soc.* **2019**, *141*, 11781.
7. Kang, X.; Ren, M.; Zhu, M.; Zhang, K. *Chem. Mater.* **2020**, *32*, 6736.
8. Nishigaki, J.; Tsunoyama, R.; Tsunoyama, H.; Ichikuni, N.; Yamazoe, S.; Negishi, Y.; Ito, M.; Matsuo, T.; Tamao, K.; Tsukuda, T. *J. Am. Chem. Soc.* **2012**, *134*, 14295.
9. Hasegawa, S.; Tsukuda, T. *Bull. Chem. Soc. Jpn.* **2020**, DOI: 10.1246/bcsj.20200377.

List of Publications and Presentations

Publications related to the thesis

(Chapter 2)

1. "An $Au_{25}(SR)_{18}$ Cluster with a Face-Centered Cubic Core", Tsubasa Omoda, Shinjiro Takano, Seiji Yamazoe, Kiichirou Koyasu, Yuichi Negishi, Tatsuya Tsukuda, *J. Phys. Chem. C* **2018**, *122*, 13199-13204.

(Chapter 3)

2. "Reduction-resistant $[Au_{25}(cyclohexanethiolate)_{18}]^0$ with an Icosahedral Au_{13} Core", Tsubasa Omoda, Shinjiro Takano, Tatsuya Tsukuda, *Chem. Lett.* **2019**, *48*, 885-887.

Publications not related to the thesis

1. “Toward Controlling the Electronic Structures of Chemically Modified Superatoms of Gold and Silver”, Tsubasa Omoda, Shinjiro Takano, Tatsuya Tsukuda, Small *in press*.

Oral presentations

1. “Novel redox and optical properties of thiolate-protected gold superatom $Au_{25}(SR)_{18}$ induced by bulky ligands”, Tsubasa Omoda, Shinjiro Takano, Tatsuya Tsukuda, The 101st CSJ Annual Meeting, Online, March 2021.
2. “チオラート配位子の骨格が誘起する金超原子の特異的構造”, 重田 翼，高野 慎二郎，佃 達哉，第 13 回分子科学討論会，名古屋，2019 年 9 月.
3. “面心立方型の新規チオラート保護金クラスター$Au_{25}(SR)_{18}$ の合成とその起源”, 重田 翼，高野 慎二郎，山添 誠司，小安 喜一郎，根岸 雄一，佃 達哉，第 12 回分子科学討論会，福岡，2018 年 9 月.
4. “面心立方型の $Au_{25}(SR)_{18}$ クラスターの合成と評価”, 重田 翼, 高野 慎二郎，山添 誠司，小安 喜一郎，佃 達哉，ナノ学会第 16 回大会，東京，2018 年 5 月.

Poster presentations

1. “Thiolate (RS)-protected $Au_{25}(SR)_{18}$ clusters with novel structures and redox properties”, Tsubasa Omoda, Shinjiro Takano, Tatsuya Tsukuda, The 76th Fujihara Seminar, International Workshop on Designer Nanocluster Materials -From Gas Phase to Condensed phase-, Tomakomai, Japan, September 2019.
2. “XAFS を用いた面心立方型の新規チオラート保護金クラスター$Au_{25}(SR)_{18}$ の構造評価”, 重田 翼, 高野 慎二郎, 山添 誠司, 小安 喜一郎, 根岸 雄一, 佃 達哉，第 21 回 XAFS 討論会，札幌，2018 年 9 月.
3. “An $Au_{25}(SR)_{18}$ cluster with a face-centered cubic core: synthesis and characterization”, Tsubasa Omoda, Shinjiro Takano, Seiji Yamazoe, Kiichirou Koyasu, Yuichi Negishi, Tatsuya Tsukuda, The 19th International Symposium of Small Particles and Inorganic clusters (ISSPIC19), Hangzhou, China, August 2018.
4. “A novel $Au_{25}(SR)_{18}$ cluster with a face-centered-cubic gold core”, Tsubasa Omoda, Shinjiro Takano, Seiji Yamazoe, Kiichirou Koyasu, Tatsuya Tsukuda, Asian Symposium on Nanoscience and Nanotechnology 2018 (ASNANO2018) "Fundamentals and applications of Nanoclusters and Nanoparticles", Tokyo, Japan, May 2018. **(Best Poster Award)**

Acknowledgements

The present works were conducted at Department of Chemistry, Graduate School of Science, The University of Tokyo, under the supervision of Prof. Tatsuya Tsukuda.

First of all, I would like to express the deepest appreciation to Prof. Tsukuda for his diligent guiding for five years. I learned what is required to be a scientist from him: the elementary knowledge of physical chemistry, the skills for writing and presentations, and how to propose and improve the research topics. Not only the scientific training, but also he kindly gave me an opportunity to interact with domestic and international researchers. Without his patient help, this thesis would not have been possible.

I am deeply grateful to Associate Prof. Kiichirou Koyasu for his instructions in the gas phase experiments and theoretical calculations. He especially taught me the mass spectrometric technique and the theoretical calculation. In addition, his comments from a different perspective helped me to extend an understanding of my research. I would like to express my gratitude to Assistant Prof. Shinjiro Takano for his supports in the liquid phase experiments. He made a great contribution in the measurement and the analysis of single crystal X-ray diffraction. He also spent much time for discussions concerned with the experimental techniques and the research direction. My heartfelt appreciation goes to Prof. Seiji Yamazoe (Tokyo Metropolitan University) who was a former Assistant Prof. of Catalytic Chemistry Laboratory. During his tenure with our group, I got an education about the X-ray absorption spectroscopy and many chances to measure it from him. He continuously supported the analysis and the calculation on it even after the move. I owe my gratitude to Assistant Prof. Shinya Masuda. I received a lot of insights and advices from him during the research.

I would like to appreciate Prof. Yuichi Negishi (Tokyo University of Science) for the collaboration and his valuable comments in the work of Chapter 2. I sincerely thank Dr. Kazuo Kato (Japan Synchrotron Radiation Research Institute, JASRI) for the access of the synchrotron facilities.

I owe my thanks to Ms. Yuka Sakurai for her punctilious support in an office work and the daily life at the laboratory. Besides, my special thanks goes to the current group members: Mr. Sojiro Emori, Mr. Shingo Hasegawa, Ms. Megumi Suyama, Mr. Katsunosuke Nakamura, Mr. Haru Hirai, Mr. Shun Ito, Ms. Koto Hirano, Mr. Taro Shigeta, Mr. Shotaro Matsuda, Mr. Li Xiang, Mr. Wang Lewei, Ms. Emi Ito, Mr. Kensuke Eya, Mr. Toshiki Komagata, Ms. Yuriko Tasaka, Mr. Haruki Fukuda, Mr. Takumi Imagawa, Mr. Masashi Iwamoto, Mr. Naoki Kito, and Mr. Koki Sakamoto. I am also grateful to the former group members: Dr. Hirokazu Kitazawa, Dr. Liang Feng, Dr. Ryo Takahata, Dr.

Chun-Fu Chang, Dr. Satoru Muramatsu, Dr. Ryohei Tomihara, Dr. Shun Hayashi, Dr. Keisuke Hirata, Dr. Kazuyuki Tsuruoka, Mr. Ryo Ishida, Mr. Naoto Sasaki, Mr. Daiki Shuto, Mr. Toshiaki Yanase, Mr. Hiroki Yamada, Mr. Hiroki Yamamoto, Mr. Lim Wei Loon, Mr. Kuenhee Kim, Mr. Ryota Shibuya, Mr. Naoaki Shinjo, Mr. Yuto Nakajima, Mr. Ray Horie, Ms. Atsuko Horinouchi, Mr. Junichi Yamazaki, Mr. Keishiro Yamashita, Mr. Satoshi Osugi, Mr. Takeki Konuma, Mr. Mizuki Shimojima, Mr. Atsushi Matsuo, and Ms. Lin I-Hsuan.

I appreciate the financial supports from Hisao Iwai Memorial Scholarship Foundation, Marubun Research Promotion Foundation, and Japan Society for the Promotion of Science (JSPS) Research Fellowship for Young Scientists. Theoretical calculations in Chapter 2 were partly performed using the Research Center for Computational Science, Okazaki. Synchrotron radiation experiments in Chapter 2 were performed with the approval of JASRI (Proposal Nos. 2016A1436, 2016B0910, 2017A0910, and 2017B0910).

Last but certainly not least, I would like to express my heartfelt thanks to my friends and family for their selfless support at all times.

Tsubasa Omoda